A thesis submitted to the University of Nottingham for the degree of Doctor of Philosophy

School of Physics and Astronomy

Investigating electromagnetic properties of brain tissue using 7 T MRI

Elena Kleban, MSc, BSc

2018

Supervised by Prof. Richard Bowtell and Prof. Penny Gowland

Submitted for examination: November 2018

Viva voce examination: February 2018

Final submission: May 2018

Abstract

Magnetic Resonance Imaging allows electromagnetic properties of the brain to be measured *in vivo*, providing new markers of structure at a microscopic level. Evaluation of the local complex signal evolution observed using a multi-echo gradient-echo (MEGE) sequence can allow the electromagnetic and relaxivity properties of individual tissue compartments to be accessed. The phase evolution carries valuable information about the different compartments, but is dominated by non-local, large-length-scale field variations which present the main challenge in processing complex MEGE data. In this work 2-compartment and 3-pool models are used to describe signal evolution from a mixed tissue and venous compartment and from white matter, respectively. A new method for removing the effects of non-local field variations without corrupting local non-mono-exponential phase evolution is proposed.

The 2-compartment model of venous blood complex signal has been used to access the vascular dependence on orientation and oxygenation levels, and has been validated against existing methods on large distinguishable veins. A phantom consisting of capillary tubes filled with ferritin solution immersed in a water bath has been used to validate the 2-compartment model and the estimated frequency offsets between the ferritin and water compartments at multiple orientations to $\vec{B}_0$ shown to agree with predictions of theory.

White matter in the corpus callosum has been investigated using a saturation-recovery MEGE sequence with variable flip angles with the aim of revealing differences in the T_1-relaxation properties of the myelin, the external and the intra-axonal water compartments. The results show that the relative saturation of the myelin water compartment decreases with increasing flip angle and is consistent with there being a short-T_1 component associated with myelin water. However, the observed signal behaviour shows less contrast than expected based on the findings from the previous studies. This could be related to differences in exchange rates between compartments.

Finally, diffusion-weighted, asymmetric spin-echo imaging was used to simultaneously investigate the diffusivity and electromagnetic properties of the external and intra-axonal compartments of white matter. This approach could provide additional information about white matter microstructure. Asymmetry of the spin echo sequence was achieved by delaying the acquisition by Δt. The preliminary results show an increase in the scaled magnitude with echo delay at a constant b-value in some regions of the corpus callosum. The preliminary results are promising, but further investigation and method development are required.

This thesis has investigated a number of novel methods of studying white matter structure and cerebral microvasculature.

Acknowledgements

I would like to thank my colleagues and friends from SPMIC for making my PhD time of about π years worth remembering. I will never forget the maths/physics chats in the back row of the "Barn" and the coffee breaks/walks in the afternoon. I was incredibly lucky to meet all of you.

Particularly, I would like to thank my supervisors Richard Bowtell and Penny Gowland for patiently guiding me through my studies, for taking any of my naive questions seriously, investing a lot of their time and energy into the projects and proofreading of my thesis chapters, and for being really nice people. I could not have hoped for better supervision, I have learned a lot from you.

I would also like to thank Molly Bright for refreshing my PhD experience by expanding my thesis beyond white matter, MacGyvering through IronPhan and giving me a lot of support on and beyond the project.

My research would be impossible without Andrew Peters – thank you for always finding the time to fix the $7\,\mathrm{T}$ every time I broke it; Lesley Martin – thank you for helping me with handling volunteers' information and other endless questions; and everyone who volunteered to spend some time in the scanner for me – a big thank you!

Finally, I would like to thank my examiners Peter Morris and Martina Callaghan for reading and discussing my thesis, I really enjoyed my viva with you.

Мама, бабушка, братеГ, Berliner Familie und (ex)Heidelberger Freunde, спасибо за ваши терпение и поддержку! Без вас было бы гораздо труднее und das Leben wäre ein bisschen grau. Und natürlich danke Frank, für deine Hilfe mit Mathe und einfach so.

Contents

Introduction **1**

I. Theory 5

1. Background **7**
1.1. Mathematical tools . . . 7
1.2. Gradients . . . 10
1.3. Complex MRI signal . . . 14
1.4. Sequences . . . 16
1.4.1. Multi-echo gradient-echo (MEGE) sequence . . . 16
1.4.2. Diffusion-weighted asymmetric spin echo sequence . . . 20
1.5. Scanning at ultra-high magnetic field strengths: advantages and challenges . . . 26

2. The origin and modelling of local signal **31**
2.1. Local magnetic field perturbation in the presence of a susceptibility distribution . . . 31
2.2. Modelling venous signals . . . 35
2.2.1. Infinite cylinder model . . . 35
2.2.2. Two-compartment model . . . 42
2.2.3. Signal dependency on in-flow . . . 44
2.3. Modelling white matter signals . . . 46
2.3.1. Hollow cylinder model (HCM) . . . 46
2.3.2. Accessing T_1 of the short-T_2^* compartment . . . 50

3. Frequency Difference Mapping **53**
3.1. Introduction . . . 53
3.2. Frequency Difference Mapping (FDM): initial implementation . . . 54
3.3. FDM: application to bipolar MEGE readout . . . 55
3.4. FDM: phantom data . . . 57
3.5. Impact of respiratory motion induced field perturbations on MEGE signal . . . 62
3.6. Conclusion . . . 75

II. Applications 79

4. *In vivo* application of 2-compartment model 81
4.1. Introduction . . . 81
4.2. Materials and Methods . . . 82
4.3. Results . . . 86
4.4. Discussion . . . 88
4.5. Conclusion . . . 90

5. Verification of the 2-compartment model on a phantom 91
5.1. Introduction . . . 91
5.2. Phantom design . . . 92
5.3. Complex signal from the phantom . . . 99
5.3.1. Materials and methods . . . 99
5.3.2. Results . . . 101
5.3.3. Discussion . . . 113
5.4. Conclusion . . . 117

6. Probing the myelin water compartment with a saturation recovery MEGE sequence 119
6.1. Introduction . . . 119
6.2. Materials and methods . . . 120
6.3. Results . . . 131
6.4. Discussion . . . 142
6.5. Conclusion . . . 146

7. Diffusion-Weighted Asymmetric Spin-Echo imaging to probe white matter microstructure 147
7.1. Introduction . . . 147
7.2. Complex signal of DW-ASE . . . 148
7.3. Materials and Methods . . . 153
7.4. Results . . . 156
7.5. Discussion . . . 164
7.6. Conclusion . . . 165

Conclusion 167

List of Acronyms

ASE	asymmetric spin echo
CEST	chemical exchange saturation transfer
DW-ASE	diffusion-weighted, asymmetric spin echo
FDM	Frequency Difference Mapping
FID	free induction decay
FOV	field of view
HCM	hollow cylinder model
ICM	infinite cylinder model
IR	inversion recovery
MEGE	multi-echo gradient-echo
MRI	magnetic resonance imaging
MT	magnetisation transfere
NMR	Nuclear Magnetic Resonance
RF	radiofrequency
ROI	region of interest
SE	spin echo
SNR	signal-to-noise ratio

Introduction

Motivation

Magnetic resonance imaging (MRI) offers a variety of non-invasive techniques to investigate brain microstructure *in vivo*. MR contrast mechanisms based on the electromagnetic properties of brain tissue are particularly exciting, since they might provide a clear marker of tissue composition.

Typically, complex gradient-echo signal is acquired to distinguish between different tissue types, giving rise to techniques such as susceptibility-weighted imaging (Deistung et al. (2008); Haacke et al. (2009)) and quantitative susceptibility mapping Schweser et al. (2011). In recent years there has been a growing interest in the complex multi-echo gradient-echo (MEGE) signal evolution in presence of multiple compartments of myelin water (Wharton and Bowtell (2012); Sati et al. (2013); Lee et al. (2017)). Due to the differences in the transverse relaxation rates and the frequency offsets between the compartments, the evolution of the MEGE signal from white matter tissue is non-mono-exponential. Moreover, the gradient-echo signal is sensitive to the white matter fibre orientation with respect to the magnetic field, $\vec{B}_0$ (Schäfer et al. (2009); Lee et al. (2010); Liu (2010); Wharton and Bowtell (2012)). Wharton and Bowtell (2012) have also shown that the dependence of the complex signal from the brain white matter

on the fibre orientation is not well explained by considering only isotropic component of myelin susceptibility. They have demonstrated that the non-zero frequency offset between the external and intra-axonal compartments can be better explained by there being an additional anisotropic susceptibility component in the myelin-sheath.

Labadie et al. (2014) have investigated bi-exponential longitudinal relaxation in the brain white matter at $7\,\mathrm{T}$, suggesting, there is a component with a short T_1, which has been associated with the myelin water compartment. Oh et al. (2013) and Kim et al. (2015) suggested there is correlation between the short T_1 and the short T_2^* and investigated the MEGE complex signal of the short-T_1-compartment after saturating the long-T_1-compartment at $3\,\mathrm{T}$. Moreover, van Gelderen et al. (2016) explored the effect of magnetisation transfer (MT) on T_1 contrast in white matter using joint analysis of inversion-recovery and MT data at $3\,\mathrm{T}$ and $7\,\mathrm{T}$.

Electromagnetic properties of cerebral venous blood reflect the cerebral blood oxygenation levels, Y_v. The effects on the intra-venous relaxation properties (Lu and Ge (2008); Dagher and Du (2012)) and susceptibility changes (Fan et al. (2014); Driver et al. (2014)) allow quantification of Y_v. However, the application of these techniques is restricted by the vein and voxel sizes. Similar to the effects in the brain white matter, MEGE signal evolution also shows sensitivity to the sub-voxel cerebral venous compartment: Sedlacik et al. (2009) have demonstrated orientation dependence to $\vec{B}_0$ of the MEGE magnitude signal evolution from small sub-voxel cerebral veins and their sensitivity to modulation of Y_v at $1.5\,\mathrm{T}$.

The phase of the complex MR signal carries valuable information on the local tissue composition based on its electromagnetic properties. However, this information is dominated by the effects of the large-length scale field variations and RF-related phase offsets. Therefore, a robust method, which removes the effects from non-local field

perturbation sources without corrupting the local phase evolution, is essential when quantifying the local complex signal evolution. Most of the processing methods are based on subtracting the field perturbations estimated from the linear fitting of the phase evolution, as for example used by Sati et al. (2013). This method may also remove or corrupt the local phase evolution. Wharton and Bowtell (2012) suggested the complex signal processing method called Frequency Difference Mapping (FDM), which relies on the assumption that the large length scale magnetic field perturbations produce a constant rate of phase evolution throughout the MEGE train. Neither of the methods discussed the effect of eddy-current-related field perturbations, which also produce non-linear phase evolution.

Ultra-high magnetic field strengths are beneficial in investigation of electromagnetic properties of tissue because of the higher intrinsic signal-to-noise ratio and the large frequency offsets. The increase of B_0 leads to a decrease of T_2^*, which is especially short ($\leq 10\,\mathrm{ms}$) for myelin water and venous compartments – the main sources of local field perturbations and non-mono-exponential signal decay, and therefore, short echo-times and echo-spacing are essential. In general MEGE acquisitions sample all echoes under read gradients of the same polarity, necessitating the use of opposite polarity "rewind" gradients between echoes. This avoids phase inconsistencies between adjacent echoes at the cost of an increased echo-spacing and therefore reducing the temporal resolution of the sampling of the short-T_2^* signal.

Aim and structure of this work

The main point of this work was to investigate the sources of non-mono-exponential MEGE complex signal evolution in the human brain at $7\,\mathrm{T}$.

The work is separated into two parts. In the first part Chapter 1 covers the mathematical and physical background essential for this work, Chapter 2 provides considerations on local complex signal modelling of the cerebral venous and white matter compartments, Chapter 3 discusses the methods of complex signal processing and phase correction.

The second part of this work demonstrates the phantom and *in vivo* applications of the signal models and processing methods. In Chapter 4 we showed the impact of vein orientation and cerebral blood oxygenation levels on the complex signal evolution *in vivo*. Chapter 5 demonstrates a phantom used to investigate the local complex signal evolution in the presence of two compartments of different, known magnetic properties, in which the smaller compartment had a cylindrical shape. The chapter also details the complex phase processing prior to the quantification. In Chapter 6 we probed a brain white matter *in vivo* with saturation-recovery multi-echo gradient-echo sequence by varying the excitation angle at a fixed repetition time. This allows us to distinguish compartments due to their different relaxivity properties. In Chapter 7 we jointly investigate the diffusivity and relaxivity properties of the white matter with diffusion-weighted, asymmetric spin echo by varying the diffusion weighting at a fixed diffusion time and diffusion-gradient duration and by delaying the acquisition time to add the T_2^*-weighting.

Part I.

Theory

1. Background

1.1. Mathematical tools

This section covers the basic mathematical tools used in this work.

Coordinate systems Depending on the symmetry of the given problem we will use two coordinate systems in this work: the Cartesian coordinate system, identified by a tuple (x, y, z), and the cylindrical coordinate system, identified by the tuple (ρ, φ, z). We will define here basis vectors, gradients and Laplacians as well as simple coordinate transformations, which we will need at a later point.

The basis vectors of the three-dimensional Cartesian coordinate system (x, y, z), with $x, y, z \in (-\infty, \infty)$ are defined as:

$$\vec{e}_x = \begin{pmatrix} 1 \\ 0 \\ 0 \end{pmatrix} , \qquad \vec{e}_y = \begin{pmatrix} 0 \\ 1 \\ 0 \end{pmatrix} , \qquad \vec{e}_z = \begin{pmatrix} 0 \\ 0 \\ 1 \end{pmatrix} . \tag{1.1}$$

The basis vectors of the three-dimensional cylindrical coordinate system (ρ, φ, z), with

$\rho \in [0, \infty)$, $\varphi \in [0, 2\pi]$, and $z \in (-\infty, \infty)$, are defined as:

$$\vec{e}_\rho = \begin{pmatrix} \cos\varphi \\ \sin\varphi \\ 0 \end{pmatrix} , \qquad \vec{e}_\varphi = \begin{pmatrix} -\sin\varphi \\ \cos\varphi \\ 0 \end{pmatrix} , \qquad \vec{e}_z = \begin{pmatrix} 0 \\ 0 \\ 1 \end{pmatrix} . \tag{1.2}$$

It is evident that the z-coordinates are identical for both Cartesian and cylindrical coordinate systems, while the x and y coordinates can be expressed using the coordinates ρ and φ as:

$$x = \rho\cos\varphi , \qquad y = \rho\sin\varphi , \qquad z = z . \tag{1.3}$$

The gradient in cylindrical coordinates can be expressed as:

$$\nabla = \vec{e}_\rho \frac{\partial}{\partial\rho} + \vec{e}_\varphi \frac{1}{\rho}\frac{\partial}{\partial\varphi} + \vec{e}_z \frac{\partial}{\partial z} , \tag{1.4}$$

and the Laplacian is expressed as:

$$\nabla^2 = \frac{1}{\rho}\frac{\partial}{\partial\rho}\left(\rho\frac{\partial}{\partial\rho}\right) + \frac{1}{\rho^2}\frac{\partial^2}{\partial\varphi^2} + \frac{\partial^2}{\partial z^2} . \tag{1.5}$$

Integral transforms and convolution theorem In mathematics a function $F(\alpha)$ related to a function $f(t)$ by an expression of the form

$$F(\alpha) = \int_a^b f(t)K(\alpha, t)\mathrm{d}t \tag{1.6}$$

is called the integral transform of $f(t)$ by the kernel $K(\alpha, t)$. Here we will use two particular integral transforms: the Fourier and Laplace transforms.

The *Laplace transform* $\mathcal{L}$ of a function $f(t)$, for all real numbers $t \geq 0$, is defined by:

$$F(s) = \mathcal{L}\{f(t)\} = \int_0^\infty e^{-st} f(t)\,\mathrm{d}t \ , \tag{1.7}$$

where s is a complex number.

The *Fourier transform* $\mathcal{F}$ of a function $g(x)$, for any real number x, is defined by:

$$F(k) = \mathcal{F}\{f(x)\} = \int_{-\infty}^\infty e^{-2\pi i k x} f(x)\,\mathrm{d}x \ , \tag{1.8}$$

where k is a real number.

The *convolution* $(f * g)(y)$ of two functions $f(x)$ and $g(x)$ is also a form of integral transform and is defined as:

$$(f * g)(x) = \int_{-\infty}^\infty g(y) \cdot f(x - y)\,\mathrm{d}y \ . \tag{1.9}$$

The *convolution theorem* states

$$\mathcal{F}\{f * g\} = \mathcal{F}\{f\} \cdot \mathcal{F}\{g\} \tag{1.10}$$

$$\mathcal{L}\{f * g\} = \mathcal{L}\{f\} \cdot \mathcal{L}\{g\} \ . \tag{1.11}$$

This means, for example, that convolution in the real domain is translated as point-wise multiplication in the Fourier or Laplace domain.

Polynomial A one-dimensional polynomial $P_N(x)$ of degree N can be expressed using summation notation as:

$$P_N(x) = \sum_{n=0}^{N} a_n x^n \ . \tag{1.12}$$

Similarly, a two-dimensional polynomial $P_N(x, y)$ of degree N can be expressed as:

$$P_N(x, y) = \sum_{n=0}^{N} \sum_{k=0}^{n} a_{k,n-k} x^k y^{n-k} \ . \tag{1.13}$$

Complex algebra A complex number $z \in \mathbb{C}$ is an ordered pair of two real numbers (a, b): $z = a + i \cdot b$, where $i = \sqrt{-1}$ is the imaginary unit. This representation is called the *Cartesian representation*. The number a is called the *real* part of the complex number z, and can also be written as $\mathfrak{R}(z) = a$, while b is called the *imaginary* part of z, and is written as $\mathfrak{I}(z) = b$.

A complex number can be expressed in *polar representation* as $z = re^{i\phi}$. The number r is called the modulus or *magnitude* of z, $r = \sqrt{a^2 + b^2}$. The value ϕ is called the argument or *phase* of z, $\phi = \tan^{-1}(b/a)$. In the complex plane, where the real axis is referred to as the x-axis and the imaginary axis is referred to as the y-axis, a complex number can be seen as a vector. Then its absolute value is the length of the vector and its argument is the angle between the vector and the real axis.

1.2. Gradients

In magnetic resonance imaging (MRI) we refer to the *linear magnetic field gradients* in the context of the spatially varying z-component of the magnetic field, i.e. along the main magnetic field $\vec{B}_0$. The variations perpendicular to $\vec{B}_0$ are generally neglected. The formal definition of the gradient vector $\vec{G}$ for the linearly varying z-component of the magnetic field B_z in Cartesian coordinates (x, y, z) is:

$$\vec{G} = \frac{\partial B_z}{\partial x}\vec{e}_x + \frac{\partial B_z}{\partial y}\vec{e}_y + \frac{\partial B_z}{\partial z}\vec{e}_z \equiv G_x\vec{e}_x + G_y\vec{e}_y + G_z\vec{e}_z \ . \tag{1.14}$$

$G_{x,y,z}$ is an orthogonal projection of the vector $\vec{G}$ onto the x, y or z axis which is also called the gradient amplitude along the x, y or z axis. The total z-component of the

magnetic field is thus:

$$B_z = B_0 + G_x x + G_y y + G_z z \ . \tag{1.15}$$

A single gradient pulse shape that starts and ends with zero amplitude is called a gradient lobe. Here we only use gradient lobes of trapezoidal shape. An example of a trapezoidal gradient lobe is shown in Figure 1.1a. When a gradient of trapezoidal shape is applied, the maximum amplitude G_{max} of $G_{x,y,z}$ is not achieved instantly, but linearly increases with time at a finite rate, the so-called gradient slew rate, S_{R}, until the required gradient amplitude is reached. Similarly, when the gradient is switched off the amplitude decreases at a rate S_{R}. The corresponding times are called the *ramp up* and *ramp down* times (which are t_1 and $t_3 - t_2$ in the example in Figure 1.1a).

Eddy currents Following Faraday's law of induction

$$\nabla \times \vec{E} = -\frac{\partial \vec{B}}{\partial t} \ , \tag{1.16}$$

the time-varying magnetic field during the ramp up and ramp down time,$0 < t < t_1$ and $t_2 < t < t_3$, induces electric currents within conductors. These electric currents are known as *eddy currents*. Due to Ampéres's circuital law the eddy currents generate magnetic fields:

$$\nabla \times \vec{H} = \vec{J}_{\mathsf{free}} + \frac{\partial \vec{D}}{\partial t} \ . \tag{1.17}$$

From Lenz's law, these induced fields oppose the field change which induced the eddy currents.

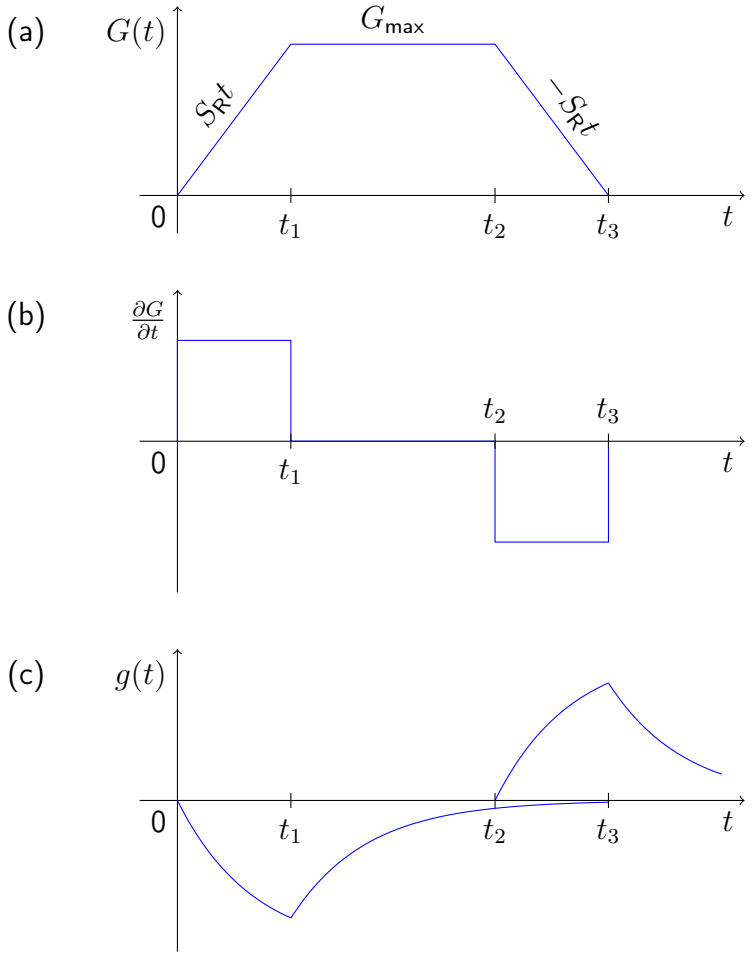


Figure 1.1.: The diagrams show: (a) field gradient variation with time for a trapezoidal gradient lobe shape, (b) the corresponding time-derivative of the field gradient, and (c) the field perturbations induced by eddy currents, which are caused by the time-varying portions of the gradient lobe.

The eddy-current-related phase evolution is described by

$$\phi_{\mathrm{e}}(t) = \gamma \int_0^t B_{\mathrm{e}}(\vec{r}, t')\,\mathrm{d}t' \ , \tag{1.18}$$

where $B_{\mathrm{e}}(\vec{r}, t')$ is the magnetic field due to the eddy currents. The sign of $B_{\mathrm{e}}(\vec{r}, t')$ depends on the direction of the gradient field change and thus of the gradient polarity.

Eddy currents build up during the ramp up and ramp down times and decay during the constant parts of the gradient lobe. In the case of the trapezoidal gradient lobe in Figure 1.1a, eddy currents build up for $t \in [0, t_1] \cup [t_2, t_3]$, i.e. when $\partial_t G \neq 0$, and decay at other times, respectively.

The temporal evolution of the magnetic field $g(t)$ generated by eddy current is given by

$$g(t) = -\frac{\partial G}{\partial t} * e(t) \ , \tag{1.19}$$

as has been shown by van Vaals and Bergman (1990), and Jehenson et al. (1990). The time-dependent function $e(t)$ is the eddy current impulse response which can be modelled as a linear combination of decaying exponentials:

$$e(t) = \begin{cases} \sum_n \alpha_n \cdot e^{-t/\tau_n} & t \geq 0 \\ 0 & t < 0 \end{cases} \ , \tag{1.20}$$

where the constants α_n and τ_n are amplitudes and non-negative time constants. The

time-derivative of the gradient waveform $G(t)$ for a trapezoidal gradient lobe is

$$\frac{\partial G}{\partial t} = \begin{cases} S_{\mathsf{R}} & 0 \leq t \leq t_1 \\ -S_{\mathsf{R}} & t_2 \leq t \leq t_3 \\ 0 & \text{otherwise} \end{cases} . \tag{1.21}$$

Using the convolution theorem and Laplace transformation we get for $g(t)$

$$g(t) = S_{\mathsf{R}} \sum_n \alpha_n \tau_n \sum_{k=0}^{4} \left(1 - e^{-(t-t_k)/\tau_n}\right) \Gamma(t - t_k) \operatorname{sgn}\left(\lim_{t \to t_k^+} \frac{\partial G}{\partial t} - \lim_{t \to t_k^-} \frac{\partial G}{\partial t}\right) , \tag{1.22}$$

which is shown in the example in Figure 1.1c. The spatial dependence of the magnetic fields induced by eddy currents can generally be approximated as low-order polynomials.

1.3. Complex MRI signal

In this short introduction to the complex MRI signal we will describe the characteristics and the origin of the non-local and local sources of variation in the MRI signal. The complex signal evolution, $S_\perp$, induced by the transverse component of magnetisation, Bernstein et al. (2004); Haacke et al. (1999), is defined by:

$$S_\perp(t) \sim \int M_\perp(\vec{r}, t) B_{1,\perp}(\vec{r}) e^{-i\phi(\vec{r},t)} \, \mathrm{d}\vec{r} \, , \tag{1.23}$$

where $M_\perp(\vec{r}, t) = M_\perp(\vec{r}, 0) e^{-t/T_2^*}$ is the absolute value of the transverse component of magnetisation, $B_{1,\perp}(\vec{r})$ is the transverse component of the receiver coil's $\vec{B}_1$ field, $\phi(\vec{r}, t)$ is the angle between the vectors $\vec{M}_\perp(\vec{r}, t)$ and $\vec{B}_{1,\perp}(\vec{r})$. By defining $\phi_M(\vec{r}, t)$ and $\phi_B(\vec{r})$ as the phases of $\vec{M}_\perp(\vec{r}, t)$ and $\vec{B}_{1,\perp}(\vec{r})$, respectively (i.e. the angle between

each of the vectors and the x-axis in the laboratory frame of reference) we can express $\phi(\vec{r},t)$ as shown below:

$$\begin{aligned}\phi(\vec{r},t) &= \phi_M(\vec{r},t) - \phi_B(\vec{r}) \\ &= \phi_M(\vec{r},0) + \Omega(\vec{r})t + \Delta\omega_\chi(\vec{r})t + \Delta\omega_\delta(\vec{r})t' + \gamma\int_0^t \vec{G}(t')\vec{r}\,\mathrm{d}t - \phi_B(\vec{r}) \\ &= \phi_0(\vec{r}) + \Omega(\vec{r})t' + \gamma\int_0^t \vec{G}(t')\vec{r}\,\mathrm{d}t + \Delta\omega_\chi(\vec{r})t + \Delta\omega_\delta(\vec{r})t\ . \end{aligned} \tag{1.24}$$

The phase $\phi_0(\vec{r}) = \phi_M(\vec{r},0) - \phi_B(\vec{r})$ is the angle between $\phi_M(\vec{r},t=0)$ and $\phi_B(\vec{r})$ at $t=0$ and indicates RF-related phase-offsets, $\Omega(\vec{r}) = \gamma\vec{B}_0(\vec{r})$ is the Larmor frequency, whose spatial dependency indicates large-length scale field variations, i.e. magnetic field inhomogeneity. $\Delta\omega_\chi$ and $\Delta\omega_\delta$ are susceptibility χ and chemical shift δ related resonance offsets. The integral term indicates phase offset due to imaging gradients $\vec{G}(t)$. By defining the spatial frequency $\vec{k}(t)$ as

$$\vec{k}(t) = \frac{\gamma}{2\pi}\int_0^t \vec{G}(t')\,\mathrm{d}t'\ , \tag{1.25}$$

we can write the final expression for the complex signal in the Fourier domain as

$$s_\perp(\vec{k},t) \sim \int M_\perp(\vec{r},0)e^{-t/T_2^*(\vec{r})}B_{1,\perp}(\vec{r})e^{-i[\phi_0(\vec{r})+\Omega(\vec{r})t+\Delta\omega_\chi(\vec{r})t+\Delta\omega_\delta(\vec{r})t]}e^{-i2\pi\vec{k}(t)\vec{r}}\,\mathrm{d}\vec{r}\ . \tag{1.26}$$

Since the gyromagnetic ratio γ of a proton is positive, $\gamma = 267.513\cdot 10^6\,{}^{\mathrm{rad}}/_{\mathrm{sT}}$, the vector $\vec{k}(t)$ in (1.25) is parallel to $\vec{G}(t)$ and indicates the direction of the k-space coverage. It is evident from (1.26) that $s_\perp(t)$ is the Fourier transform, which we

defined in (1.8), of the signal $S_\perp(t)$ in the real domain, which can be expressed as:

$$S_\perp(\vec{x},t) \sim M_\perp(\vec{r},0)e^{-t/T_2^*(\vec{r})}B_{1,\perp}(\vec{r})e^{-i[\phi_0(\vec{r})+\Omega(\vec{r})t+\Delta\omega_\chi(\vec{r})t+\Delta\omega_\delta(\vec{r})t]} \ . \tag{1.27}$$

1.4. Sequences

In this section we introduce the two main sequences used in this work: the multi-echo gradient-echo (MEGE) sequence and the diffusion-weighted, asymmetric spin echo (DW-ASE) sequence.

1.4.1. Multi-echo gradient-echo (MEGE) sequence

The MEGE sequence is a MRI sequence, in which multiple gradient echoes are acquired per excitation from a single line of k-space. The position of the acquired line in k-space is determined by the amplitude of the phase-encoding gradient.The gradients along the frequency-encoding axis start with a *prephasing* gradient, which dephases the spin magnetic moments, followed by a *rephasing* readout gradient of the opposite polarity, forming a gradient-echo. The following readout gradients do not require prephasing. The polarity of the frequency-encoding gradient determines the direction in which the line in the k-space is sampled, following the expression in (1.25). Since the MEGE sequence involves a train of fast-switching gradients, the main source of artefacts is the time-varying magnetic fields during the ramp-up and ramp-down periods, which induce eddy currents. These eddy currents produce magnetic fields, which then cause shifts in k-space. This is also evident from Eq. (1.25). The magnetic fields induced by eddy currents oppose the magnetic field change which caused the eddy currents, therefore the k-space shift direction will depend on the polarity of the frequency-encoding gradients. This causes inconsistencies in the field, and therefore the phase,

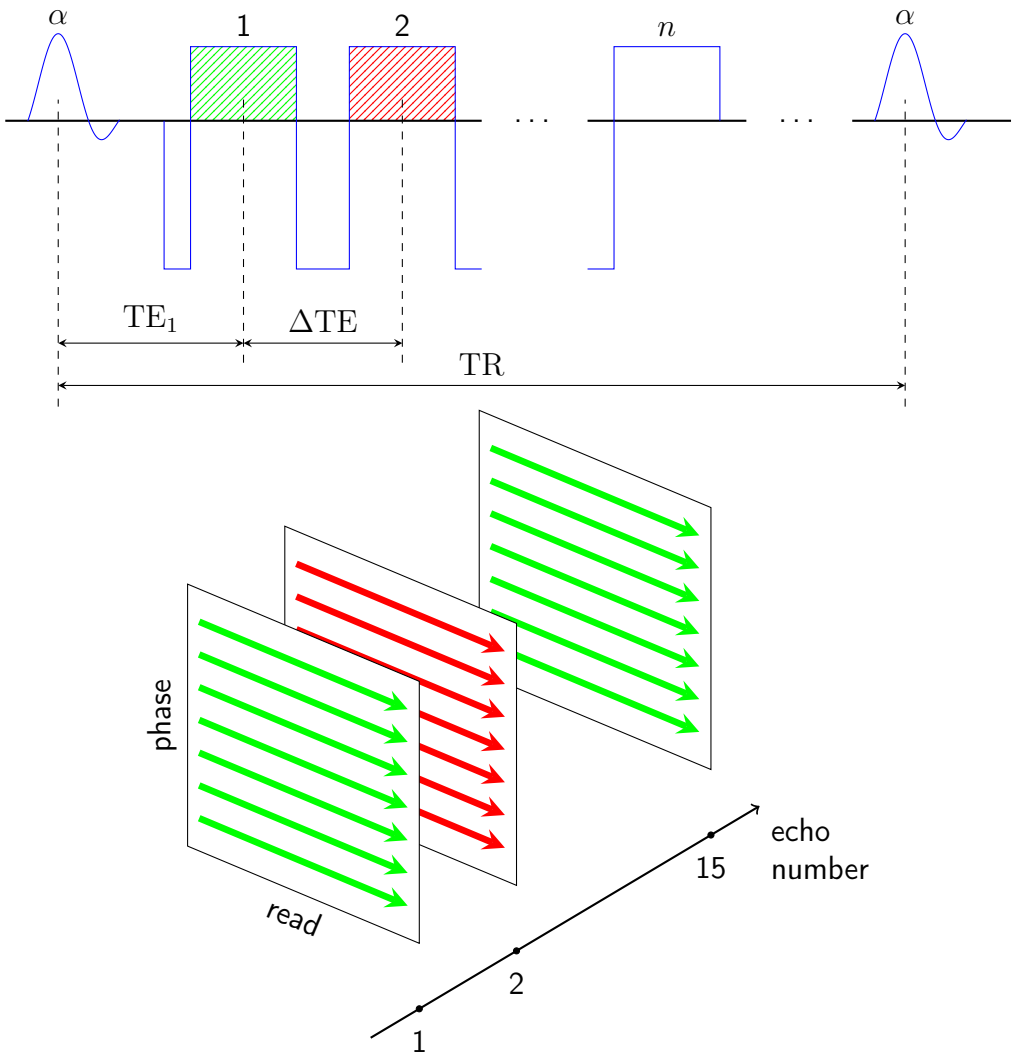


Figure 1.2.: A MEGE sequence with unipolar readout gradients. The k-space is acquired in the same direction for all gradient echoes. The sequence starts with the excitation pulse of angle α followed by a pre-phasing gradient and the train of gradient echoes. The first echo occurs at the echo time TE_1 called the *first echo time*. The time between the adjacent echoes is called *echo-spacing* and is described by the symbol $\Delta\mathrm{TE}$. A single line of k-space is acquired at multiple echo times per excitation and the duration between successive excitations is called the repetition time TR.

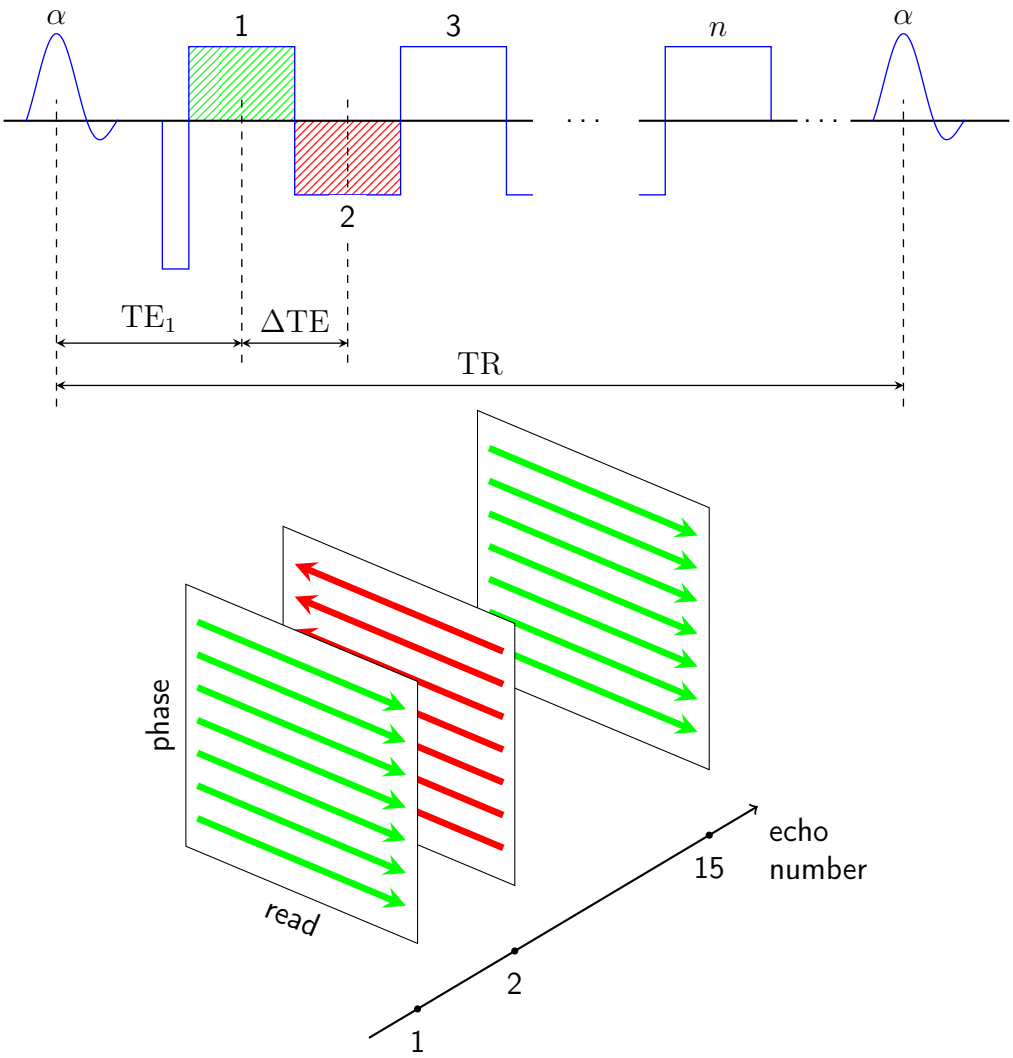


Figure 1.3.: A MEGE sequence with bipolar readout direction. The readout direction in k-space is different for odd and even echoes. The sequence starts with the excitation pulse of angle α followed by a pre-phasing gradient and the train of gradient echoes. The first echo occurs at the echo time TE_1 called the *first echo time*. The time between adjacent echoes is called the *echo-spacing* with the symbol $\Delta\mathrm{TE}$. A single line of k-space is acquired per excitation at multiple echo times and the duration between successive excitations is called repetition time TR.

between adjacent echoes acquired using gradients of opposite polarities. To overcome these inconsistencies two main strategies are used. The first option is to acquire only the signal produced by the gradients of the same polarity. This allows the inconsistency between adjacent echoes to be avoided at a cost of a higher minimum echo spacing. This MEGE acquisition method is called a *unipolar* MEGE readout. The *bipolar* MEGE readout allows signal acquisition for all echoes regardless of the gradient polarity. This reduces the minimum echo spacing but requires some correction for the phase shifts between adjacent echoes. Including these corrections into signal-processing would therefore be the second option. Refer to Figure 1.2 and Figure 1.3, respectively, for schematic representation of MEGE with unipolar and bipolar readout direction as well as the k-space encoding directions.

In the MEGE sequence the magnetisation undergoes the following time evolution after the first excitation

$$M_{\perp}(t) = M_{\perp}(0) \cdot e^{-t/T_2} \cdot e^{-i\Delta\omega_0(\vec{r})t} \ , \tag{1.28}$$

$$M_z(t) = M_z(0) \cdot e^{-t/T_1} + M_0 \cdot (1 - e^{-t/T_1}) \ . \tag{1.29}$$

$M_{\perp} = M_x + iM_y$ describes the transverse magnetisation, M_0 is the equilibrium magnetic moment, $\Delta\omega_0(\vec{r}) = \gamma\Delta B_0(\vec{r})$ represents the local deviation of the magnetic field which leads to a faster signal decay with the effective transverse relaxation time T_2^*, while T_2 and T_1 are tissue characteristic spin-spin and spin-lattice relaxation times. The first exponential in (1.28) arises from the *irreversible* spin-spin relaxation mechanism, the second exponential comes from $\gamma\vec{M} \times \Delta\vec{B}_0$ followed by combining x and y components of the magnetic moment to form the transverse component of magnetisation. $\vec{M}(0)$ is the magnetisation just after the excitation. For an excitation angle α with

the B_1-field applied along the y-axis, $\vec{M}(0)$ would be

$$\vec{M}(0) = M_0 \cdot \begin{pmatrix} \sin\alpha \\ 0 \\ \cos\alpha \end{pmatrix} . \tag{1.30}$$

After a series of excitations a steady-state longitudinal magnetisation, M_E, is achieved (E stands for equilibrium). Its value is smaller than the equilibrium magnetisation, M_0, and depends on the excitation angle α, repetition time TR and the longitudinal relaxation time T_1:

$$M_\mathsf{E} = M_0 \frac{1 - e^{-\mathrm{TR}/T_1}}{1 - \cos\alpha e^{-\mathrm{TR}/T_1}} . \tag{1.31}$$

1.4.2. Diffusion-weighted asymmetric spin echo sequence

To discuss the diffusion-weighted, asymmetric spin echo sequence we first introduce the spin echo (SE) sequence, then derive the asymmetric spin echo (ASE) sequence from it and separately explain the diffusion-weighted spin echo sequence.

Spin echo sequence A spin echo sequence, also called a radiofrequency spin echo sequence, already indicates by its name that the spin echo is formed by using radiofrequency (RF) pulses. In a typical SE sequence a $90°$ RF excitation pulse is followed by a $180°$ refocussing pulse. The delay between both pulses is τ and the echo occurs at the echo time $\mathrm{TE} = 2\tau$.

Following the expressions in (1.28) and (1.30), the transverse component of the magnetic moment evolves after the $90°$ excitation pulse as

$$M_\perp(t < \tau) = M_0 \cdot e^{-t/T_2} \cdot e^{-i\Delta\omega_0(\vec{r})t} . \tag{1.32}$$

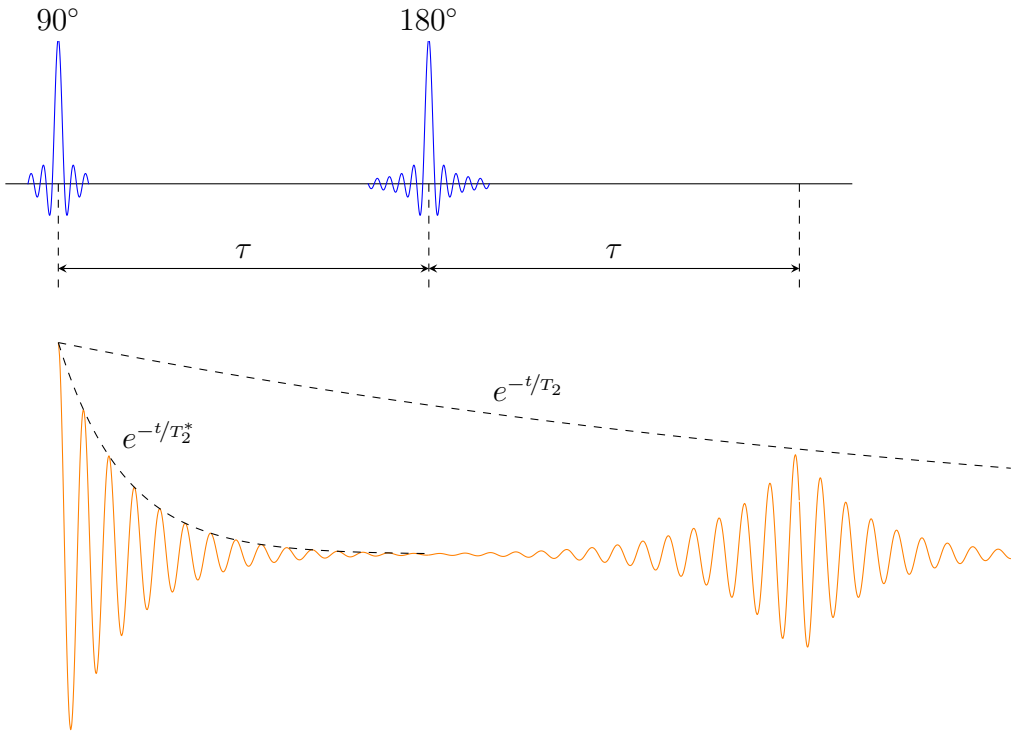


Figure 1.4.: A spin echo sequence consists of a $90°$ excitation pulse and a $180°$ refocussing pulse. There is an additional signal decay due to magnetic field inhomogeneities which is reversed after the refocussing pulse and the RF spin echo builds up.

The effective transverse relaxation time T_2^* combines the effects of *irreversible* spin-spin relaxation described by characteristic relaxation time T_2 and of *reversible* relaxation due to magnetic field inhomogeneities with the characteristic relaxation time $T_2' \sim {}^1/_{\gamma \Delta B_0}$:

$$\frac{1}{T_2^*} = \frac{1}{T_2} + \frac{1}{T_2'} \ . \tag{1.33}$$

Due to magnetic field inhomogeneities within the volume of interest, the magnetic moments precess around the z-axis at frequencies different from the Larmor frequency, γB_0, causing an additional reduction of the net magnetisation with the effective transverse relaxation time defined above. Note, that the proportionality $T_2' \sim {}^1/_{\gamma \Delta B_0}$ is an approximation:

$$\int_\Omega e^{-\Delta\omega_0(\vec{r})t} \mathrm{d}t \approx e^{-t/T_2'}. \tag{1.34}$$

The refocussing 180° pulse along the x-axis will rotate the y and z components of the magnetic moment around the x-axis by 180° leading to the magnetic moment

$$M_\perp(t=\tau) = M_0 \cdot e^{-t/T_2} \cdot e^{i\Delta\omega_0(\vec{r})t} \ . \tag{1.35}$$

just after the pulse. The evolution of the transverse magnetic moment at $t > \tau$ is therefore

$$M_\perp(t>\tau) = M_\perp(\tau) \cdot e^{-(t-\tau)/T_2} \cdot e^{-i\Delta\omega_0(\vec{r})(t-\tau)} \tag{1.36}$$

$$= M_0 \cdot e^{-t/T_2} \cdot e^{-i\Delta\omega_0(\vec{r})(t-2\tau)} \ . \tag{1.37}$$

The final expression indicates that the effects of field inhomogeneities are reversed after the refocussing pulse and and cancel when $t = 2\tau$, i.e. at the spin echo time TE. A schematic diagram of a spin echo sequence is shown in Figure 1.4.

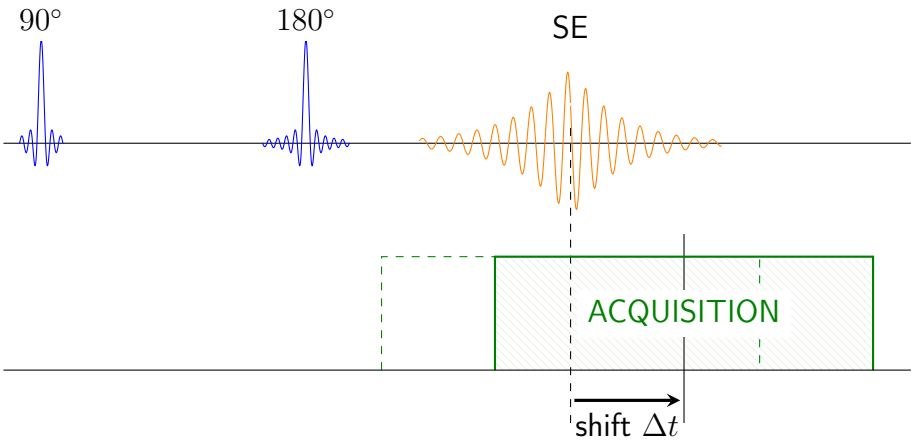


Figure 1.5.: A diagram of the asymmetric spin echo sequence: the centre of k-space is shifted relative to the centre of the RF spin echo by the time Δt.

Asymmetric spin echo If the effective echo time, i.e. the time at which signal at the centre of k-space is acquired, does not match the RF spin echo time, the sequence has an additional T_2^* weighting

$$M_\perp(\mathrm{TE}+\Delta) = M_0 \cdot e^{-\mathrm{TE}+\Delta t/T_2} \cdot e^{-i\Delta\omega_0(\vec{r})\Delta t} \ , \tag{1.38}$$

where Δt is the temporal asymmetry between the RF spin echo and the centre of k-space. A schematic diagram of the asymmetric spin echo sequence is shown in Figure 1.5.

Diffusion weighting The simplest diffusion weighted sequence consists of an excitation pulse applied in conjunction with dephasing and rephasing gradient lobes with equal areas and direction but opposite polarity. The phase accumulated during the dephasing gradient is fully reversed by the rephasing gradient if the spins are stationary. In the presence of Brownian molecular motion, the rephasing is only partial and this leads to signal loss. In the spin echo sequence the dephasing and rephasing gradients are positioned on either side of the refocussing pulse and have the same polarity, since

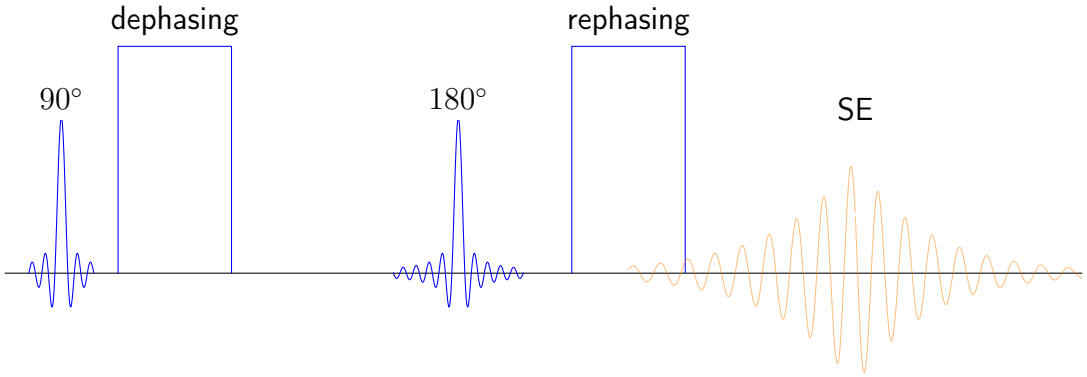


Figure 1.6.: Stejskal-Tanner diffusion weighted spin echo sequence.

the refocussing pulse inverts the phase. This setup was first proposed by Stejskal and Tanner (1965). In general, it is not necessary to have de- and rephasing gradients and the signal loss due to Brownian motion can be observed in spin echo sequences, where the refocussing appears to be partial at long echo times and large diffusion constants. This effect will increase at longer echo times, Hahn (1950); Carr and Purcell (1954). The signal attenuation due to free diffusion in this sequence is exponential

$$\frac{S(b)}{S(0)} = e^{-bD} \ . \tag{1.39}$$

D is the free diffusion coefficient, $S(0)$ and $S(b)$ indicate signals without and with diffusion weighting, respectively. The diffusion weighting factor b is determined by the diffusion gradient form, $\vec{G}(t)$, as it is shown below:

$$b = \gamma^2 \int_0^{\mathrm{TE}} \left[\int_0^t \vec{G}(t') \, \mathrm{d}t' \right] \mathrm{d}t \ . \tag{1.40}$$

When considering the diffusion processes in biological tissues, we no longer speak about *free* diffusion coefficient, but rather of the *apparent* diffusion coefficient, since the molecular motion is additionally confined by the tissue geometry. This means that

diffusion techniques form a very powerful tool for investigating the microstructure of porous media. The signal attenuation with b may also appear to be no longer mono-exponential.

1.5. Scanning at ultra-high magnetic field strengths: advantages and challenges

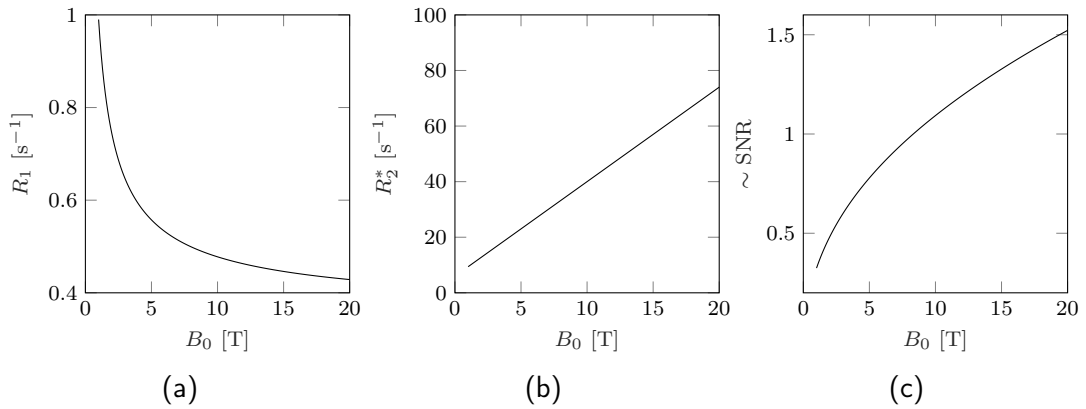
What depends on the magnetic field strength To understand the advantages and challenges of scanning at ultra-high field strengths, we need to consider which imaging values and scanning parameters change with the magnetic field, B_0. We first start with the relaxation rates, since they play an important role for different imaging techniques and also define the scanning parameters. According to Duyn (2012) the dependency of the relaxation rates on the magnetic field can be heuristically approximated by:

$$R_1 = a + b \cdot B_0^c \,, \tag{1.41}$$

$$R_2^* = d + e \cdot B_0 \,. \tag{1.42}$$

The values R_1 and R_2^* stand for longitudinal and effective transverse relaxation rates, respectively, the constants a, b, c, d, and e are tissue type dependent. The approximate values for cortical grey matter are $a = 0.35$, $b = 0.64$, $c = -0.7$, $d = 7$, and $e = 3.5$ (Duyn (2012)). Peters et al. (2007) investigated effective transverse relaxation rates at $1.5\,\mathrm{T}$, $3\,\mathrm{T}$, and $7\,\mathrm{T}$, and estimated $d = 6 \pm 1\,\mathrm{s}^{-1}$ and $e = 3.4 \pm 0.3\,\mathrm{s}^{-1}\mathrm{T}^{-1}$ for cortical grey matter, and $d = 8 \pm 2\,\mathrm{s}^{-1}$ and $e = 4.2 \pm 0.5\,\mathrm{s}^{-1}\mathrm{T}^{-1}$ for cortical white matter. In general the reduction of R_1 (Figure 1.7a) and increase of R_2^* (Figure 1.7b) with increasing magnetic field strength, for the the magnetic field strengths of $1.5\,\mathrm{T}$, $3\,\mathrm{T}$ and $7\,\mathrm{T}$, has been reported by Peters et al. (2007) and Wright et al. (2008).

The susceptibility-related magnetic field perturbation and the secondary magnetic field induced by electron motion depend linearly on the primary magnetic field strength, B_0.



(a) (b) (c)

Figure 1.7.: Dependence of longitudinal (a), and transverse (b) relaxation rates, and SNR (c) in cortical grey matter on magnetic field strength B_0. The curves in (a), (b), and (c) were calculated based on expressions in (1.41), (1.42), and (1.44), respectively, using parameters $a = 0.35$, $b = 0.64$, $c = -0.7$, $d = 7$, and $e = 3.5$.

The precession frequency is also field dependent, $\omega_0 = \gamma B_0$. Therefore the frequency resolution in susceptibility based and chemical shift based scanning is linearly dependent on the magnetic field strength. Similarly the contrast due to the effective transverse relaxation rate R_2^* increases with increasing magnetic field strength.

Since the precession frequency depends on the magnetic field strength, the resonance frequency, $\omega_1 \sim \omega_0$, also called the RF frequency, also increases with the increasing magnetic field strength. The wavelength of the RF field is proportional to its frequency, as follows:

$$\lambda = \frac{2\pi}{\omega_1} c_{\text{medium}} = \frac{2\pi}{\omega_1} \frac{c}{\sqrt{\epsilon_r \mu_r}} \,, \tag{1.43}$$

where c is speed of light in vacuum, ϵ_r is relative permittivity, and μ_r is relative permeability. The latter two values are tissue and frequency dependent. The gyromagnetic ratio of the proton is $\gamma = 2\pi \cdot 42.57747892(29)\,\mathrm{MHzT}^{-1}$. The corresponding Larmor frequency values $\omega_0/2\pi$ for the field strengths of $1.5\,\mathrm{T}$, $3\,\mathrm{T}$, and $7\,\mathrm{T}$ are about

$65\,\mathrm{MHz}$, $130\,\mathrm{MHz}$, and $300\,\mathrm{MHz}$, respectively. The resulting wavelengths in vacuum of the above-mentioned magnetic field strengths are $470\,\mathrm{cm}$, $235\,\mathrm{cm}$, and $100\,\mathrm{cm}$, respectively. The approximate relative permittivity of water and relative permeability of water at room temperature at frequency of $1\,\mathrm{GHz}$ or less are $\epsilon_r = 80$ and $\mu_r = 1$, respectively. Therefore the RF wavelengths in water and water-like medium drops to approximately $50\,\mathrm{cm}$, $25\,\mathrm{cm}$, and $10\,\mathrm{cm}$. This leads to increasing effects of destructive and constructive interference within the imaging volume with the increasing field strength, since the wavelength is similar to the diameter of the object and of the coil size at ultra-high magnetic field strengths.

Advantages One of the most obvious and most interesting advantages of scanning at higher magnetic field strengths for this work is the better frequency and phase contrast in susceptibility contrast measurements, and better R_2^* contrast due to stronger susceptibility based field variations. Scanning techniques using contrast derived from the chemical shift effects, like $^1\mathrm{H}$ spectroscopy, magnetisation transfere (MT), and chemical exchange saturation transfer (CEST), may also benefit from increased magnetic field. Moreover, according to Duyn (2012), the signal-to-noise ratio (SNR) dependancy on magnetic field can be approximated for $\mathrm{TR} \ll T_1$ as

$$\mathrm{SNR} \sim B_0 \sqrt{\frac{R_1}{R_2^*}} \,. \tag{1.44}$$

Therefore scanning at ultra-high magnetic field strengths benefits from higher SNR and therefore allows for better resolution. This, combined with better contrast, makes scanning at $7\,\mathrm{T}$ very attractive for structural and microstructural MRI.

Challenges The magnetic field at the interface between two regions of different susceptibility is distorted. The increase of susceptibility effects with increasing magnetic field strengths results in more severe magnetic field distortions. Also, the artefacts caused by motion-related field variations become more prominent with increasing magnetic field.

As discussed above, the RF required at higher magnetic field strengths has shorter wavelength. For example, the wavelength at $7\,\mathrm{T}$ is comparable with the RF coil and object sizes. As a result, the amplitude of the RF field, B_1, varies across field of view (FOV) leading to variable excitation angle and thus variation in contrast and SNR. It is very important to take these excitation angle variations into account when quantifying T_1 with MEGE.

2. The origin and modelling of local signal

This chapter outlines the physics needed to describe the interaction between material and magnetic fields in Section 2.1. The existing models of venous compartment and white matter are also covered in this chapter in Sections 2.2 and 2.3, respectively.

2.1. Local magnetic field perturbation in the presence of a susceptibility distribution

Isotropic susceptibility Different materials respond differently to an applied magnetic field of strength $\vec{H}$. The strength of the induced magnetic moment $\vec{M}$ is characterised by a dimensionless constant of proportionality χ, called the magnetic susceptibility, so that

$$\vec{M} = \chi \vec{H} \ . \tag{2.1}$$

Thus, a material placed inside a magnetic field can change the local magnetic flux density $\vec{B}$:

$$\vec{B} = \mu_0(\vec{H} + \vec{M}) \ . \tag{2.2}$$

This results in a Larmor frequency shift, which can be measured using a multi-echo gradient-echo sequence.

Depending on the form of the interaction between a material and a magnetic field we can distinguish three main types of material, which are: diamagnetic, paramagnetic and ferromagnetic. Diamagnetic materials are repelled by a magnetic field, i.e. the induced magnetic moment has the opposite sign to the applied magnetic field. Thus the diamagnetic material has negative susceptibility. Unlike diamagnetic materials, paramagnetic and ferromagnetic materials, respectively, are weakly and strongly attracted by the magnetic field, and thus a magnetic moment is induced parallel to the applied magnetic field, and the material consequently has a positive susceptibility. Furthermore ferromagnetic materials can retain magnetisation in the absence of an external magnetic field. In a healthy human brain, areas of high myelination like brain white matter show increased diamagnetism compared to water, whereas venous blood is paramagnetic, since it contains deoxyhemoglobin, which exhibits paramagnetism.

The magnetic field outside a sample of a homogeneous material is perturbed since the magnetic moment induced inside the material (2.1) also generates a magnetic field field outside of the sample. Without loss of generality we can assume that the direction of the applied magnetic field is along the z-axis. Then the magnetic field perturbation along the z-axis $\Delta B_z(\vec{r}_0)$ at a spatial point $\vec{r}_0$ in a domain Ω caused by a susceptibility distribution $\chi(\vec{r})$, for $\chi \ll 1$, can be described as a first-order approximation, by a convolution of the magnetic susceptibility distribution with the z-component of the spatial unit dipole, Jackson (1975); Salomir et al. (2003); Marques and Bowtell (2005);

Jenkinson et al. (2004):

$$\begin{aligned}\frac{\Delta B_z(\vec{r}_0)}{B_0} &= (\chi * d_z)(\vec{r}_0) \\ &= \int_\Omega \chi(\vec{r}) \cdot d_z(\vec{r}_0 - \vec{r})\,\mathrm{d}\vec{r}\,, \end{aligned} \tag{2.3}$$

where the spatial unit dipole field at a location $\vec{r}$ is defined as

$$d_z(\vec{r}) = \frac{3\cos^2\theta - 1}{|\vec{r}|^3}\,, \tag{2.4}$$

with θ being the angle between the spatial vector $\vec{r}$ and the applied magnetic field $\vec{B}_0$ and thus $\cos\theta = {}^{z}/_{|\vec{r}|}$. A 2-dimensional image of the spatial unit dipole field in real space is shown in Figure 2.1a.

The induced magnetic field, the susceptibility distribution and the spatial unit dipole may be represented by 3-dimensional arrays and the convolution in (2.3) will then take the form:

$$\frac{[\Delta B_z]^{i_0,j_0,k_0}}{B_0} = \sum_{i,j,k} \chi_{i,j,k} \cdot [d_z]^{i_0,j_0,k_0}_{i,j,k}\,. \tag{2.5}$$

We can set the size of the array describing the induced magnetic field to $M \times M \times M$ and that describing the susceptibility distribution and the spatial unit dipole to $N \times N \times N$. The coefficients i_0, j_0 and k_0 denote the location where the induced magnetic field needs to be estimated, thus the origin of the spatial unit dipole also matches this location. To make it more computationally applicable we can reshape the susceptibility array into a row vector $\vec{\chi}$ and the spatial unit dipole at the location (i_0, j_0, k_0) into a column vector $[\vec{d_z})]^{i_0,j_0,k_0}$ each containing N^3 elements, then the above expression can be re-written as a matrix product of the row vector $\vec{\chi}$ and a matrix D_z consisting of M^3 column vectors $[\vec{d_z}]^{i_0,j_0,k_0}$. Then the induced magnetic field, now introduced as a

row vector of M^3 elements, can be calculated as follows:

$$\frac{\Delta B_z}{B_0} = \vec{\chi} \cdot D_z \ . \tag{2.6}$$

This expression could be inverted for example if we would want to estimate the susceptibility distribution which produces a given magnetic field. Unfortunately, for $M, N \approx 100$ we would end up with the matrix D_z being $10^6 \times 10^6$ and an average computer cannot handle such large arrays.

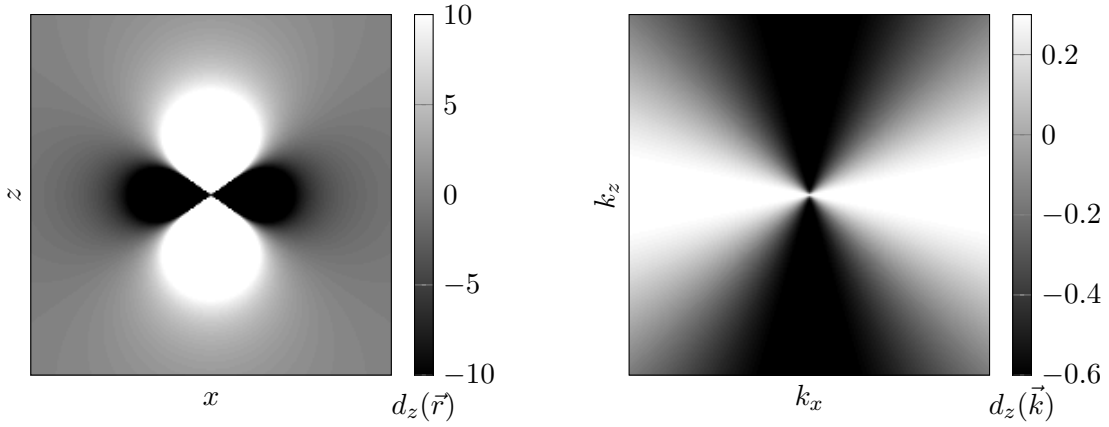
The computational effort can be reduced when (2.3) is transformed into the Fourier domain, since due to the convolution theorem, the convolution in the real domain is a point-wise multiplication in the Fourier domain, Arfken et al. (1999). This approach was used in the NMR context by Deville et al. (1979) for the first time. We refer to the variables in the Fourier domain by placing $\sim$ over the corresponding variable in the real domain. Then the magnetic field $\Delta\tilde{B}_z(\vec{k}_0)$ induced by a susceptibility distribution $\tilde{\chi}(\vec{k})$ is

$$\frac{\Delta\tilde{B}_z(\vec{k}_0)}{B_0} = \tilde{\chi}(\vec{k}_0) \cdot \tilde{d}_z(\vec{k}_0) \ , \tag{2.7}$$

where the spatial unit dipole field, also shown in Figure 2.1b, is

$$\tilde{d}_z(\vec{k}) = \frac{1}{3} - \left[\frac{k_z}{\|\vec{k}\|}\right]^2 \ . \tag{2.8}$$

Anisotropic susceptibility The magnetisation $\vec{M}$ of some materials may depend on the orientation of the sample with respect to the applied magnetic field. In this case the susceptibility χ is no longer described by a scalar value but by a tensor $\underline{\underline{\chi}}$ and



(a) Real domain

(b) Fourier domain

Figure 2.1.: A 2-dimensional illustration of the spatial unit dipole fields in (a) the real domain and (b) the Fourier domain.

the expression in (2.1) is generalised as

$$M^{\mathrm{i}} = \sum_j \chi_{ij} H_j \ . \tag{2.9}$$

2.2. Modelling venous signals

2.2.1. Infinite cylinder model

The infinite cylinder model (ICM) is often used to describe the vascular compartment, Ziener et al. (2005); Sedlacik et al. (2009). It models a vein as an infinite cylinder of radius a with a homogeneous susceptibility that is $\Delta\chi$ higher than the surrounding tissue, and with its axis angled with respect to the static magnetic field $\vec{B}_0$ by θ, see Figure 2.2. The accuracy of the model for representing effects of large veins was validated by Li et al. (2012).

The difference in susceptibility, $\Delta\chi$, between the inside of the cylinder and the sur-

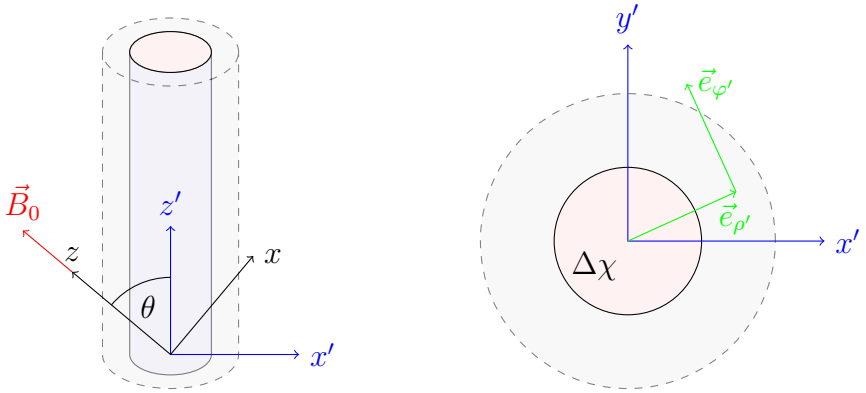


Figure 2.2.: Schematic illustration of the infinite cylinder model: A cylinder of relative susceptibility $\Delta\chi$ is aligned along z', while the static magnetic field $\vec{B}_0$ is aligned along z, the transformation between the reference frames S : (x, y, z) and S' : (x', y', z') is achieved by rotating around the y-axis by an angle θ. The y-axis points away from the viewer.

rounding material produces a relative magnetisation of the cylinder

$$\vec{M} = \Delta\chi\vec{H}_0 = \Delta\chi\vec{B}_0\frac{1}{\mu_0} \ . \tag{2.10}$$

Let S be the frame of reference where the z-axis is aligned with the static magnetic field $\vec{B}_0$ and S' be the frame of reference where the z'-axis is aligned with the axis of the cylinder. For convenience we will use Cartesian, (x, y, z), as well as cylindrical, (ρ, φ, z), coordinates for both frames of reference. The unit vectors are displayed as $\vec{e}_\square$. Both the cylindrical axis and the magnetic field are assumed to lie in the xz-plane and thus the transformation between the two frames of reference is a rotation by an angle θ about the y-axis represented by the rotation matrix $R_y(\theta)$. Thus the static magnetic field $\vec{B}_0$ is represented in each frame of reference as follows:

$$\vec{B}_0(S) = B_0\vec{e}_z \ , \tag{2.11}$$

$$\vec{B}_0(S') = R_y(\theta)\vec{B}_0(S) = B_0(-\sin\theta\vec{e}_{x'} + \cos\theta\vec{e}_{z'}) \ . \tag{2.12}$$

A magnetised cylinder induces internal and external magnetic fields indicated by the superscripts i and e, respectively. Inside the cylinder, the magnetic field strength, the magnetic field flux and the magnetisation are linked together as described in (2.2):

$$\mu_0 \vec{H}^{\mathsf{i}} = \vec{B}^{\mathsf{i}} - \mu_0 \vec{M} \ . \tag{2.13}$$

The internal and external magnetic fields at $\rho' = a$ are linked by the boundary conditions

$$\vec{B}^{\mathsf{i}} \cdot \vec{e}_{\rho'}\Big|_{\rho'=a} = \vec{B}^{\mathsf{e}} \cdot \vec{e}_{\rho'}\Big|_{\rho'=a} \ , \tag{2.14}$$

$$\vec{H}^{\mathsf{i}} \cdot \vec{e}_{\varphi'}\Big|_{\rho'=a} = \vec{H}^{\mathsf{e}} \cdot \vec{e}_{\varphi'}\Big|_{\rho'=a} \ , \tag{2.15}$$

$$\vec{H}^{\mathsf{i}} \cdot \vec{e}_{z'}\Big|_{\rho'=a} = \vec{H}^{\mathsf{e}} \cdot \vec{e}_{z'}\Big|_{\rho'=a} \ . \tag{2.16}$$

The strength of the external field is defined as

$$\vec{H}^{\mathsf{e}} = -\nabla \phi_M \ , \tag{2.17}$$

where ϕ_M is magnetic scalar potential, which satisfies Laplace's equation

$$\nabla^2 \phi_M = 0 \ . \tag{2.18}$$

We can consider a separable solution in cylindrical coordinates for ϕ_M

$$\phi_M(\rho', \varphi', z') = R(\rho') F(\varphi') Z(z') \ . \tag{2.19}$$

The external field strength in cylindrical coordinates in S' is then

$$\begin{aligned} \vec{H}^{\mathsf{e}} &= -\nabla \phi_M \\ &= -\vec{e}_{\rho'} \frac{\partial R}{\partial \rho'} FZ - \vec{e}_{\varphi'} \frac{1}{\rho'} \frac{\partial F}{\partial \varphi'} RZ - \vec{e}_{z'} \frac{\partial Z}{\partial z'} RF \ . \end{aligned} \tag{2.20}$$

Furthermore, we can simplify the problem by solving it separately for the components of the magnetic moment, $\vec{M}$, along and perpendicular to the cylinder axis, i.e. along z' and x', respectively.

The magnetic moment projected onto $\mathbf{x}'$ can be expressed as $\vec{M}_{x'} = M_{x'}\vec{e}_{x'}$, where $M_{x'} = {}^{\Delta\chi}/_{\mu_0 B_0 \sin\theta}$ from Eqs. (2.10) and (2.12). For symmetry reasons the internal induced magnetic field, $\vec{B}^{\mathsf{i}}_{x'}$, is aligned with the magnetic moment, i.e. $\vec{B}^{\mathsf{i}}_{x'} = B^{\mathsf{i}}_{x'}\vec{e}_{x'}$, and thus $\mu_0\vec{H}^{\mathsf{i}}_{x'} = (B^{\mathsf{i}}_{x'} - \mu_0 M_{x'})\vec{e}_{x'}$, also we define $|\vec{H}^{\mathsf{i}}_{x'}| = H^{\mathsf{i}}_{x'}$.

The boundary conditions (2.14)–(2.16) are reduced to

$$\vec{B}^{\mathsf{e}}_{x'} \cdot \vec{e}_{\rho'}\Big|_{\rho'=a} = B^{\mathsf{i}}_{x'} \cos\varphi' \ , \tag{2.21}$$

$$\vec{H}^{\mathsf{e}}_{x'} \cdot \vec{e}_{\varphi'}\Big|_{\rho'=a} = -H^{\mathsf{i}}_{x'} \sin\varphi' \ , \tag{2.22}$$

$$\vec{H}^{\mathsf{e}}_{x'} \cdot \vec{e}_{z'}\Big|_{\rho'=a} = 0 \ . \tag{2.23}$$

The last condition means that the z'-component of $\vec{B}^{\mathsf{e}}_{x'}$ is also zero and thus the value of ϕ_M does not depend on z'. Without loss of generality we can set $Z(z') = 1$. This reduces the magnetic scalar potential in (2.19) to

$$\phi_M = R(\rho')F(\varphi') \ , \tag{2.24}$$

and the external magnetic field strength in (2.20) to

$$\vec{H}^{\mathsf{e}}_{x'} = -\vec{e}_{\rho'}\frac{\partial R}{\partial \rho'}F - \vec{e}_{\varphi'}\frac{1}{\rho'}\frac{\partial F}{\partial \varphi'}R \ . \tag{2.25}$$

The Laplace's equation

$$\frac{1}{\rho'}\frac{\partial}{\partial \rho'}\left(\rho'\frac{\partial R}{\partial \rho'}\right)F + \frac{1}{\rho'^2}\frac{\partial^2 F}{\partial \varphi'^2}R = 0 \tag{2.26}$$

can be rewritten by bringing terms dependent on ρ' to the left-hand-side and those dependent on φ' to the right-hand-side

$$\frac{\rho'}{R}\left(\frac{\partial R}{\partial \rho'}+\rho'\frac{\partial^2 R}{\partial \rho'^2}\right)=-\frac{1}{F}\frac{\partial^2 F}{\partial \varphi'^2}\ . \tag{2.27}$$

Since each side depends only on ρ' and φ', respectively, they both have to be equal a constant, which we set to m^2. From RHS $= m^2$

$$\frac{\partial^2 F(\varphi')}{\partial \varphi'^2}+m^2F(\varphi')=0\ . \tag{2.28}$$

It follows that

$$\boxed{F(\varphi')=k_1\sin m\varphi'+k_2\cos m\varphi'}\ . \tag{2.29}$$

And from the LHS $= m^2$

$$\frac{\partial^2 R(\rho')}{\partial \rho'^2}+\frac{1}{\rho'}\frac{\partial R(\rho')}{\partial \rho'}-\frac{m^2}{\rho'^2}R(\rho')=0\ . \tag{2.30}$$

It follows that

$$\boxed{R(\rho')=c_1{\rho'}^m+c_2{\rho'}^{-m}}\ . \tag{2.31}$$

The coefficients k_1, k_2, c_1 and c_2 are real constants.

From the boundary condition (2.21) it follows that $m=1$ and $k_1=0$ and thus the magnetic scalar potential can be reduced to $\phi_M=(P\rho'+Q{\rho'}^{-1})\cos\varphi'$. Also from (2.21) and (2.22) follows

$$B^{\mathrm{i}}_{x'}=\mu_0(-P+Qa^{-2})\ , \tag{2.32}$$

$$M_{x'}-\frac{B^{\mathrm{i}}_{x'}}{\mu_0}=P+Qa^{-2}\ . \tag{2.33}$$

Additionally, it is also physically reasonable to set $P = 0$ to ensure that the magnetic scalar potential $\phi_M(\rho' \to \infty)$ converges. $B^{\mathsf{i}}_{x'}$ and Q from the above equations can consequently be expressed in terms of B_0

$$Q = \frac{a^2}{2} M_{x'} = \frac{\Delta\chi}{2} \frac{B_0}{\mu_0} \sin\theta a^2 \ , \tag{2.34}$$

$$B^{\mathsf{i}}_{x'} = \frac{\Delta\chi}{2} B_0 \sin\theta \ . \tag{2.35}$$

The external magnetic field flux is then

$$\begin{aligned} \vec{B}^{\mathsf{e}}_{x'} &= \frac{\Delta\chi}{2} B_0 \sin\theta \frac{a^2}{\rho'^2} (\cos\varphi' \vec{e}_{\rho'} + \sin\varphi' \vec{e}_{\varphi'}) \\ &= \frac{\Delta\chi}{2} B_0 \sin\theta \frac{a^2}{\rho'^2} (\cos 2\varphi' \vec{e}_{x'} + \sin 2\varphi' \vec{e}_{y'}) \ , \end{aligned} \tag{2.36}$$

and the internal magnetic field flux is

$$\vec{B}^{\mathsf{i}}_{x'} = \frac{\Delta\chi}{2} B_0 \sin\theta \vec{e}_{x'} \ . \tag{2.37}$$

The magnetic moment projected onto $\mathbf{z'}$ can be expressed as $\vec{M}_{z'} = M_{z'} \vec{e}_{z'}$, where $M_{z'} = {}^{\Delta\chi}/_{\mu_0} B_0 \cos\theta$ from Eqs. (2.10) and (2.12). Similar to the case for projection onto x' we define $\vec{B}^{\mathsf{i}}_{z'} = B^{\mathsf{i}}_{z'} \vec{e}_{z'}$ and thus get $\mu_0 \vec{H}^{\mathsf{i}}_{z'} = (B^{\mathsf{i}}_{z'} - \mu_0 M_{z'}) \vec{e}_{z'}$. From the boundary conditions (2.14)–(2.16) we can conclude that ϕ_M depends only on z' and thus from Laplace's equation $\nabla^2 \phi_M = \frac{\partial^2 Z(z')}{\partial z'^2} = 0$ it follows that

$$\phi_M = Z(z') = a_1 z' + a_2 \ . \tag{2.38}$$

Applying the boundary condition (2.16) we get

$$a_1 = \frac{B^{\mathsf{i}}_{z'}}{\mu_0} - M_{z'} \ . \tag{2.39}$$

It is again physically reasonable to set $a_1 = 0$, thus $B^{\mathsf{i}}_{z'} = \mu_0 M_{z'} = \Delta\chi B_0 \cos\theta$. The external field flux is then

$$\vec{B}^{\mathsf{e}}_{z'} = 0 \ , \tag{2.40}$$

and the internal field flux is

$$\vec{B}^{\mathsf{i}}_{z'} = \Delta\chi B_0 \cos\theta \vec{e}_{z'} \ . \tag{2.41}$$

Total field perturbation in the reference frame of the cylinder S' is the sum of the projections onto x' and z', i.e. the external field flux is

$$\vec{B}^{\mathsf{e}}(S') = \frac{\Delta\chi}{2} B_0 \sin\theta \frac{a^2}{\rho'^2} (\cos 2\varphi' \vec{e}_{x'} + \sin 2\varphi' \vec{e}_{y'}) \ , \tag{2.42}$$

and the internal field flux is

$$\vec{B}^{\mathsf{i}}(S') = \frac{\Delta\chi}{2} B_0 (\sin\theta \vec{e}_{x'} + 2\cos\theta \vec{e}_{z'}) \ . \tag{2.43}$$

The perturbation of the z-component of the magnetic field,$\Delta\vec{B}_z(S)$, can be calculated from $\Delta\vec{B}(S')$ as $\Delta\vec{B}_z(S) = [R_y(-\theta)\Delta\vec{B}(S')]$, where

$$\Delta\vec{B} = \begin{cases} \vec{B}^{\mathsf{i}} & \rho' \leq a \\ \vec{B}^{\mathsf{e}} & \rho' > a \end{cases} \ .$$

Therefore the *macroscopic* field perturbation along z is

$$\Delta\vec{B}_z = \frac{\Delta\chi}{2} B_0 \vec{e}_z \begin{cases} \cos^2\theta + 1 & \rho' \leq a \\ \frac{a^2}{\rho'^2} \sin^2\theta \cos 2\varphi' & \rho' > a \end{cases} \ . \tag{2.44}$$

To find the *microscopic* field perturbation experienced within an infinitesimal region we need to exclude the contribution from the region itself, i.e. by subtracting $^2/_3 \Delta\chi B_0$.

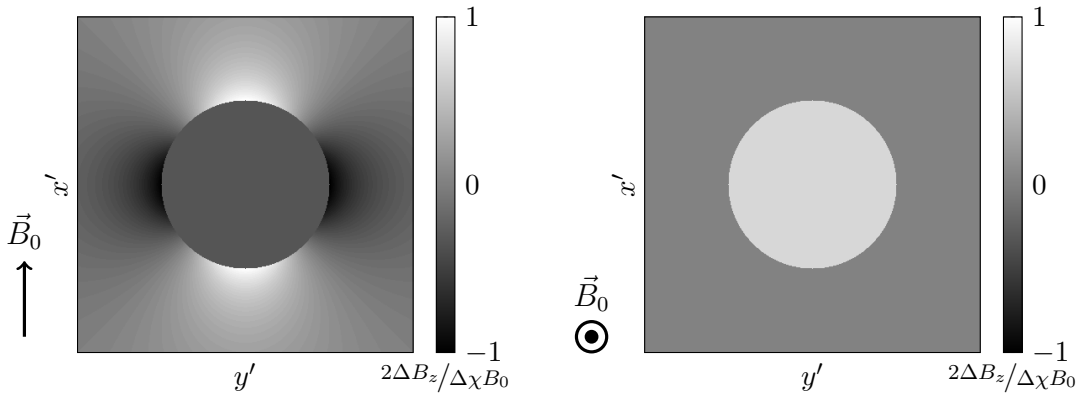


Figure 2.3.: This illustration visualises the field perturbation along $\vec{B}_0$, i.e. along the z-axis from Eq. (2.45) depending on the cylinder orientation using as an example of two extreme orientations: perpendicular to the magnetic field, LHS, and parallel to the magnetic field, RHS.

This concept is known as the sphere of Lorentz and is discussed in detail by Durrant et al. (2003). The microscopic field perturbation along z after applying the sphere of Lorentz correction is therefore

$$\Delta\vec{B}_z = \frac{\Delta\chi}{2} B_0 \vec{e}_z \begin{cases} \cos^2\theta - 1/3 & \rho' \leq a \\ \frac{a^2}{\rho'^2}\sin^2\theta\cos 2\varphi' & \rho' > a \end{cases} . \tag{2.45}$$

Field perturbation in the presence of the cylinder is shown in Figure 2.3 for two extreme orientations, i.e. for $\theta = 0°$ and for $\theta = 90°$.

2.2.2. Two-compartment model

From the field distribution calculated above we can calculate the average frequency offset $\Delta\langle\omega\rangle$ between the venous and the tissue compartments as

$$\Delta\langle\omega\rangle = \gamma B_0 \cdot \frac{\Delta\chi}{2} \cdot \left(\cos^2\theta - \frac{1}{3}\right) . \tag{2.46}$$

The susceptibility difference between the vein and the tissue depends on the susceptibility of fully deoxygenated blood, $\Delta\chi_{\mathsf{do}}$, relative to tissue, the hematocrit, hct, and varies linearly with the blood oxygenation level, Y, as shown in the following relation (Weisskoff and Kiihne (1992)):

$$\Delta\chi = \Delta\chi_{\mathsf{do}} \cdot \mathrm{hct} \cdot (1 - Y) \ . \tag{2.47}$$

Substituting (2.47) into (2.46) we obtain an expression for the frequency offset, which only depends on the blood oxygenation level:

$$\Delta\langle\omega\rangle = \frac{1}{2} \cdot \gamma B_0 \cdot \Delta\chi_{\mathsf{do}} \cdot \mathrm{hct} \cdot (1 - Y) \cdot \left(\cos^2\theta - \frac{1}{3}\right) \ . \tag{2.48}$$

Due to the frequency offset between the tissue, t, and the venous, v, compartments as well as the much faster transverse relaxation rate, R_2^*, of the venous compartment, $R^*_{2,\mathsf{v}} \gg R^*_{2,\mathsf{t}}$, the complex signal evolution from the MEGE sequence from a voxel containing a vein surrounded by tissue is naturally separated into two components.

$$\begin{aligned} S(t) &= S_{\mathsf{venous}}(t) + S_{\mathsf{tissue}}(t) \\ &= M_{\mathsf{v}}(t) \cdot e^{i\phi(t)} + M_{\mathsf{t}}(t) \\ &= \lambda \cdot e^{-R^*_{2,\mathsf{v}}t} \cdot e^{i\Delta\langle\omega\rangle t} + (1 - \lambda) \cdot e^{-R^*_{2,\mathsf{t}}t} \ , \end{aligned} \tag{2.49}$$

where $M(t)$ is a time-dependent complex signal magnitude, $\phi(t)$ is a relative phase evolution, and λ represents the vascular signal fraction.

The two-compartment signal evolution was described by Sedlacik et al. (2009), where they simulated signal magnitude based on the field distribution and fitted it to the acquired magnitude data at $1.5\,\mathrm{T}$.

2.2.3. Signal dependency on in-flow

The vascular signal fraction λ not only depends on the blood volume, but also on spin-lattice relaxation of both compartments and on the velocity of blood flow, especially in the case of single-slice excitation. We consider here the situation as illustrated in Figure 2.4. The z-component of the magnetisation prior to the first excitation is proportional to the slice thickness x

$$M_0 \sim x \ . \tag{2.50}$$

At time $t = 0$, just after the excitation of flip angle α it is reduced by $\cos\alpha$

$$M_z(0) \sim x \cdot \cos\alpha \ . \tag{2.51}$$

With increasing time it evolves towards the equilibrium as

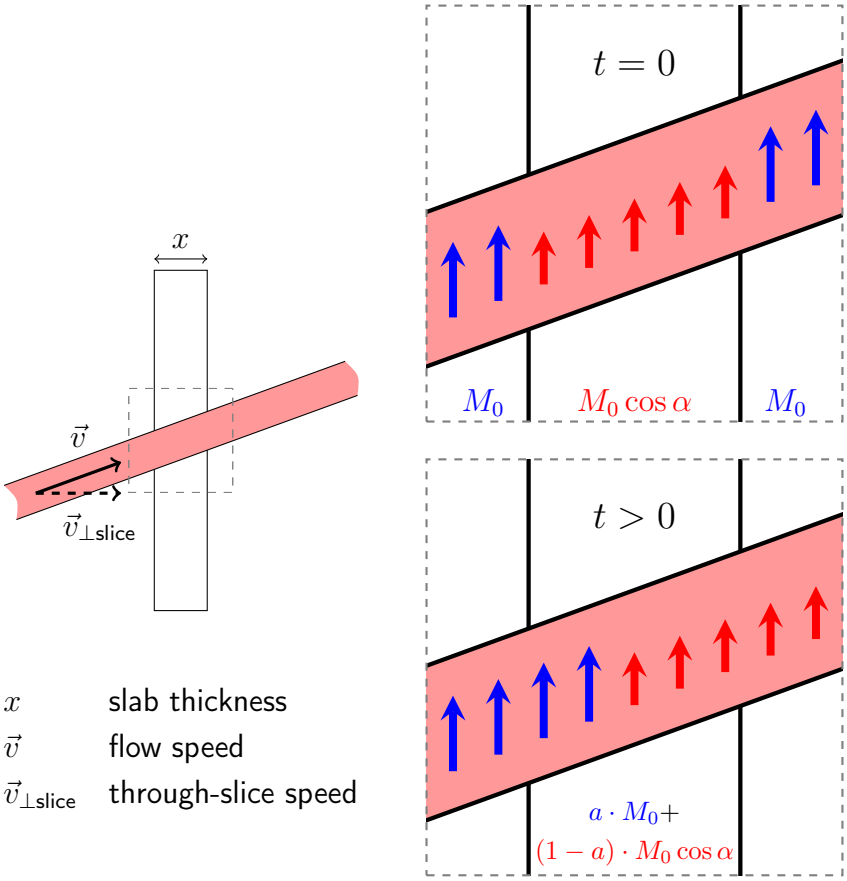
$$M_z(t) \sim M_z(0) \cdot e^{-t/T_1} + M_0 \cdot (1 - e^{-t/T_1}) \ . \tag{2.52}$$

We define a parameter a depending on slab thickness x, through-slice velocity $v_{\perp\text{slice}}$ and the repetition time TR as follows

$$a_t = \begin{cases} {}^{v_{\perp\text{slice}} \cdot t}/_{x} & v_{\perp\text{slice}} \cdot t \leq x \\ 1 & \text{otherwise} \end{cases} \ . \tag{2.53}$$

The additional magnetisation evolution due to flow is

$$M_z^{\text{flow}}(\mathrm{TR}_{n+1}) = a_{\mathrm{TR}} \cdot M_0 + (1 - a_{\mathrm{TR}}) \cdot M_z(\mathrm{TR}_{n+1}) \ , \tag{2.54}$$



x	slab thickness
$\vec{v}$	flow speed
$\vec{v}_{\perp\text{slice}}$	through-slice speed

Figure 2.4.: Schematic illustration of the relation between the flow direction and speed and the slice thickness. Directly after the excitation pulse the equilibrium magnetisation M_0 in the slab is reduced by $\cos\alpha$, where α is the excitation angle. After some time the magnetisation in the slab increases due to inflow effects: $M_z(t > 0) = a \cdot M_0 + (1 - a) \cdot M_0 \cos\alpha$, where a is the factor dependent on the slab thickness x and the through-slice speed of blood flow $\vec{v}_{\perp\text{slice}}$, defined in Eq. (2.53).

where

$$M_z(\mathrm{TR}_{n+1}) = M_z^{\mathsf{flow}}(\mathrm{TR}_n) \cdot \cos\alpha \cdot e^{-t/T_1} + M_0 \cdot (1 - e^{-t/T_1}) \ . \tag{2.55}$$

From the steady-state condition $M_z^{\mathsf{flow}}(\mathrm{TR}_{n+1}) = M_z^{\mathsf{flow}}(\mathrm{TR}_n) \equiv M_z^{\mathsf{E}}$ we can calculate the equilibrium longitudinal magnetisation M_z^{E}

$$M_z^{\mathsf{E}} = M_0 \cdot \frac{1 - (1-a) \cdot e^{-\mathrm{TR}/T_1}}{1 - (1-a) \cdot \cos\alpha \cdot e^{-\mathrm{TR}/T_1}} \ . \tag{2.56}$$

Therefore, the equilibrium transverse magnetisation, and thus also the vascular signal fraction, is T_1-weighted as well as flow-dependent as follows

$$\begin{aligned} M_{xy}^{\mathsf{E}} &= M_z^{\mathsf{E}} \cdot \sin\alpha \\ &= M_0 \cdot \frac{1 - (1-a) \cdot e^{-\mathrm{TR}/T_1}}{1 - (1-a) \cdot \cos\alpha \cdot e^{-\mathrm{TR}/T_1}} \cdot \sin\alpha \ . \end{aligned} \tag{2.57}$$

2.3. Modelling white matter signals

2.3.1. Hollow cylinder model (HCM)

A hollow cylinder model can be used to describe the local field perturbation caused by a myelinated white matter fibre. Liu (2010) and Lee et al. (2010) suggested that the susceptibility of the myelin compartment has an anisotropic component. Wharton and Bowtell (2012) described the magnetic susceptibility of a myelin sheath as a superposition of a hollow cylinder with isotropic magnetic susceptibility χ^{I} and a hollow cylinder with radial anisotropic magnetic susceptibility described by a susceptibility tensor $\underline{\underline{\chi}}$:

$$\chi(\rho) = \begin{cases} \chi^{\mathsf{I}} + \underline{\underline{\chi}} & r < \rho \leq R \\ 0 & \text{otherwise} \end{cases} \ , \tag{2.58}$$

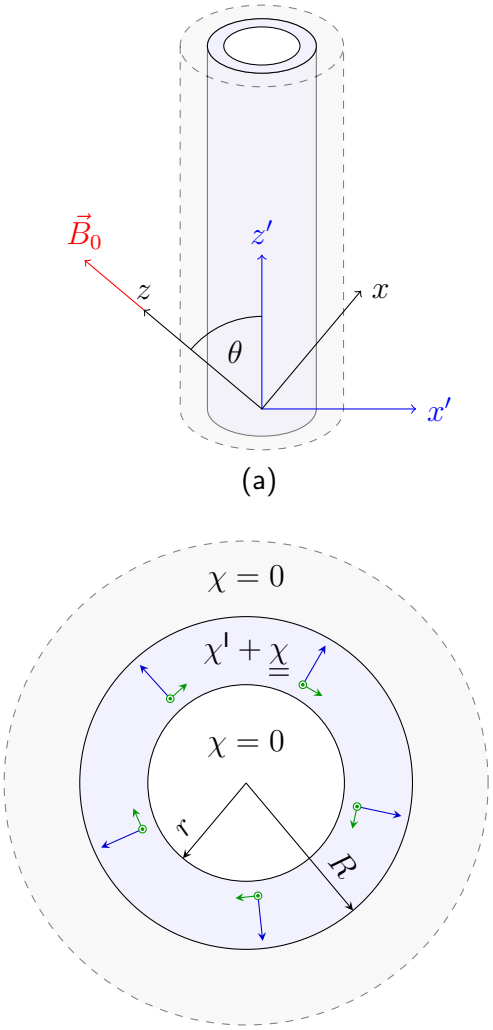


Figure 2.5.: Schematic illustration of the hollow cylinder model: A hollow cylinder of relative susceptibility $\chi^{\mathrm{I}}+\underline{\underline{\chi}}$ is aligned along z', where χ^{I} is the isotropic susceptibility and $\underline{\underline{\chi}}$ is a tensor-representation of the anisotropic susceptibility, static magnetic field $\vec{B}_0$ is aligned along z, the transformation between the reference frames $S : (x, y, z)$ and $S' : (x', y', z')$ is achieved by rotating about the y-axis by an angle θ. The parameters r and R represent the inner and the outer radii of the hollow cylinder. respectively. The blue and the green arrows indicate the radial and the azimuthal components of the anisotropic susceptibility tensor, respectively.

with the susceptibility tensor described in terms of a value χ^{A} which characterises the anisotropic magnetic susceptibility

$$\underline{\underline{\chi}} = \begin{bmatrix} \chi^{\mathsf{A}} & 0 & 0 \\ 0 & -\chi^{\mathsf{A}}/2 & 0 \\ 0 & 0 & -\chi^{\mathsf{A}}/2 \end{bmatrix} , \tag{2.59}$$

where the principal axis of the tensor is radially directed. Wharton and Bowtell (2012) have then derived the field perturbations for this hollow cylinder, the results of which are summarised below. The field perturbation due to a hollow cylinder formed from material with isotropic magnetic susceptibility χ^{i} is:

$$\Delta\vec{B}_z^{\mathsf{I}} = \frac{\chi^{\mathsf{I}}}{2} B_0 \vec{e}_z \begin{cases} \sin^2\theta \cos 2\varphi \frac{R^2 - r^2}{\rho^2} & \rho > R \\ \cos^2\theta - \frac{1}{3} - \sin^2\theta \cos 2\varphi \frac{r^2}{\rho^2} & r < \rho \leq R \\ 0 & \rho \leq r \end{cases} . \tag{2.60}$$

The field perturbation due to a hollow cylinder formed from material with radial anisotropic magnetic susceptibility is:

$$\Delta\vec{B}_z^{\mathsf{A}} = \frac{\chi^{\mathsf{A}}}{2} B_0 \vec{e}_z \begin{cases} \frac{1}{4}\sin^2\theta \cos 2\varphi \frac{R^2 - r^2}{\rho^2} & \rho > R \\ \sin^2\theta \left(-\frac{5}{6} - \frac{1}{4}\cos 2\varphi \left(1 + \frac{r^2}{\rho^2}\right) + \frac{3}{2}\ln\frac{R}{\rho} \right) - \frac{1}{3}\cos^2\theta & r < \rho \leq R \\ \frac{3}{2}\sin^2\theta \ln\frac{R}{r} & \rho \leq r \end{cases} , \tag{2.61}$$

while the average frequency offset resulting from the induced field perturbation by an isotropic hollow cylinder is only non-zero within the material of the hollow cylinder:

$$\Delta\langle\omega^{\mathsf{I}}\rangle = \frac{\chi^{\mathsf{I}}}{2}\gamma B_0 \begin{cases} 0 & \rho > R \\ \cos^2\theta - \frac{1}{3} & r < \rho \leq R \\ 0 & \rho \leq r \end{cases}, \tag{2.62}$$

the average frequency offset contribution from the anisotropic magnetic susceptibility is

$$\Delta\langle\omega^{\mathsf{A}}\rangle = \frac{\chi^{\mathsf{A}}}{2}\gamma B_0 \begin{cases} 0 & \rho > R \\ -\frac{1}{3} + \sin^2\theta\left(\frac{1}{4} - \frac{3}{2}\frac{r^2}{R^2-r^2}\ln\frac{R}{r}\right) & r < \rho \leq R \\ \frac{3}{2}\sin^2\theta\ln\frac{R}{r} & \rho \leq r \end{cases}. \tag{2.63}$$

In this work we are predominantly interested in the case when white matter fibres are oriented perpendicular to the magnetic field, i.e. $\theta \approx 90°$ and thus $\cos^2\theta \to 0$, $\sin^2\theta \to 1$, since it allows us to achieve the maximum contrast between the compartments. The average frequency offsets are then

$$\Delta\langle\omega^{\mathsf{I}}\rangle = -\frac{\chi^{\mathsf{I}}}{6}\gamma B_0 \begin{cases} 1 & r < \rho \leq R \\ 0 & \text{otherwise} \end{cases} \tag{2.64}$$

for the contribution from the an isotropic susceptibility and

$$\Delta\langle\omega^{\mathsf{A}}\rangle = \frac{\chi^{\mathsf{A}}}{2}\gamma B_0 \begin{cases} 0 & \rho > R \\ -\frac{1}{12} - \frac{3}{2}\frac{r^2}{R^2-r^2}\ln\frac{R}{r} & r < \rho \leq R \\ \frac{3}{2}\ln\frac{R}{r} & \rho \leq r \end{cases} \tag{2.65}$$

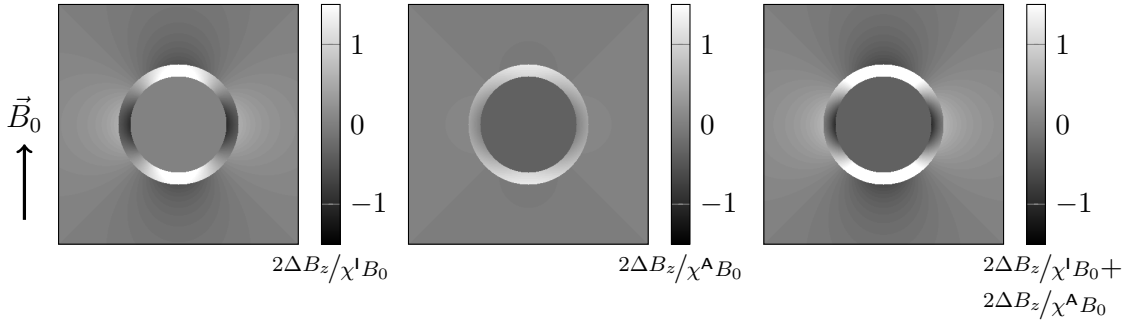


Figure 2.6.: Field perturbation along the z-axis by a hollow cylinder oriented perpendicular to the magnetic field with, from left to right: isotropic susceptibility, anisotropic susceptibility, superposition of isotropic and anisotropic susceptibility. The ratio of χ^{I} and χ^{A} values is about 1.5.

for the contribution from the anisotropic susceptibility.

The field perturbations due to hollow cylinders of isotropic, anisotropic and combined susceptibility, respectively, oriented perpendicular to the magnetic field are shown in Figure 2.6.

2.3.2. Accessing T_1 of the short-T_2^* compartment

The compartments in the hollow cylinder model above can be interpreted as external, $\rho > R$, myelin water, $r < \rho \leq R$, and intra-axonal, $\rho \leq r$, compartments, denoted as e, m and a, respectively. The complex MEGE signal evolution $S(t)$ can be modelled using a complex 3-compartment model (van Gelderen et al. (2012); Nam et al. (2015)) as

$$S(t) = S_{\mathsf{a}}(t) + S_{\mathsf{m}}(t) + S_{\mathsf{e}}(t) \tag{2.66}$$

$$= A_{\mathsf{a}} \cdot e^{-R^*_{2,\mathsf{a}}t} \cdot e^{-i\langle\omega_{\mathsf{a}}\rangle t} + A_{\mathsf{m}} \cdot e^{-R^*_{2,\mathsf{m}}t} \cdot e^{-i\langle\omega_{\mathsf{m}}\rangle t} + A_{\mathsf{e}} \cdot e^{-R^*_{2,\mathsf{e}}t} \ , \tag{2.67}$$

where A, R_2^* and ω characterise the signal amplitude, transverse relaxation rate and frequency offsets relative to the external compartment, respectively. Wharton and

Bowtell (2012), van Gelderen et al. (2012), and Sati et al. (2013) suggested that the myelin water signal decays at a much higher relaxation rate than the external and intra-axonal compartments. Moreover, the signal attenuation of the intra-axonal and external compartments acquired at low TE-values can be assumed similar. Thus here we make the assumption that the transverse relaxation rates are equal for axonal and external water signals, i.e. $R^*_{2,\mathsf{a}} = R^*_{2,\mathsf{e}} \equiv R^*_2$, and rewrite the above expression as

$$S(t) = \left(\frac{A_\mathsf{a}}{A_\mathsf{e}} \cdot e^{-i\langle\omega_\mathsf{a}\rangle t} + \frac{A_\mathsf{m}}{A_\mathsf{e}} \cdot e^{-r^*_{2,\mathsf{m}} t} \cdot e^{-i\langle\omega_\mathsf{m}\rangle t} + 1 \right) \cdot A_\mathsf{e} \cdot e^{-R^*_2 t} \ . \tag{2.68}$$

Here we introduced r^*_2 as the additional relaxation rate of the myelin water signal.
The relative signal fraction of each of the compartments is additionally T_1-weighted. Labadie et al. (2014), and Kim et al. (2015) suggested that the myelin water has a component with much shorter $T_{1,\mathsf{m}}$ than the intra- and extra-axonal compartments. Moreover, van Gelderen et al. (2016) have explored the effect of magnetization transfer on T_1 in white matter. Since the intra- and extra-axonal T_1-values are similar and are much longer than the typical MEGE sequence repetition time TR of $10\,\mathrm{ms}$, we can assume the longitudinal relaxation times of these compartments to be indistinguishable, i.e. $T_{1,\mathsf{a}} = T_{1,\mathsf{e}}$. Thus the relative signal fraction between the myelin and external water compartments, ${}^{A_\mathsf{m}}\!/_{A_\mathsf{e}}$, can be influenced by varying the excitation pulse angle, α:

$$\frac{A_\mathsf{m}}{A_\mathsf{e}}(\alpha) = c \cdot \frac{L_\mathsf{m}}{L_\mathsf{e}}(\alpha) \ , \tag{2.69}$$

where signal attenuation due to spin-lattice relaxation, $L_{\mathsf{e/a/m}}$, of a compartment e/a/m is

$$L_{\mathsf{e/a/m}} = \sin(\alpha) \cdot \frac{1 - e^{-\mathrm{TR}/T_1^{\mathsf{e/a/m}}}}{1 - \cos(\alpha) \cdot e^{-\mathrm{TR}/T_1^{\mathsf{e/a/m}}}} \ . \tag{2.70}$$

3. Frequency Difference Mapping

3.1. Introduction

We have seen in Chapter 1 Section 1.3 in Eq. (1.27) the complex MRI signal carries the local signal information, indicated by local susceptibility- and chemical-shift-related frequency offsets, ω_χ and ω_δ, respectively. Since the water proton signal has much higher SNR than signals from other metabolites containing protons, we can dismiss the influence of chemical shift on local frequency offsets when considering brain image data. We also have seen in Chapter 1 Section 1.3 that the local signal is dominated by frequency offsets due to large length scale field variations, $\Omega(\vec{r})$, and RF related phase offsets, $\phi_0(\vec{r})$. Therefore, our aim is to remove the non-local phase variations without corrupting the local signal evolution.

A method which allows removal of the effects of RF-related phase offsets and large-length scale field variations which was proposed by Wharton and Bowtell (2012), is called Frequency Difference Mapping (FDM) and is described in Section 3.2. In the same section we discuss the restrictions and unresolved challenges of this method, which we then address in Section 3.3 and propose an extension to FDM. We demonstrate both methods on a phantom in Section 3.4 and discuss in detail their differences and challenges. In Section 3.5 we will show the influence of physiological motion on

field variation and address its impact on FDM.

3.2. FDM: initial implementation

Frequency Difference Mapping was proposed for the first time by Tendler and Bowtell (2018) and these authors used this approach to separate the non-local field variation from the local white matter signal. As is evident in the following detailed description of the method, it is essential that the local signal evolution is not mono-exponential. This is the case in myelinated white matter regions, as described in Section 2.3, but following Section 2.2 the sub-voxel vascular compartment also produces a non-mono-exponential signal.

Following Sections 1.3 and 1.4 the complex signal evolution $S_n \equiv S(\mathrm{TE}_n)$ in the real domain from a unipolar multi-echo gradient-echo readout can be expressed as

$$S_n(\vec{r}) = S_0(\vec{r}) \cdot e^{i\Omega(\vec{r})\mathrm{TE}_n} \cdot e^{i\phi_0(\vec{r})} \cdot F_n(\vec{r}) \ , \tag{3.1}$$

where S_0 is the signal amplitude, $F_n \equiv F(\mathrm{TE}_n)$ is the non-mono-exponential local signal from the nth echo modelled as in Eqs. (2.49) or (2.68) for a sub-voxel vascular compartment or white matter, respectively, $\mathrm{TE}_n = \mathrm{TE}_1 + (n-1)\Delta\mathrm{TE}$ is the echo time of the nth echo, with TE_1 being the first echo time and $\Delta\mathrm{TE}$ being the echo spacing. The RF-related phase offsets $\phi_0(\vec{r})$ are removed by division of the signal from the nth echo by the signal from the 1st echo since:

$$S'_n(\vec{r}) \equiv \frac{S_n(\vec{r})}{S_1(\vec{r})} = e^{i\Omega(\vec{r})\cdot[n-1]\cdot\Delta\mathrm{TE}} \cdot \frac{F_n(\vec{r})}{F_1(\vec{r})} \ . \tag{3.2}$$

The non-local, large length scale field perturbations $\Omega(\vec{r})$ are removed in the second step, in which the signal ratio for the nth echo from (3.2) is divided by the $n-1$ power

of the signal ratio for the 2nd echo:

$$\begin{aligned} S''_n &\equiv \frac{S'_n}{[S'_2]^{n-1}} \\ &= \frac{e^{i\Omega(n-1)\Delta\mathrm{TE}}}{\left[e^{i\Omega\Delta\mathrm{TE}}\right]^{n-1}} \cdot \frac{F_n}{F_1} \cdot \left[\frac{F_2}{F_1}\right]^{-(n-1)} \\ &= \frac{F_n \cdot [F_1]^{n-2}}{[F_2]^{n-1}} \ . \end{aligned} \tag{3.3}$$

The phase of the signal ratio in (3.3) strongly depends on the scanning parameters. To diminish this dependency we scale $\arg(S''_n)$ by the echo time and get the final expression for FDM in Hz from the nth echo:

$$\mathrm{FDM}_n = \frac{\arg(S''_n)}{2\pi[n-2]\Delta\mathrm{TE}} \qquad [\mathrm{Hz}]. \tag{3.4}$$

It is very important to keep in mind that the method described here can only be applied directly to the complex data acquired with a unipolar MEGE readout, since the phase information is in this case consistent between the echoes. The biggest disadvantage of the unipolar readout is the additional time it requires for fly-back, Lu et al. (2008). Since the signal from the vascular or myelin water compartment decays very rapidly, it is preferable to have as many echoes as possible before the signal has decayed. In the following section we show, how the inconsistency between the adjacent echoes in a bipolar MEGE readout can be corrected, to enable the calculation of FDM on data collected with a bipolar MEGE readout.

3.3. FDM: application to bipolar MEGE readout

We have mentioned above that the FDM calculation cannot be applied to data acquired with bipolar MEGE readout without pre-processing the data. This is a consequence of the eddy-current-related inconsistency between adjacent echoes acquired under gra-

dients of opposite polarity. This leads to k-space misalignment and therefore phase shifts between the adjacent echoes. The phase correction between the adjacent echoes in bipolar MEGE has been addressed in multiple studies, e.g. in Yu et al. (2010), Hargreaves and Lu (2010), and Peterson and Månsson (2014). The complex MEGE signal acquired without flyback can be expressed as

$$S_n^{\pm}(\vec{r}) = S_0(\vec{r}) \cdot e^{i\Omega(\vec{r})\mathrm{TE}_n} \cdot e^{i\phi_0(\vec{r})} \cdot e^{\pm(-1)^n i\psi_n} \cdot F_n(\vec{r}) \ . \tag{3.5}$$

Consistent with the previous section, F_n is the non-mono-exponential local signal from the nth echo modelled as in Eqs. (2.49) or (2.68) for a sub-voxel vascular compartment or white matter, respectively, and TE_n is the time of the nth gradient-echo. The $\pm$ sign indicates the read gradient polarity of the first gradient echo. The phase ψ_n embodies the effects of time-varying non-local field perturbations which change in sign depending on the gradient polarity, but not in absolute value (e.g. representing effects of eddy-current-related magnetic field perturbations, see Section 1.2).

Multiplication of S_n^+ by S_n^- removes phase shifts between the adjacent echoes, particularly the eddy-current-related phase inconsistency, without corrupting the local signal evolution:

$$S_n^+ \cdot S_n^- = e^{i2\Omega\mathrm{TE}_n} \cdot e^{i2\phi_0} \cdot e^{(-1)^n i\psi_n} \cdot e^{-(-1)^n i\psi_n} \cdot [F_n]^2 \tag{3.6}$$

$$= e^{i2\Omega\mathrm{TE}_n} \cdot e^{i2\phi_0} \cdot [F_n]^2 \ . \tag{3.7}$$

Similar to the method described in Section 3.2 in (3.3) we can calculate $[S^+ \cdot S^-]''$

$$[S_n^+ \cdot S_n^-]'' = \frac{S_n^+ \cdot S_n^- \cdot \left[S_1^+ \cdot S_1^-\right]^{n-2}}{\left[S_2^+ \cdot S_2^-\right]^{n-1}}$$

$$= \left[\frac{F_n \cdot [F_1]^{n-2}}{[F_2]^{n-1}}\right]^2 \ , \tag{3.8}$$

which removes the effects of non-local field perturbations and RF-related phase offsets. The power of 2 in (3.8) of the complex signal ratio is reflected in a factor 2 in its complex argument, i.e.:

$$\arg\left([S_n^+ \cdot S_n^-]''\right) = 2 \cdot \arg\left(\frac{F_n \cdot [F_1]^{n-2}}{[F_2]^{n-1}}\right) \ . \tag{3.9}$$

Therefore when scaling the complex argument in Eq. (3.9) by the echo time, an additional factor of 2 is necessary:

$$\mathrm{FDM}_n = \frac{\arg\left([S_n^+ \cdot S_n^-]''\right)}{4\pi[n-2]\Delta\mathrm{TE}} \ . \tag{3.10}$$

This method can be applied equally well to the MEGE signal from a unipolar readout to remove the eddy current effects induced by the readout gradients. But its major advantage in comparison to the method described in Section 3.2 is that it allows us to apply FDM calculations on MEGE data acquired with bipolar gradient readout and consequently to reduce the echo spacing, $\Delta\mathrm{TE}$, which is essential for the rapidly decaying signals. Since the experiment needs to be repeated with each read gradient polarity, the number of averages can be reduced by factor 2 to achieve the same SNR as for the method described in Section 3.2. The total scan time is therefore maintained.

3.4. FDM: phantom data

Now let us compare the two methods described in Sections 3.2 and 3.3 by applying them to phantom data.

Data acquisition The experimental data to compare the two methods was acquired on the $7\,\mathrm{T}$ scanner from a spherical phantom of $16\,\mathrm{cm}$ diameter, filled with an aqueous copper sulphate solution. We acquired a total of 8 MEGE single slice

Table 3.1.: The list of scanning parameters for the MEGE complex data acquisition from a spherical phantom to compare the data collected from unipolar and bipolar readout gradients.

	α [°]	TR [ms]	TE_1 [ms]	$\Delta\mathrm{TE}$ [ms]	N echoes
unipolar	20	100	1.4	2.2	20
bipolar	20	100	1.4	1.4	30

data sets: 2 different slice orientations, sagittal and coronal; 2 types of read gradient polarity, set by varying the fat-shift direction on the scanner; and 2 different readout types, unipolar and bipolar. The 2D single-slice MEGE magnitude, phase, real and imaginary data were acquired with the following scanning parameters: excitation angle $\alpha = 20°$, FOV of $224 \times 224\,\mathrm{mm}^2$, in-plane voxel size of $1 \times 1\,\mathrm{mm}^2$, slice thickness of $5\,\mathrm{mm}$, 5 dynamic scans, and a repetition time, first echo time, echo spacing and number of echoes of $\mathrm{TR}/\mathrm{TE}_1/\Delta\mathrm{TE}/N = 100/1.4/2.2\,\mathrm{ms}/20$ and $\mathrm{TR}/\mathrm{TE}_1/\Delta\mathrm{TE}/N = 100/1.4/1.4\,\mathrm{ms}/30$ for unipolar and bipolar readout, respectively. A summary of the scanning parameters is listed in Table 3.1.

Complex signal Real and imaginary data from 5 dynamic scans were averaged and combined to form the complex signal: $S = \overline{\Re(S_{\mathsf{dynamic}})} + i \cdot \overline{\Im(S_{\mathsf{dynamic}})}$ for each of the 8 data sets. Example sagittal MEGE phase data, $\arg(S)$, is shown in Figure 3.1, wherein (a) and (b) show the phase from the data acquired with unipolar gradient echo readout, and (c) and (d) show the phase from the data acquired with bipolar gradient echo readout. Phase inconsistency between the adjacent echoes from the bipolar readout is evident. It can be visualised even better by estimating the phase difference between signals acquired with read gradients of opposite polarity, i.e. by calculating $\arg(S^+/S^-)$, where $+$ and $-$ indicate the read gradient's polarity, achieved

by varying the fat-shift direction. Here we selected signals acquired with the fat-shift in the foot and head directions for S^+ and S^-, respectively, when calculating $\arg(S^+/S^-)$. Phase differences between the signals are shown for (a) unipolar and (b) bipolar readout in Figure 3.2 .

FDM calculation The FDM was calculated using Eq. (3.4) for each data set acquired with unipolar MEGE readout. Example data are shown in Figures 3.3a and 3.3b. The FDM of the product of the signals from the data acquired with opposite readout gradient polarities is calculated using Eq. (3.10). The examples for the FDM calculated from the signal products acquired with unipolar and bipolar readouts are shown in Figures 3.3c and 3.3d, respectively. In addition, the frequency profiles through the centre of the FDM images along the z-direction, are plotted as indicated by dashed lines in Figure 3.3, at echo times $\mathrm{TE} = 5.8\,\mathrm{ms}$ and $\mathrm{TE} = 5.6\,\mathrm{ms}$ for unipolar and bipolar readout gradients, respectively, in Figure 3.4.

Inspection of the FDM images shown in Figure 3.3 indicates that the phase wraps present in the raw phase data, Figure 3.1, have been removed. This indicates that some effects of the large length scale phase variations were removed. Also, it is evident, that the inconsistency between the adjacent echoes in the bipolar gradient readout have also been removed and the FDM calculation is possible. In the absence of multiple compartments we expect the FDM to approach a value of zero since the frequency should be constant. However, from Figure 3.3 and Figure 3.4 it is obvious that there is some residual spatial field variation predominantly of linear character in the z-direction producing up to $15\,\mathrm{Hz}$ of frequency variation across the phantom. This is not surprising, since the method described in Section 3.2 only removes phase variations that are linear in time, and the method described in Section 3.3 although additionally

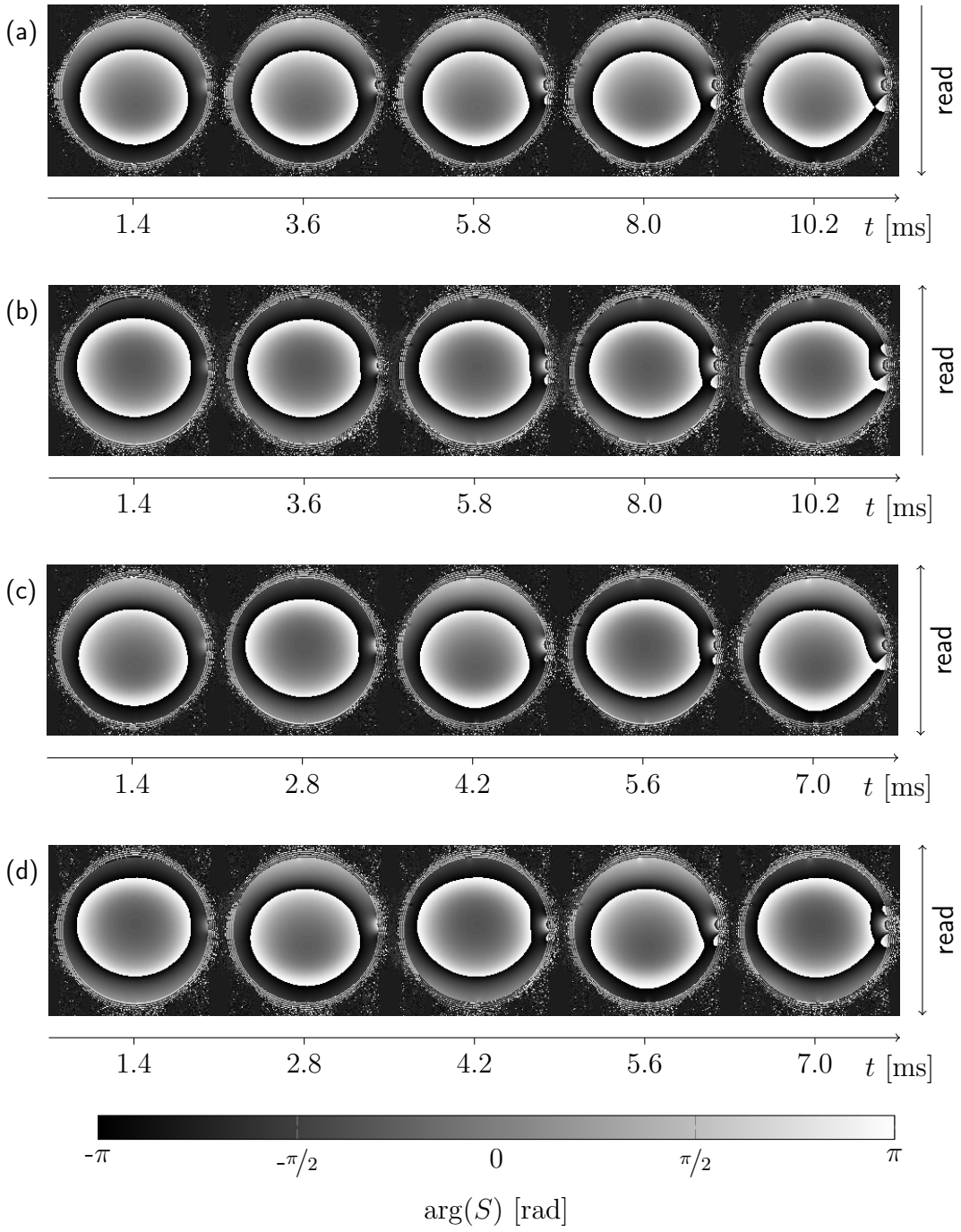


Figure 3.1.: An example for the single sagittal slice MEGE phase data from the first five echoes: (a) MEGE unipolar readout and fat-shift in the foot direction; (b) MEGE unipolar readout and fat-shift in the head direction; (c) MEGE bipolar readout and with fat-shift in the foot direction; (d) MEGE bipolar readout and with fat-shift in the head direction. The inconsistency in phase between the adjacent echoes in the data without flyback is evident from the images shown in (c) and (d).

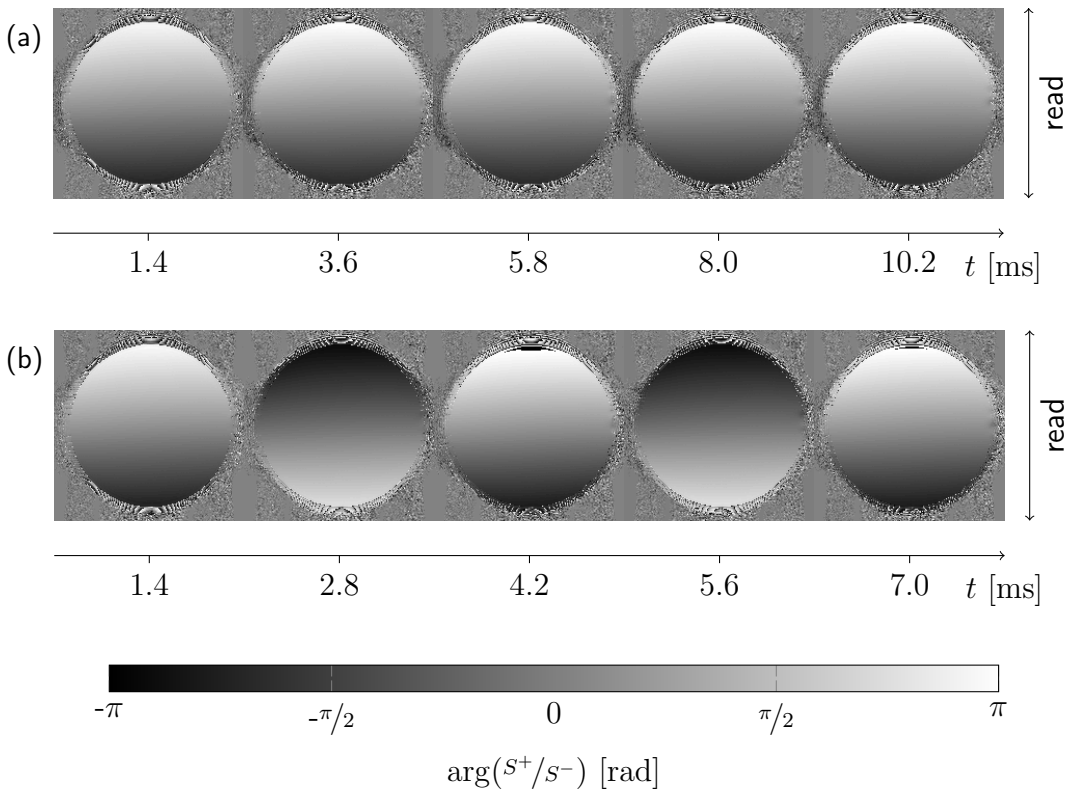


Figure 3.2.: The argument of the complex ratio of signals acquired with the two different read gradient polarities, $\arg(S^+/S^-)$, shows the inconsistency between the adjacent echoes when signal is acquired using bipolar (b) MEGE readout in contrast to the signal acquired using unipolar (a) MEGE readout. It is obvious, that the calculation of FDM from signal acquired using bipolar MEGE readout would be problematic without prior correction of this inconsistency.

removing the temporally non-linear effects arising from the readout gradients, does not remove the field variations from other eddy current sources, e.g. from the slice selective gradients. Therefore, additional field correction or more advanced pulse programming, e.g. by also inverting all the gradients along the slice direction, is necessary.

Additional eddy current correction The spatial character of eddy current field variations can be approximated as a low-order polynomial, as discussed in Section 1.2. The FDM were corrected for eddy current related field variation using 2-dimensional polynomials (1.13) of degrees $N = 1$, $N = 2$ and $N = 3$. The corrected FDM data for $N = 1$, $N = 2$ and $N = 3$ are compared in Figure 3.5 at two different echo times. The images show that the major field perturbations are spatially linear, but inclusion of higher degree polynomials allow further improvement: the improvement between $N = 1$ and $N = 2$ degree polynomial corrections is evident from the histograms shown in Figure 3.5. This figure also shows that further increase of polynomial degree gives only minor improvement. Since eddy-current-related field perturbations are hardware-related and therefore can be assumed not to vary between the scans, the polynomial fit from the phantom data can be applied to the in vivo data, providing us an unbiased field correction.

3.5. Impact of respiratory motion induced field perturbations on MEGE signal

Field perturbations due to respiratory motion Chest expansion in respiration causes periodically varying magnetic field perturbations which are especially significant at ultra-high magnetic field strengths, see van de Moortele et al. (2002), van Gelderen et al. (2007), and Vannesjo et al. (2015). During a single-slice, MEGE scan with

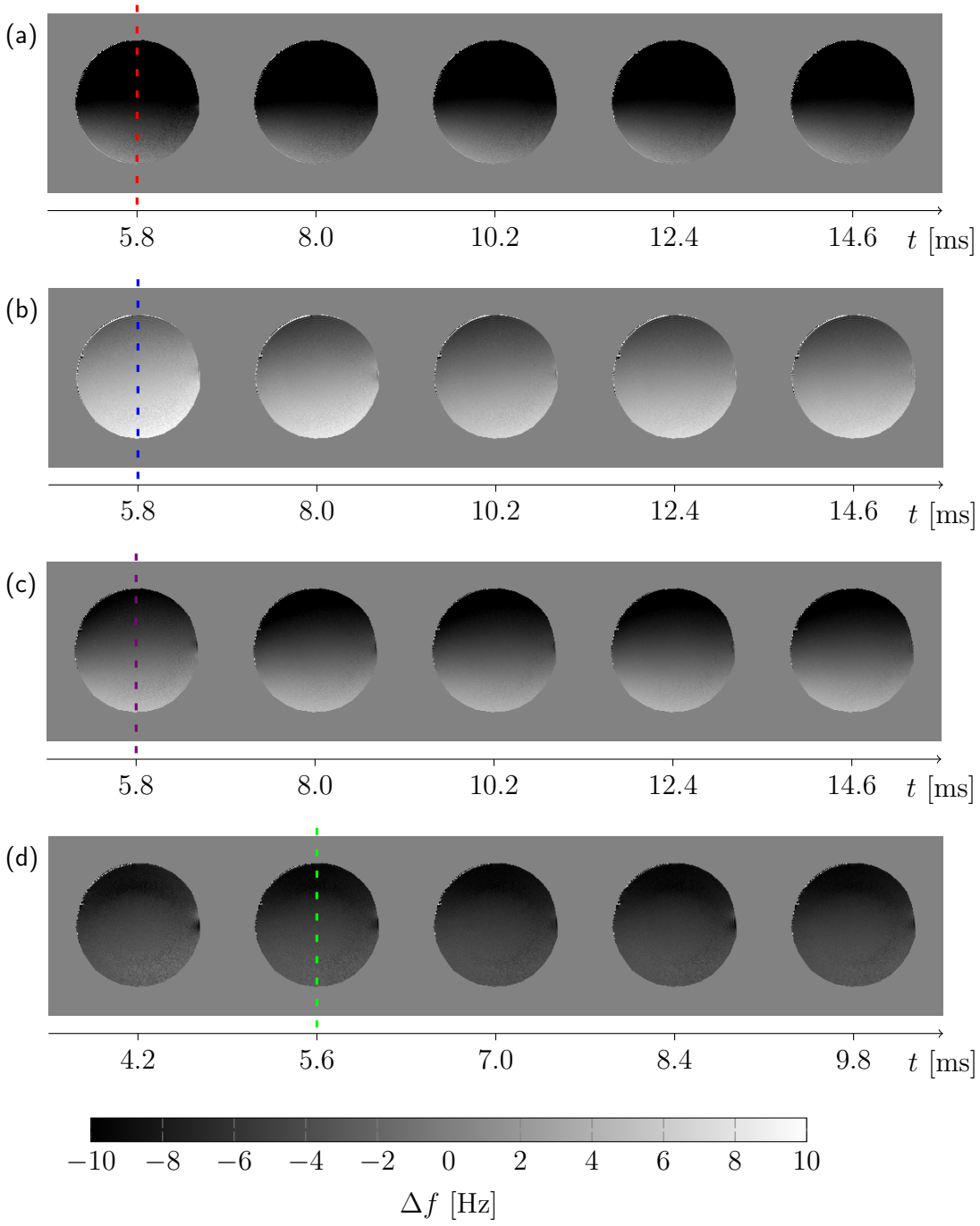


Figure 3.3.: FDM calculated using Eq. (3.4): images in (a) and (b), and Eq. (3.10): images in (c) and (d). The signals for (a) and (b) were acquired using unipolar readout with fat-shift in the foot and head direction, respectively, and in (c) the product of these signals is used. The FDM in (d) were calculated from the product of signals acquired using bipolar readouts of opposite polarity. The dashed lines in each group of images indicate the positions and echo times chosen for plotting the frequency profiles shown in Figure 3.4, the colours are correlated between both figures.

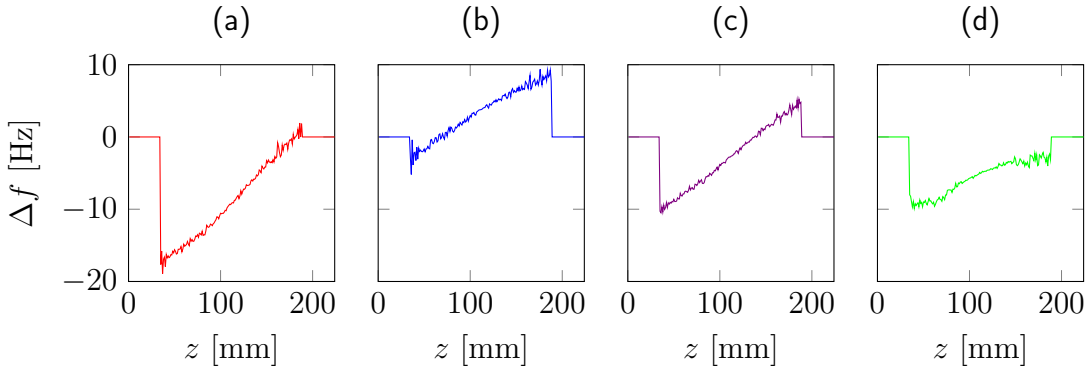


Figure 3.4.: Frequency profiles from the FDM images indicated in Figure 3.3.

total scan duration of about 20-25 s an average subject inhales and exhales about 4 or 5 times. The FDM calculation cannot correct for these field changes, therefore it is important to understand the limitations arising from this physiological motion. We have therefore measured the influence of respiratory motion on the magnetic field variation in the brain at 7 T by acquiring complex EPI images of a single mid-sagittal slice in the brain, resolution $2 \times 2 \times 2\,\mathrm{mm}^3$, every 100 ms at an echo time of 25 ms, from a healthy volunteer. We assumed, that the hardware-related field perturbations remained constant throughout the scan, and the phase changes in each acquisition relative to the first acquisition are purely of physiological character or related to subject movements. To visualise the spatial field variation we calculated maps of frequency changes relative to the first acquisition:

$$\Delta f(t) = \arg\left[\frac{S_m}{S_0}\right] \frac{1}{2\pi \mathrm{TE}} \,, \tag{3.11}$$

where S_0 is the signal from the first acquisition, S_m is the signal from the acquisitions at time $t = \mathrm{TR}_m$, and TE is the echo time. An example of the field variation, measured during a single respiratory cycle is shown in Figure 3.6.

The subject was asked to do the following tasks during three separate scans: (i) to

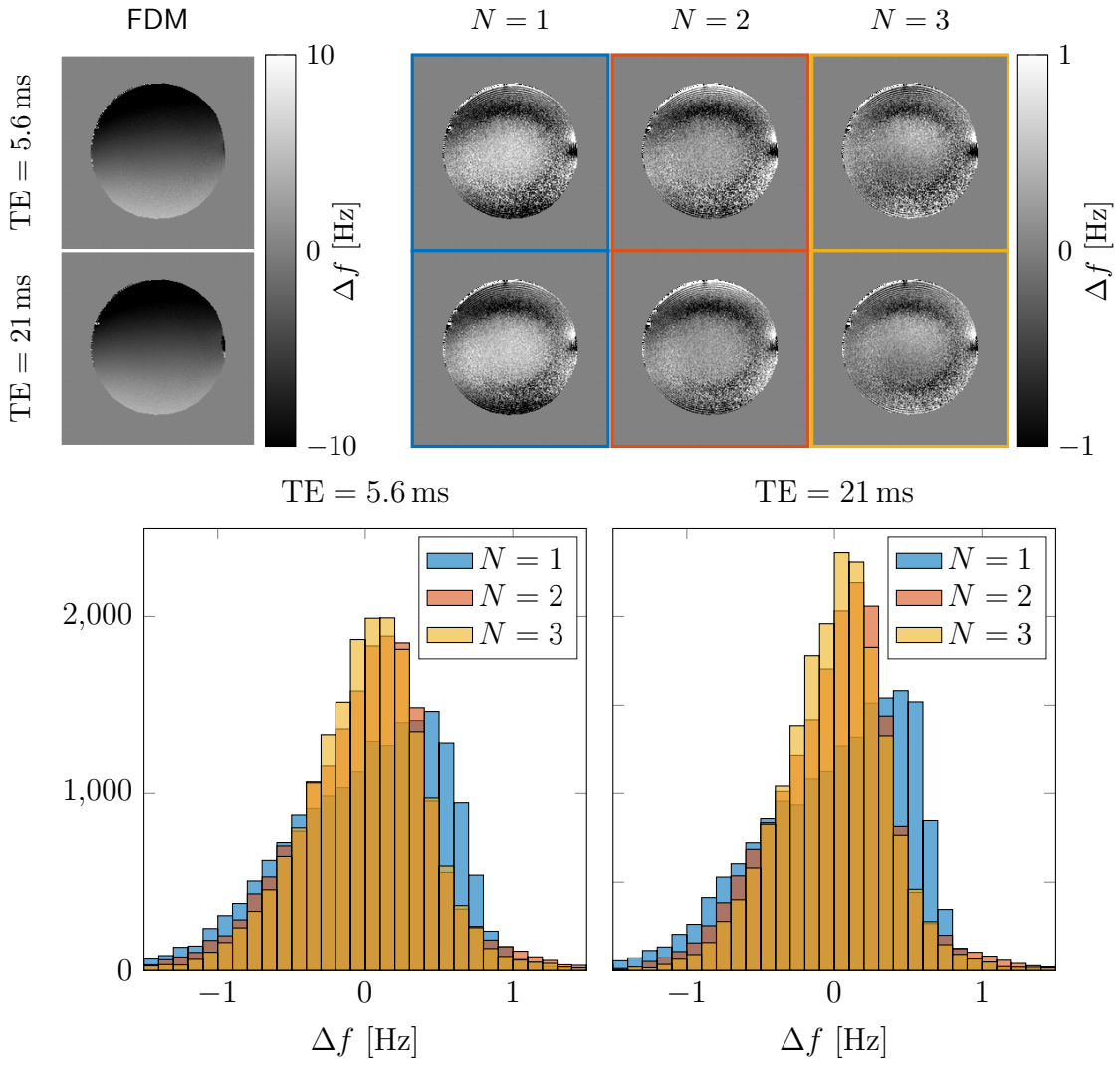


Figure 3.5.: FDM data from complex signals acquired using bipolar MEGE readout before and after spatial polynomial fit correction is shown at two different echo times $\mathrm{TE} = 5.6\,\mathrm{ms}$ and $\mathrm{TE} = 21\,\mathrm{ms}$, displayed in the images shown in the top and bottom rows, respectively. The histograms show the frequency distribution across the phantom at echo times $\mathrm{TE} = 5.6\,\mathrm{ms}$ (left) and $\mathrm{TE} = 21\,\mathrm{ms}$ (right), to indicate the difference between the corrections for polynomials of different degrees $N = 1$, $N = 2$, $N = 3$.

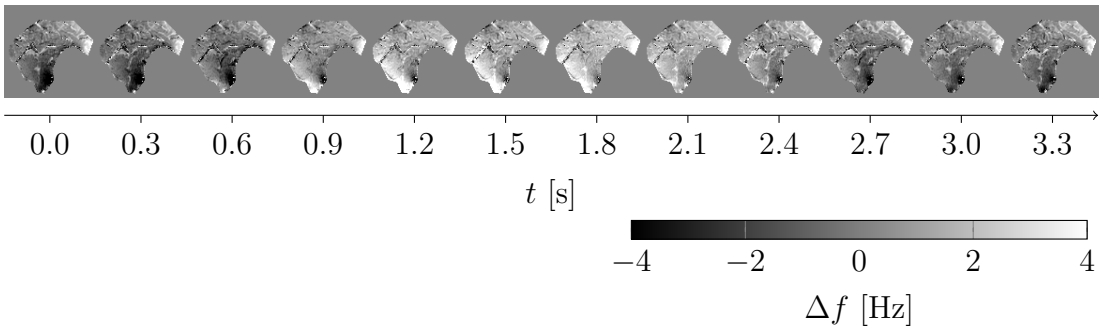


Figure 3.6.: Field perturbations during a single respiratory cycle.

breath deeply for 2 minutes, (ii) to breath normally for 2 minutes, and (iii) to hold their breath for 20 seconds. For each task the frequency change relative to the first scan was averaged within three different ROIs positioned in: the whole corpus callosum (cc), the splenium of the corpus callosum and the genu of the corpus callosum, and then plotted against time. The plots are shown in Figure 3.7. Figure 3.8 shows the frequency variation measured during normal breathing and during breathhold plotted over the duration of the breathhold as well as their Fourier transformations to make clear what the frequencies of the fluctuations are. It is evident from Figure 3.7 that the frequency variation is periodic and depends on the amplitude of breathing. The plot in Figure 3.8b which shows the data recorded during the breathhold task, shows small periodic frequency variation which could be related to the cardiac cycle. Also the plot in Figure 3.8a, shows the superposition of low and high temporal frequency periodic field variation, while the high temporal frequency changes are of smaller amplitude.

To gain further understanding of the spatial and temporal behaviour of the frequency variation due to respiratory motion, we can fit a first order polynomial in z (the foot-head direction) to frequency difference between the signal acquired at time t and the

first acquisition:

$$f(z,t) = a(t) \cdot z + b(t) \ . \tag{3.12}$$

Higher degree polynomials are not considered here, but are discussed, for example, by Vannesjo et al. (2015), and Andersen et al. (2016). The best-fitting parameters $b(t)$ and $a(t) \cdot 2\,\mathrm{mm}$ are plotted against time and compared with the previously calculated average frequency variation from the corpus callosum in Figure 3.9b. The length scale of $2\,\mathrm{mm}$ arises from the image resolution in the z-direction.

Impact of field changes due to breathing on the MEGE data By using the information on spatially and temporally varying field perturbations in the real domain we can perform an *in silico* MEGE MRI experiment using following steps:

- **Step 1** Calculate complex signal in the real domain using spatially varying field perturbations of physiological origin at a selected time point;
- **Step 2** From the complex signal in the real domain in **Step 1** calculate a Fourier transform;
- **Step 3** Select a line in the Fourier domain in **Step 2** which is related to the time point in **Step 1**;
- **Step 4** Repeat **Step 1** – **Step 3** until the full image in the Fourier domain is "acquired";
- **Step 5** Use the inverse Fourier transform of **Step 4** to get an image in the real domain.

First, we simulate the spatial and temporal field perturbations. The spatial frequency

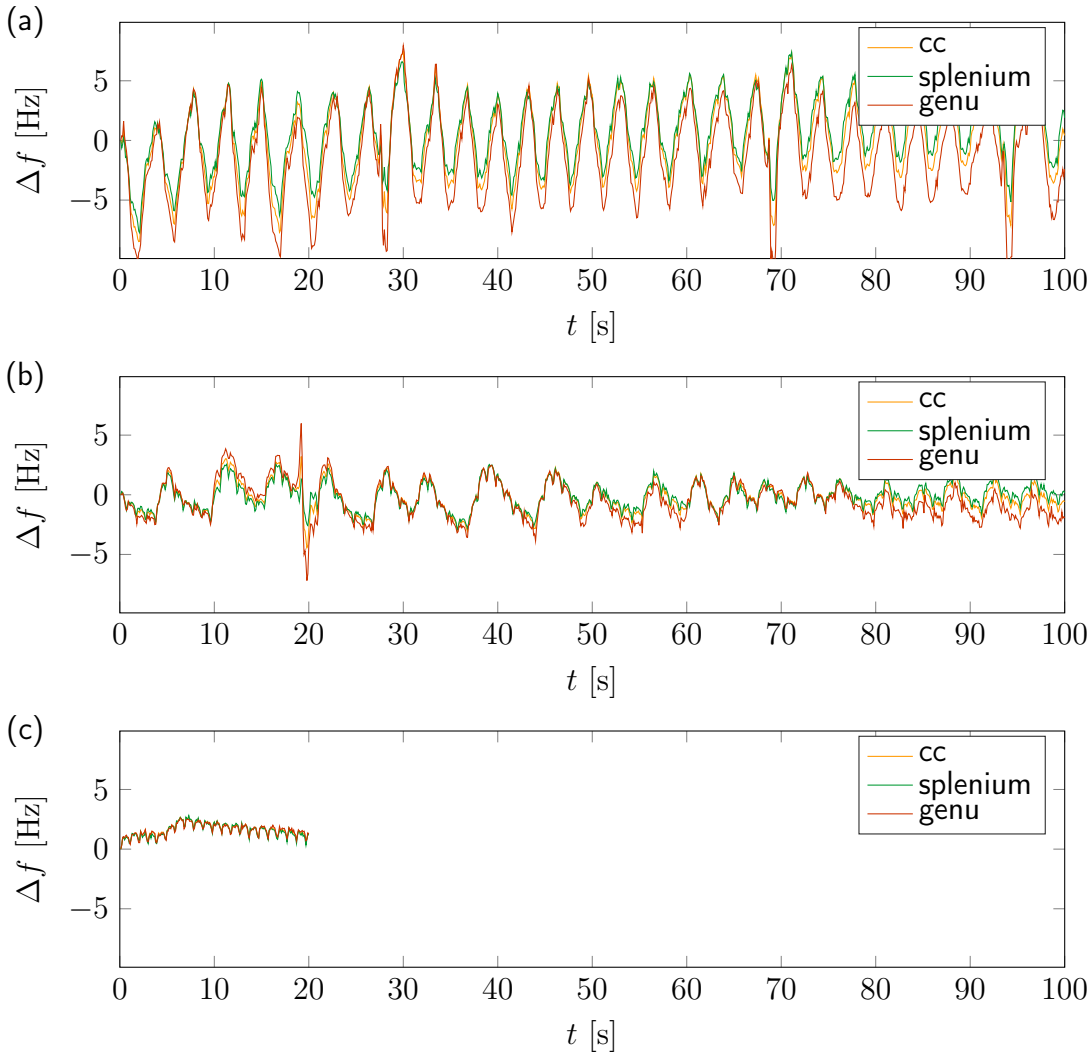


Figure 3.7.: Respiratory motion induces periodic frequency variation within the corpus callosum. The plots show the frequency difference to the first dynamical scan $\Delta f = {}^{\arg(s_m/s_1)}/_{2\pi \mathrm{TE}}$ averaged over three different ROIs: the whole corpus callosum (cc), the splenium of the cc and the genu of the cc, plotted against time. In three separate scans the subject was asked to (i) breath deeply, (ii) breath normally for 2 minutes, and (iii) hold their breath for 20 seconds. The results are shown in (a), (b) and (c), respectively.

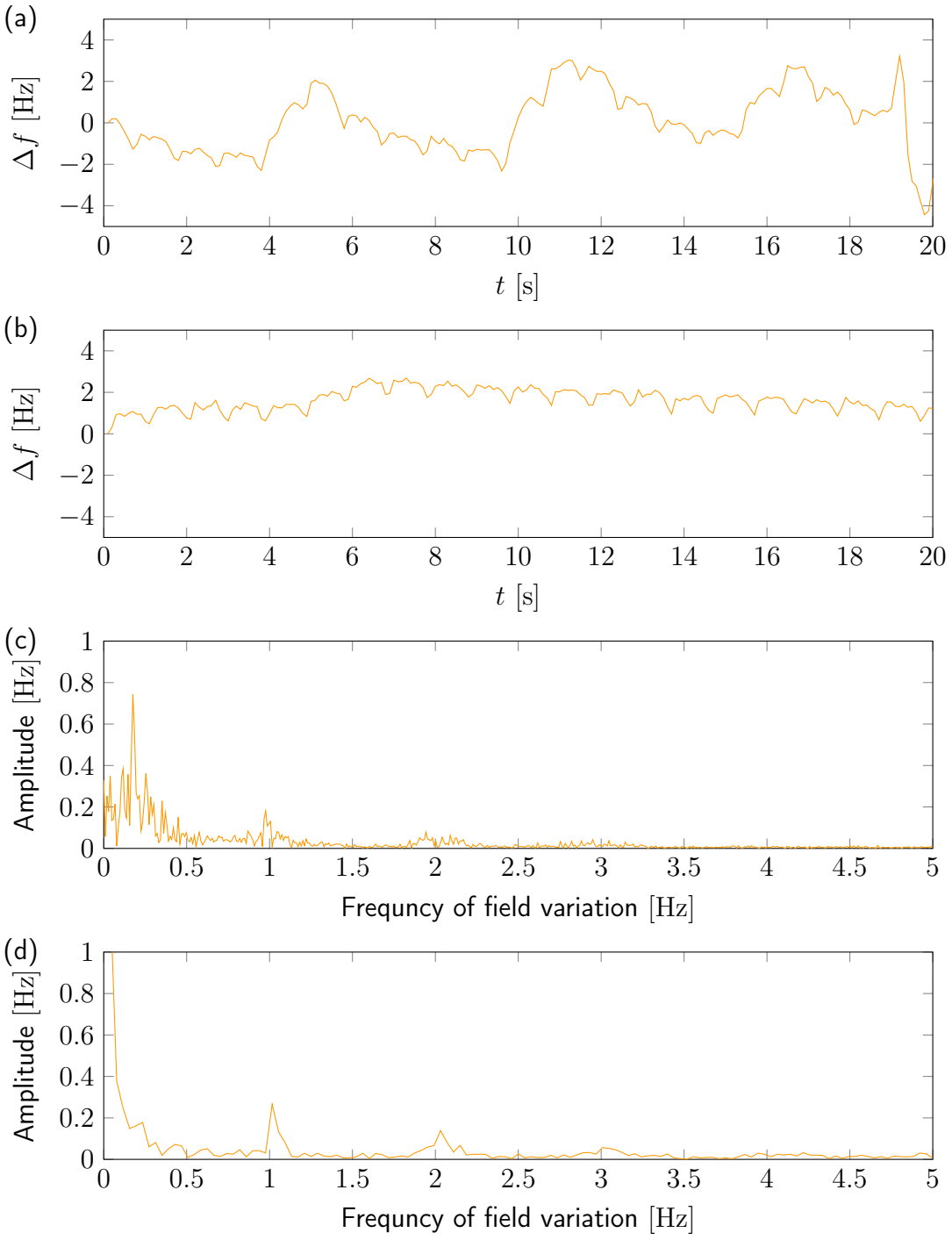


Figure 3.8.: Plots in (a) and (b) show the frequency variation with time from the whole corpus callosum, during normal breathing and breathhold, respectively, plotted over the $20\,\mathrm{s}$ duration of the breathhold. The corresponding Fourier transformations in (c) and (d) of the field variations make visible the amplitude and frequencies of the fluctuations.

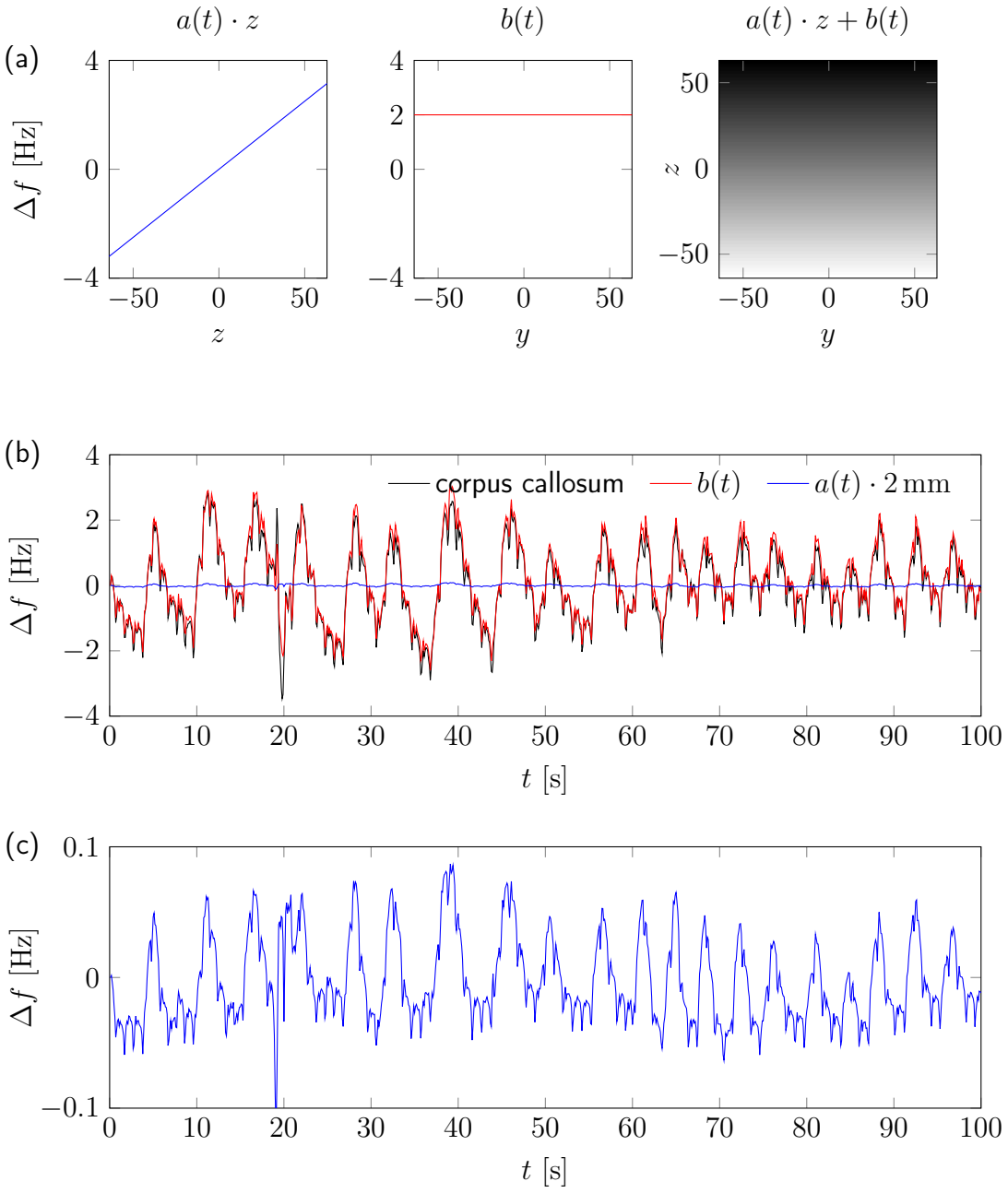


Figure 3.9.: Field variations due to respiratory motion can be approximated as a linear variation in z-direction plus a constant: i.e. as $a(t) \cdot z + b(t)$, as shown in (a). The plot in (b) compares the best fitting parameter $b(t)$, red line, to the frequency variation within the corpus callosum, black line. The plot in (c) shows that the linear term $a(t)$ undergoes periodic changes as well.

variation, $f(z,t)$, to a first approximation is linearly dependent on z in the real domain

$$f(z,t) = a(t) \cdot z + b(t) \ . \tag{3.13}$$

The fitting parameters $a(t)$ and $b(t)$ are time-dependent and depend on the time of acquisition within the respiratory cycle, and therefore can be approximated by periodic functions, for example a sinusoid:

$$a(t) = A \cdot \sin(\theta_t + \theta_0) \ , \tag{3.14}$$

$$b(t) = B \cdot \sin(\theta_t + \theta_0) \ . \tag{3.15}$$

θ_0 indicates the position in the respiratory cycle relative to the scan start, parameters A and B stand for the amplitudes of constant and linear periodic field changes, respectively. The variable θ_t is defined depending on the period, T, of a single respiratory cycle, $\theta_t = {}^{2\pi t}/_{T}$. Therefore the temporal and spatial dependency of the frequency variation, $f(t,z)$ can be written as

$$f(t,z) = (A \cdot z + B) \cdot \sin({}^{2\pi t}/_{T} + \theta_0) \ . \tag{3.16}$$

As we have shown in Section 1.4, one line of k-space is acquired per excitation at multiple gradient-echo times. Furthermore, the acquisition of the mth line of the k-space can be related to the mth repetition time TR_m. Since only spoiled gradient-echo sequence is used the phase is accumulated across each echo train only. We write $\phi_{m,n} = \phi(\mathrm{TR}_m + \mathrm{TE}_n)$ for the phase accumulated at the time of acquisition of the mth line of the k-space of the nth gradient-echo is acquired, which is defined as

$$\phi_{m,n} = \int_{\mathrm{TR}_m}^{\mathrm{TR}_m + \mathrm{TE}_n} 2\pi f(t', z) \, \mathrm{d}t' \ . \tag{3.17}$$

The complex signal is proportional to the exponential of product of the accumulated phase and the imaginary unit, i.e. $S_{m,n} \sim e^{i\cdot\phi_{m,n}}$. The complex signal variation from the MEGE sequence in the real domain due to respiratory motion related to the mth line of the k-space at the nth gradient-echo would thus be modulated by

$$S_{m,n} \sim \exp\left[\int_{\mathrm{TR}_m}^{\mathrm{TR}_m+\mathrm{TE}_n} i2\pi f(t',z)\,\mathrm{d}t'\right] \tag{3.18}$$

$$= \exp\left[-i(A\cdot z+B)\cdot T\cdot\cos\left(\tfrac{2\pi}{T}(\mathrm{TR}_m+\mathrm{TE}_n)+\theta_0\right)\right]$$

$$\times \exp\left[i(A\cdot z+B)\cdot T\cdot\cos\left(\tfrac{2\pi}{T}\mathrm{TR}_m+\theta_0\right)\right]\ . \tag{3.19}$$

This fulfils **Step 1**.

The signal of the mth line of the k-space of the nth gradient-echo $s_{m,n}$ in the Fourier domain is derived from the Fourier transform of the product between signal $S_{m,n}$ and object r, $\mathcal{F}\{r\cdot e^{i\cdot\phi_{m,n}}\}$ (**Step 2**), by picking the mth line (**Step 3**). If we repeat the calculation for each line in k-space, we will get a full MEGE image in the Fourier domain (**Step 4**) which we can then transform into the real domain (**Step 5**) and analyse for the frequency uncertainties due to breathing. The algorithm described here is also shown in a diagram in Figure 3.10.

To have an estimate for the signal distortion and the impact on FDM calculation of res-

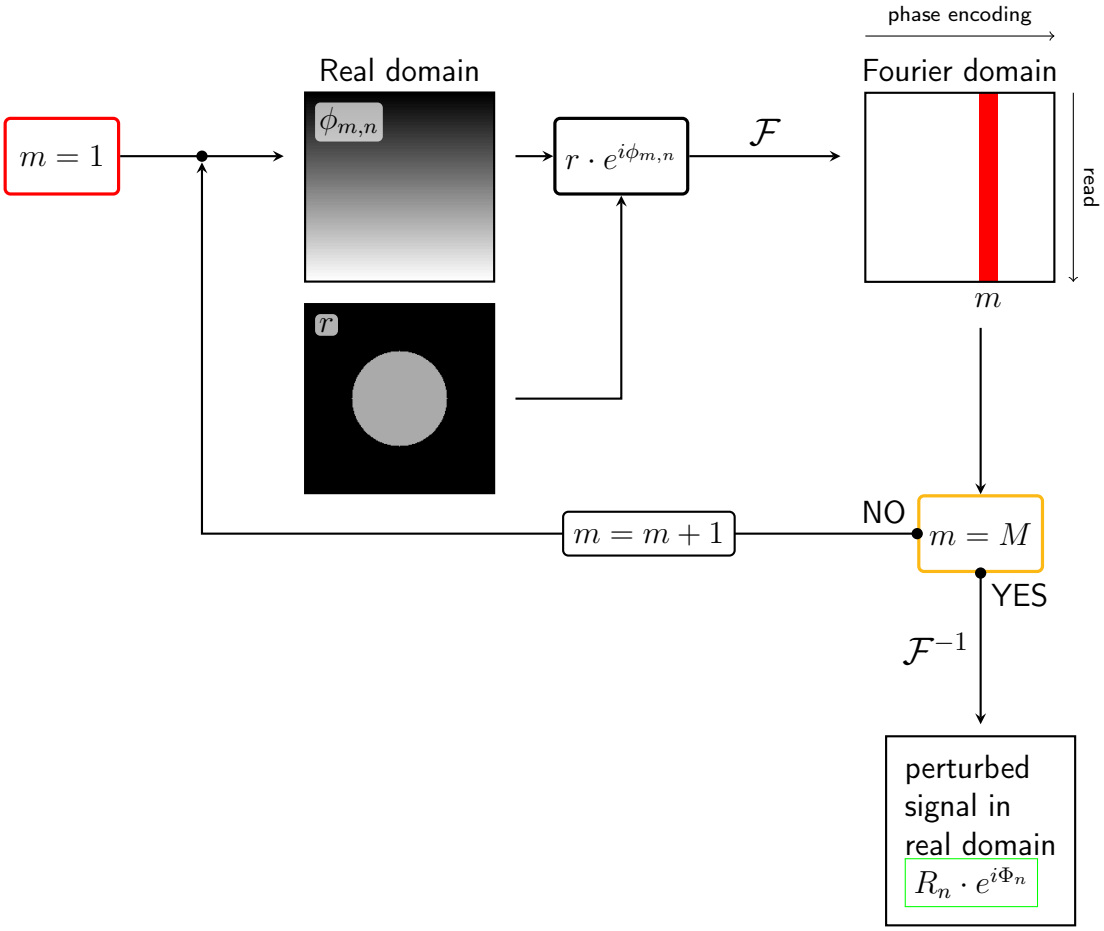


Figure 3.10.: This diagram shows the algorithm to calculate the signal distortion originating from respiration.

piration, we selected the following values for the parameters in (3.19) and Figure 3.10:

$$\begin{aligned} A &= 0.025\,{}^{\mathrm{Hz}}/_{\mathrm{mm}}\ , \\ B &= 2\,\mathrm{Hz}\ , \\ T &= 6\,\mathrm{s}\ , \\ M &= 224\ , \\ N &= 20\ , \\ \theta_0 &= [-{}^{\pi}/_{2},\ -{}^{\pi}/_{4},\ 0,\ {}^{\pi}/_{4},\ {}^{\pi}/_{2}]\ , \end{aligned} \tag{3.20}$$

where the parameters M and N are number of k-space lines and number of echoes, respectively. The parameters A, B, and T in (3.20) were selected based on the experimental data demonstrated in the first part of this section, where we investigated temporal and spatial field perturbations due to physiological motion.

The example of magnitude, phase and FDM distortion for echo times of $6.6\,\mathrm{ms}$ and $44\,\mathrm{ms}$ for $\theta_0 = 0$ is shown in Figure 3.11. The plots in Figure 3.12 show the uncertainty in FDM calculation for three different locations, indicated by red crosses in the images next to each of the plots. From the images and plots it is evident that the error is higher in the interface regions in the phase encoding direction and lower elsewhere. The uncertainty in FDM increases with the echo time. It also varies with the value of θ_0 and depends on the duration of the scan. Especially because of the significant error in the interface regions in phase encoding direction it is important to take respiratory sources of error into account when analysing in vivo data.

The example given here gives us an approximate idea, how respiratory motion can affect phase contrast. From it we can derive, that the uncertainty may increase with the increased amplitude of field perturbation, for example due to gas challenge involving

the increased amount of oxygen in the gas mixture; the uncertainty also increases with the longer scan time, as for example in case of a 3D acquisition instead of a 2D slice.

3.6. Conclusion

We have described Frequency Difference Mapping, an approach which can be used to remove linearly evolving phase associated with non-local field perturbations without corrupting the local non-mono-exponential phase evolution, acquired using unipolar MEGE readout. We suggested a method how FDM can be applied to MEGE data acquired using bipolar readout. This allows us to reduce the echo-spacing and thus increase temporal resolution. We have shown the performance of both methods on unipolar and bipolar MEGE data collected from a phantom. Finally, we considered the respiratory motion as a source of field perturbations and its impact on the MEGE data and on FDM calculation.

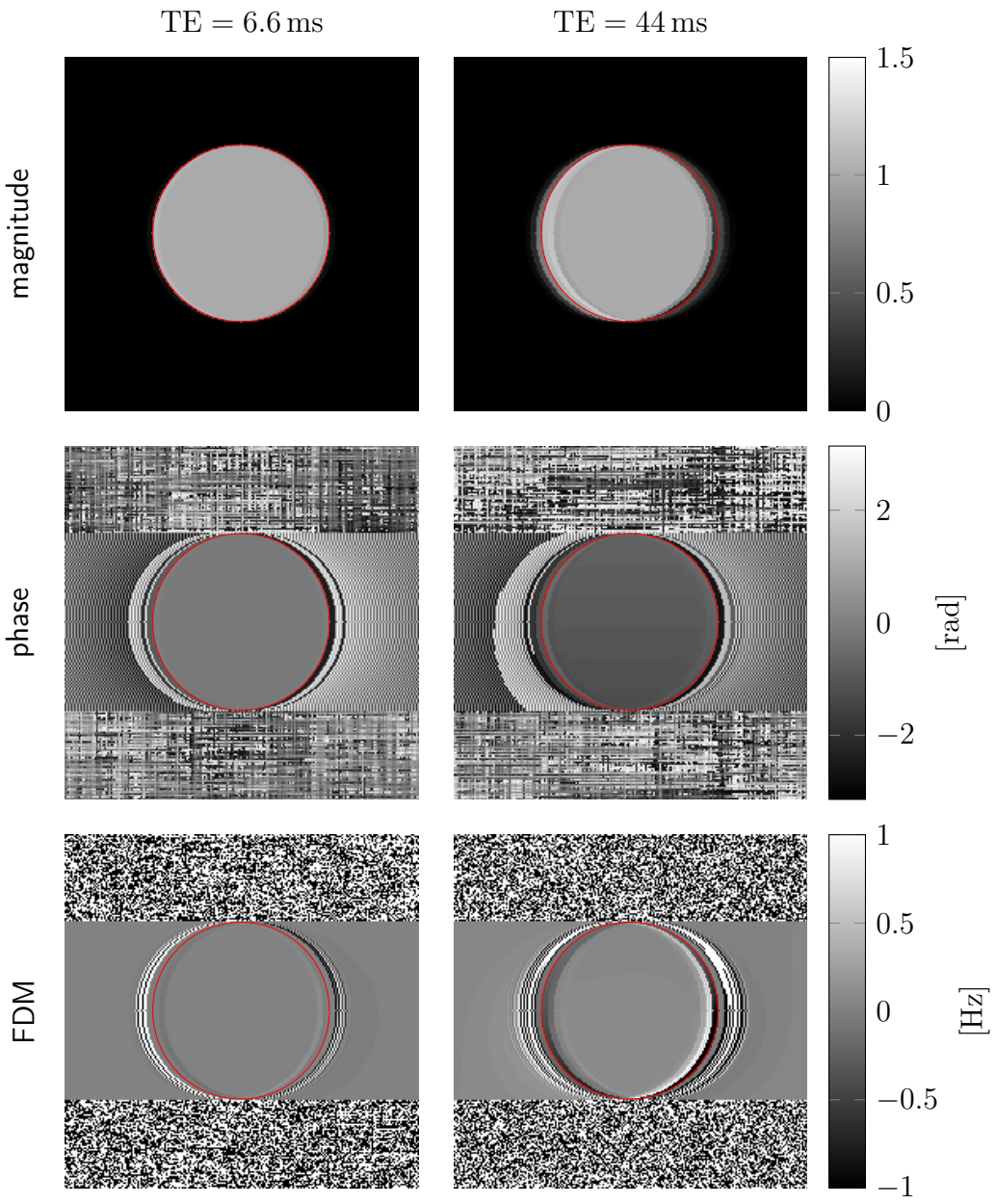


Figure 3.11.: The magnitude, phase and FDM images for the echo times of $6.6\,\mathrm{ms}$ and $44\,\mathrm{ms}$ were calculated using the method displayed in Figure 3.10 for the values for A, B, T, M and N in (3.20) and $\theta_0 = 0$. The red circles indicate the interface area of the object to make the distortion more obvious.

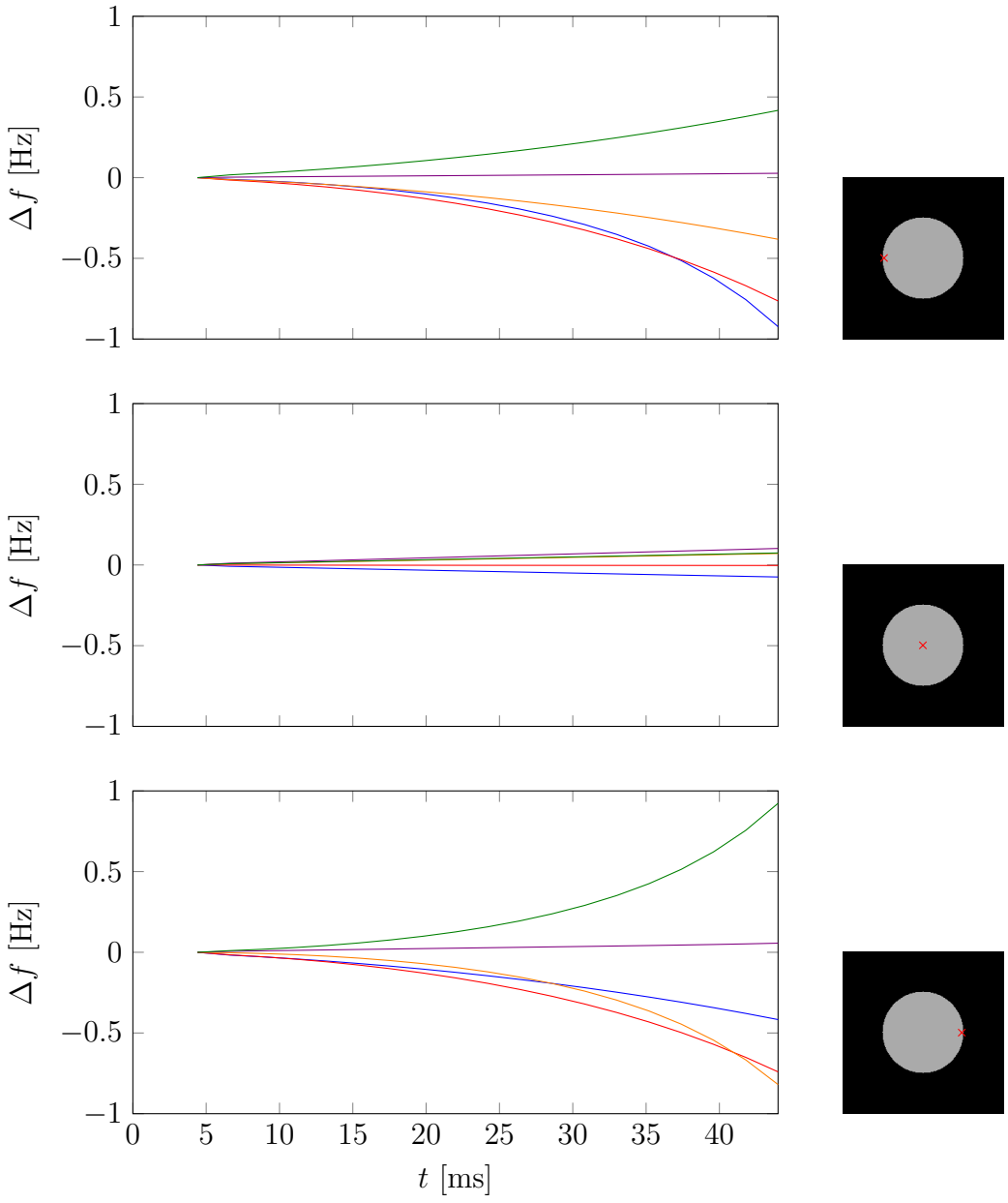


Figure 3.12.: The uncertainty of the FDM calculations in presence of periodically varying magnetic field is plotted for three different regions within the object, indicated with red cross in the images next to the plots. Different line colours stand for different θ_0 values. The uncertainty varies dependent on θ_0 and increases with the echo time.

Part II.

Applications

4. *In vivo* application of 2-compartment model

4.1. Introduction

MRI methods to quantify cerebral venous oxygenation, Y_v, offer a valuable biomarker for tissue metabolism. Existing techniques characterise the magnitude or phase of the intra-vascular signal to measure Y_v, meaning that they are generally limited to studying vessels larger than the image resolution (Lu and Ge (2008); Fan et al. (2014)). Smaller vessels with known geometry can be examined, by modelling the gradient-echo signal decay as a two-pool model containing tissue and venous contributions, Sedlacik et al. (2009). An alternative approach (Driver et al. (2014)) induces a change in perivascular signal phase by altering blood oxygen levels, removing dependence on vessel geometry, however this is also only appropriate for single, well-resolved veins.

We propose that a 2-compartment model of the evolution of signal phase, processed using FDM (Wharton and Bowtell (2012)) can be used to study venous oxygenation and architecture at the microscopic scale. In this chapter we provide a proof-of-concept demonstration of the quantification of Y_v in single visible sub-voxel-sized vessels, and test the sensitivity of the resulting Y_v values to hyperoxia. We will discuss how this

Table 4.1.: Scanning parameters.

Breathing and gas control	$P_{ET}O_2$ [mmHg]	N Subj	echoes	TE_1 [ms]	ΔTE [ms]	TR [ms]	VS [mm^3]	t_{total} [s]
Normal breathing; No gas control	–	3	20	1.5	2.2	100	$1 \times 1 \times 5$	22.4
14 s breath-holds; RespirAct ™	~ 120 ~ 450	1	17	1.36	2.1	60	$1 \times 1 \times 3$	13.4

method can be applied to study microvasculature of cerebral cortex. The complex data demonstrated here were acquired using a unipolar MEGE readout, since a method to correct for inconsistency between the adjacent echoes in data acquired using bipolar MEGE readout was developed later.

4.2. Materials and Methods

Data acquisition Single-slice mid-sagittal unipolar MEGE data were acquired from four healthy subjects ($25.9 \pm 1.7\,\mathrm{y}$, 3 females) using a $7\,\mathrm{T}$ whole-body scanner. MEGE data were collected using the following scanning parameters, first echo time, echo spacing and repetition time: $\mathrm{TE}_1/\Delta\mathrm{TE}/\mathrm{TR} = 1.5/2.2/100\,\mathrm{ms}$, 20 echoes, and voxel size of $1 \times 1 \times 5\,\mathrm{mm}^3$. The fourth subject (male) underwent a gas challenge, during which normoxic (NO) or hyperoxic (HO) gas mixtures were delivered using the RespirAct ™ system so as to modulate the cerebral venous oxygenation levels, Y_v. To reduce the artifacts due to respiratory motion the data for this subject were acquired during a breathhold and the scanning protocol was adapted to limit the time of acquisition of a single $2\mathrm{D}$ image to enable a reasonable time for breathholds of $14\,\mathrm{s}$. The first echo time, echo spacing and repetition time were set to $\mathrm{TE}_1/\Delta\mathrm{TE}/\mathrm{TR} = 1.36/2.1/60\,\mathrm{ms}$, and the number of echoes was reduced to 17 and voxel size was $1 \times 1 \times 3\,\mathrm{mm}^3$. Data for all subjects were averaged over 10 repeats. Scanning parameters for both groups are listed in Table 4.1.

RespirAct ™ (Thornhill Research, Toronto, Canada) is a system which controls end-tidal (ET) gas concentrations in the lungs and blood. A face mask attached to this circuit provided the subject's normoxia ($\mathrm{P_{ET}O_2} \sim 120\,\mathrm{mmHg}$) and hyperoxia ($\mathrm{P_{ET}O_2} \sim 450\,\mathrm{mmHg}$).

Complex signal processing Complex data were processed using the FDM approach described in Chapter 3. For each subject, 8 veins were identified in the magnitude images with $\mathrm{TE} = 20\,\mathrm{ms}$. ROIs were drawn around straight segments of each vein, and the orientation of each vein with respect to $\vec{B}_0$ (represented by angle θ) was estimated. FDM and magnitude data were averaged across each ROI for each echo. For each ROI, the 2-compartment model of complex signal evolution, described in Section 2.2.2, was fitted to the mean FDM data using non-linear least-squares analysis:

$$\begin{aligned} S(t) &= S_{\text{venous}}(t) + S_{\text{tissue}}(t) \\ &= \lambda \cdot e^{-R^*_{2,\text{v}}t} \cdot e^{i\Delta\omega t} + (1-\lambda) \cdot e^{-R^*_{2,\text{t}}t} \,, \end{aligned} \tag{4.1}$$

allowing the estimation of frequency offset, $\Delta\omega$, between the venous and the tissue compartments, the venous signal fraction, λ, and the relative relaxation rate of the venous compartment, $r^*_{2,\text{v}} = R^*_{2,\text{v}} - R^*_{2,\text{t}}$. The signal fractions and the relaxation rates were restricted to non-negative values, no limits were applied to the frequency offsets.

Quantification of $\mathbf{Y_v}$ As described in Section 2.2.2, the frequency offset, $\Delta\omega$, between the venous and the tissue compartments, depends on the orientation of the vein to $\vec{B}_0$, θ, and on venous blood oxygenation level, Y_v, as follows (Sedlacik et al.

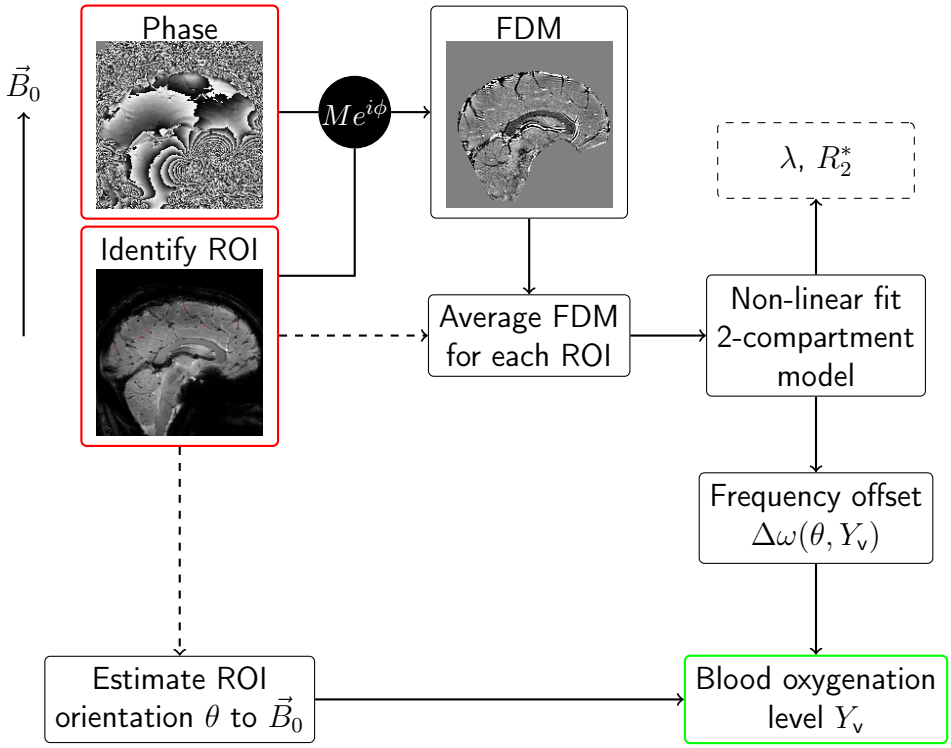


Figure 4.1.: The diagram shows the steps applied to the complex signal data in order to estimate venous blood oxygenation levels.

(2009)):

$$\Delta\omega(\theta, Y_v) = \frac{1}{2} \cdot \gamma B_0 \cdot \Delta\chi_{do} \cdot \mathrm{hct} \cdot (1 - Y_v) \cdot \left[\cos^2\theta - \frac{1}{3}\right] \quad . \tag{4.2}$$

To estimate the venous blood oxygenation level, Y_v, from the frequency offset, $\Delta\omega$, we assumed a hematocrit value of $\mathrm{htc} = 0.45$ and a susceptibility difference between tissue and fully deoxygenated blood of $\Delta\chi_{do} = 2.26\,\mathrm{ppm}$.

The steps for the complex signal processing and Y_v quantification are summarised in Figure 4.1.

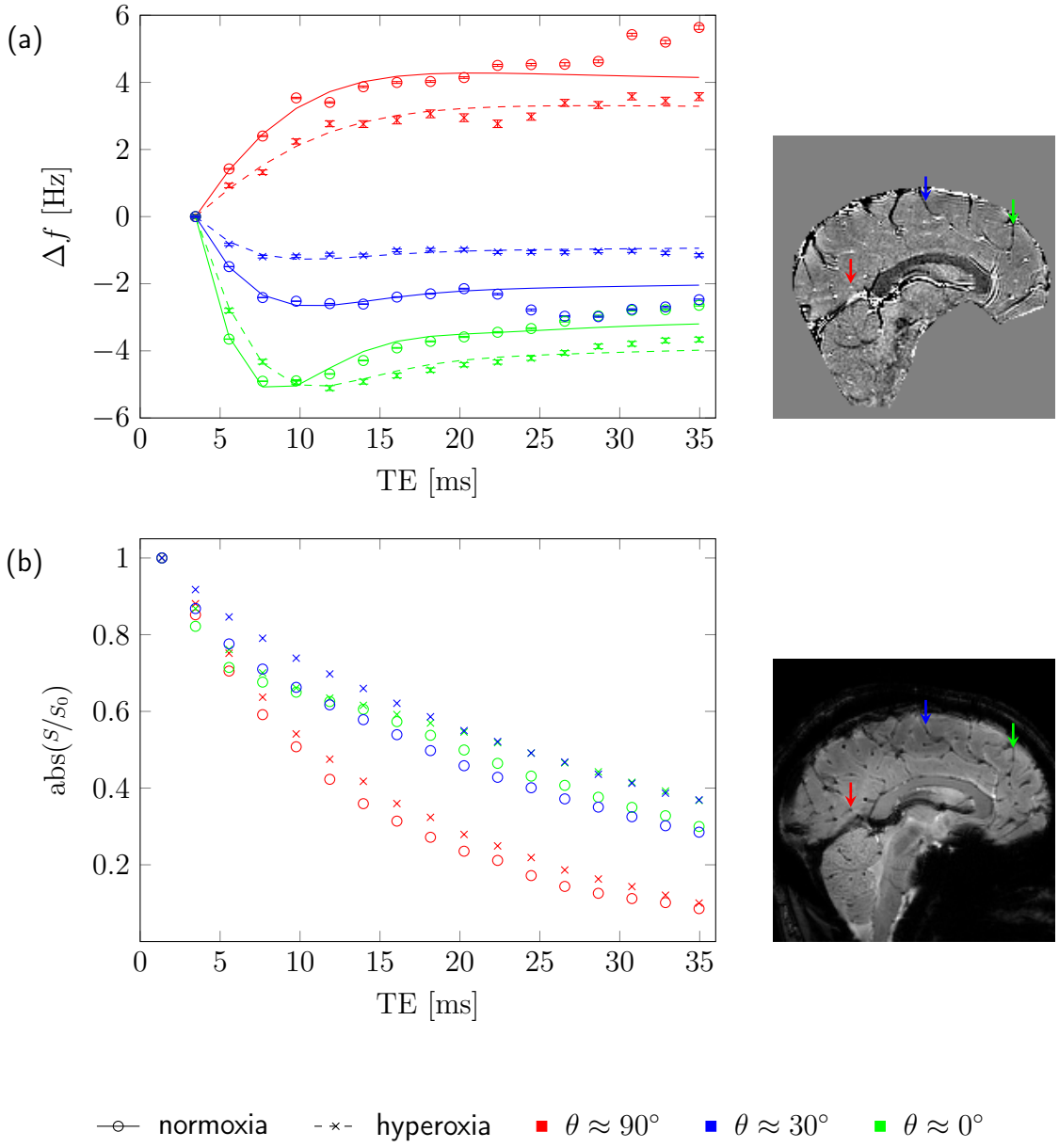


Figure 4.2.: Evolution of the signal phase from an ROI containing a single vein, processed using FDM (a) and the corresponding magnitude decay (b) for the data from normoxia (circles for the data points and solid lines for the fit) and hyperoxia (crosses for the data points and dashed lines for the fit) scans with the associated results of the two-compartment model fit. Different colors indicate different vein orientations to $\vec{B}_0$: red for nearly perpendicular, green for nearly parallel, and blue for intermediate orientations. FDM data shows a better orientation contrast than magnitude data.

4.3. Results

Comparison of the signal evolution during normoxia and hyperoxia gas challenges for three different ROIs is shown in Figure 4.2. The ROIs selected for this example are indicated by arrows of corresponding colour in the FDM and magnitude images next to the plots. FDM data, Figure 4.2a, show a better orientation contrast than the magnitude data, Figure 4.2b. The lower contrast and slower decay in FDM data recorded during the hyperoxia gas challenge are consistent with the higher oxygenation levels. Figure 4.3 shows the frequency offsets from 8 ROIs estimated by fitting the 2-compartment model to FDM data during normoxia (red data points and curves) and hyperoxia (blue data points and curves) scans, plotted as a function of θ, along with the fitted curves. The lower ampitude of the fitted curve for hyperoxia data is consistent with higher Y_{v}. The oxygenation levels estimated from these plots were $Y_{\mathrm{v}} = 0.30 \pm 0.05$ for normoxia, and $Y_{\mathrm{v}} = 0.45 \pm 0.07$ for hyperoxia. Finally, the distribution of the values for oxygenation levels Y_{v} and venous blood signal fractions λ for all subjects are presented in Figure 4.4.

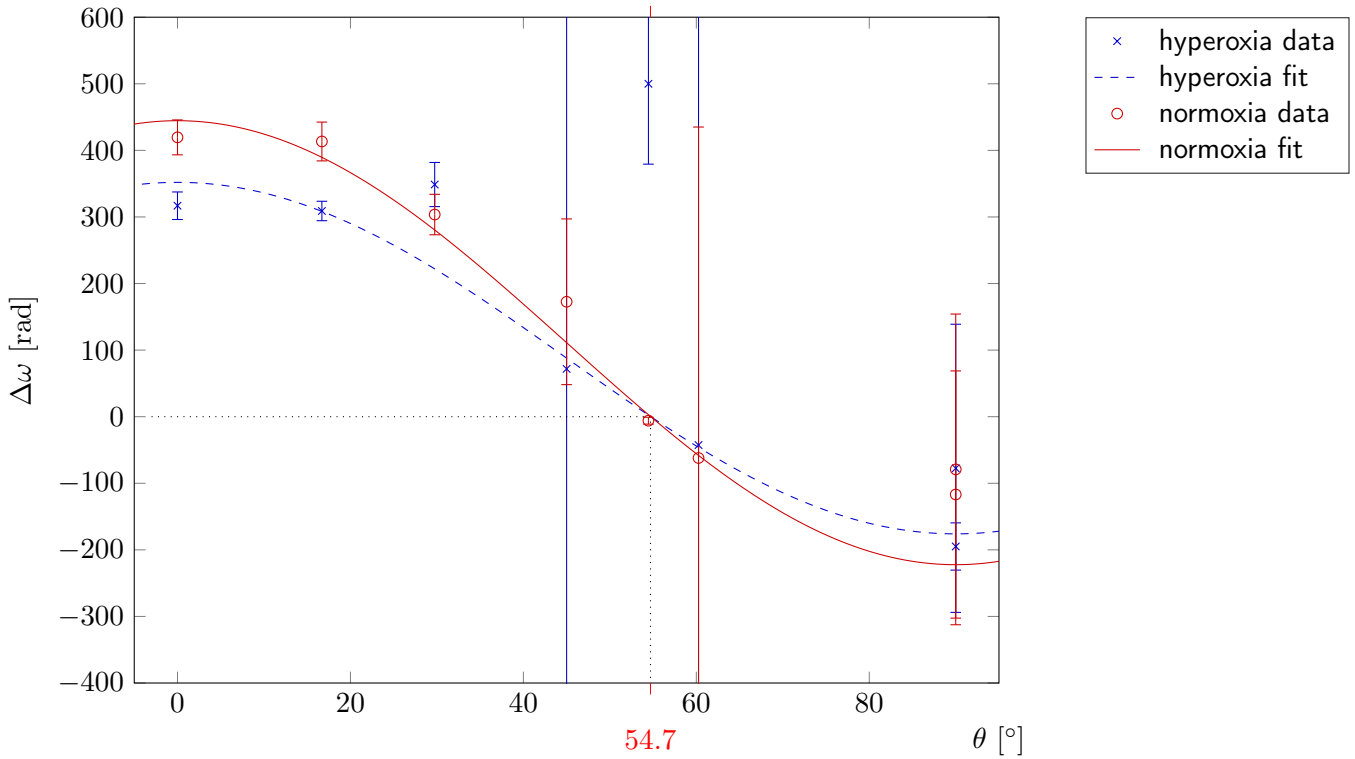


Figure 4.3.: Data from 8 ROIs identified in normoxia (red) and hyperoxia (blue) scans on a single subject are represented, along with best fit curves. The lower ampitude of the fitted curve for hyperoxia data is consistent with higher Y_v. The area around $\theta = 54.7°$ is ill-conditioned, since $[\cos^2\theta - 1/3] \to 0$, causing inaccurate fitting and a large uncertainty in $\Delta\omega$.

4.4. Discussion

Quantification of Y_v Several venous ROIs in Figure 4.4 produced non-physiological values above 1, as well as implausible blood volume measurements. Figure 4.3 shows that inaccurate fitting of $\Delta\omega$ occurs when θ approaches the magic angle, $54.7°$, which reflects a fundamental limitation when studying susceptibility effects. ROIs containing veins with orientation to $\vec{B}_0$ approaching the magic angle are indicated in Figure 4.4 and correlate with non-physiological values for Y_v. Other ROIs demonstrate more reasonable agreement with expected values ranging from $Y_v = 0.49 \ldots 0.72$ (Lu and Ge (2008), Sedlacik et al. (2009), Fan et al. (2014), and Driver et al. (2014)). Shorter echo times, as it has been suggested in Chapter 5, as well as more robust fitting procedures and measurement of hematocrit would help to improve estimation of both λ and Y_v.

Sensitivity to hyperoxia and orientation In the combined data of Figure 4.3, we observe an increase in Y_v during hyperoxia, as expected, demonstrating our method is sensitive to oxygenation changes. This increase translates to a reduction in $\Delta\omega$, which is manifested as a reduced frequency difference at longer TE_n values in Figure 4.2.

Limitations and future work Higher through-plane resolution and greater coverage would improve the estimation of vessel geometry, thus improving the accuracy of quantification. Breath-holding reduced phase artefacts, but also limited the acquisition time and thus resolution/coverage in this study. This new technique should now be validated against existing methodologies for single, sub-voxel veins; however, it can also theoretically be expanded to model venous microstructure. Although signal models typically assume small vessels in brain tissue can be described as randomly oriented

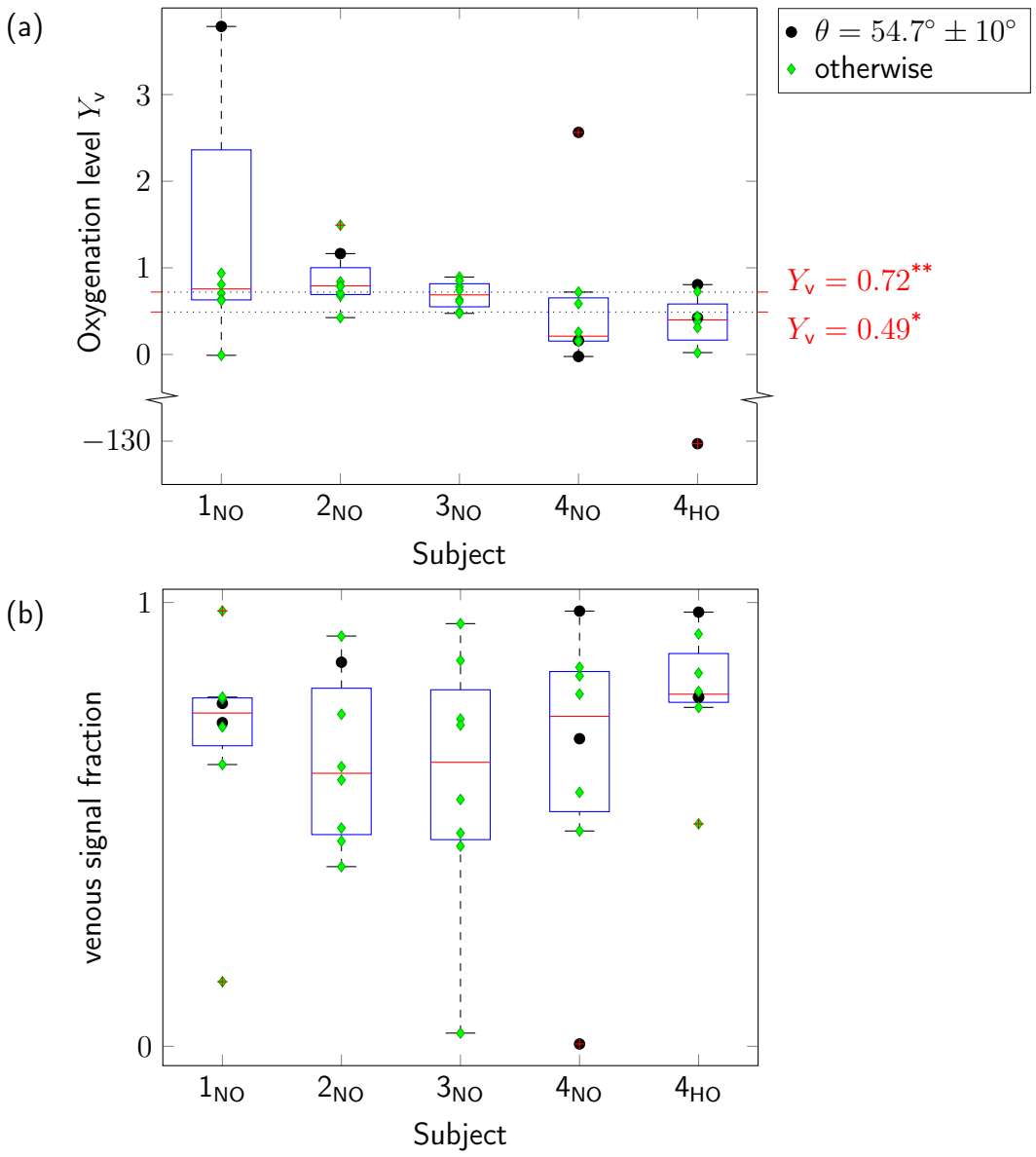


Figure 4.4.: Boxplot showing fitted values of blood oxygenation levels (a) and volume fractions (b) for 8 ROIs defined in each scan. Reference values for Y_v from * Sedlacik et al. (2009) and ** Fan et al. (2014) are indicated.

cylinders (He and Yablonskiy (2007)) any alignment in the orientation of these cylinders would produce a frequency offset between the intravascular and tissue pools. In future we aim to adapt the methods presented here and in Chapter 5 to assess whether there is coherent venous orientation in the cortical ribbon of grey matter, and whether useful oxygenation diagnostics can be mapped across the brain using FDM data.

4.5. Conclusion

We have demonstrated *in vivo* that local phase evolution from a voxel containing venous and tissue compartments is sensitive to modulation of venous blood oxygenation and to the vein orientation to $\vec{B}_0$. Due to short T_2^* ($< 10\,\mathrm{ms}$) of venous blood, this technique could benefit from a better temporal resolution and better estimation of the vessel orientation.

This chapter has motivated Chapter 5, where we demonstrate a phantom model used to better understand the complex signal in the presence of two compartment without limitations of *in vivo* experiment. Using the results from this chapter and Chapter 5 we aim to probe the the alignment of cerebral microvasculature in the future.

5. Verification of the 2-compartment model on a phantom

5.1. Introduction

In Section 2.2 we described how the magnetisation of a sub-voxel venous compartment can be modelled using infinite cylinder model (ICM), and derived a two-compartment model of complex signal evolution in Section 2.2.2. Sedlacik et al. (2009) have estimated the venous blood oxygenation levels, Y_{v}, from small cerebral veins of known orientation to $\vec{B}_0$, by simulating the magnetisation-time-course using ICM, and fitting it to the measured signal decay acquired at $1.5\,\mathrm{T}$. It is obvious that an accurate estimation of Y_{v} from the frequency offset ω between the venous and tissue compartments requires knowledge of vein orientation with respect to magnetic field. The phase of the local signal evolution, in contrast to its magnitude, is sensitive to the sign of ω, and therefore provides the important information in investigation of the cerebral venous microstructure *in vivo*. Since the local phase evolution is dominated by the large-length-scale field perturbations from the non-local sources, a method allowing

to remove these effects without corrupting the local phase evolution is required. The frequency difference mapping described in Chapter 3 is such a method.

In this chapter we introduce a phantom model, which can allow us to better understand the information carried by the complex signal in the presence of two compartments. We demonstrate the application of the frequency difference mapping on its complex signal and compare the information carried by the phase and the magnitude data. Further, we identify the limitations of the proposed 2-compartment model. Finally, we then discuss how the newly acquired knowledge can be translated to an in-vivo study.

5.2. Phantom design

Desired NMR properties Our aim was to prepare a phantom which can be used for verification of the 2-pool model and that is based on known geometry and composition. In order to imitate the in-vivo NMR properties at $7\,\mathrm{T}$ as closely as possible, we consider the reference values listed in Table 5.1. As it has been discussed in Section 2.2.2, the susceptibility value of fully deoxygenated blood, $\Delta\chi_{\mathsf{do}} = 3.431 \pm 0.075\,\mathrm{ppm}$ (Jain et al. (2012)), allows us an approximate estimation of the venous blood susceptibility, assuming hematocrit level of $\mathrm{hct} = 0.5$ and an oxygenation level of $Y = 0.5$: $\Delta\chi = \mathrm{hct} \cdot (1 - Y) \cdot \Delta\chi_{\mathsf{do}} \approx 0.9\,\mathrm{ppm}$.

Phantom composition The phantom is composed of thin long capillaries filled with paramagnetic solution which are placed parallel to each other in a non-paramagnetic bath. The capillaries have to be long and thin to allow the infinite cylinder approximation to be used. The outer shell of the phantom has to be spherical, to reduce the field perturbation due to the interface with the air outside the phantom. For external material and the solvent we selected water, since it has similar magnetic prop-

Table 5.1.: Reference values for NMR properties of brain tissue at $7\,\mathrm{T}$.

Tissue	χ [ppm] cgs	χ [ppm] SI	T_2^* [ms]	T_1 [ms]	f_{vascular}
Venous blood	0.273 ± 0.006[a]	3.431 ± 0.075	≤ 10[b]	2450 ± 110[c]	-
Grey matter			33.2 ± 1.3[d]	1939 ± 149[e]	$5\,\%$
White matter			26.8 ± 1.2[d]	1126 ± 97[e]	$2\,\%$

[a] deoxygenated blood sample Jain et al. (2012)
[b] Yacoub et al. (2001); Blockley et al. (2008)
[c] Rane and Gore (2013)
[d] Peters et al. (2007)
[e] Wright et al. (2008)

Table 5.2.: Susceptibility values derived for two iron concentrations based on the proportionality factor estimated experimentally by Zheng et al. (2013): $1.10\,{}^{\mathrm{ppb}}/_{\mu\mathrm{g/ml}}$.

Iron concentration	$\rho_{\text{Fe}} = 2\,\mathrm{mg/ml}$	$\rho_{\text{Fe}} = 1\,\mathrm{mg/ml}$
Susceptibility	$\Delta\chi = 2.2\,\mathrm{ppm}$	$\Delta\chi = 1.1\,\mathrm{ppm}$

erties as brain tissue and is diamagnetic at room temperature with a susceptibility of $-9.04 \cdot 10^{-6}$ in SI units, Arrighini (1968). The material for the capillaries must therefore have similar magnetic properties to water. Borosilicate glass (trade names Pyrex® and Duran®) is diamagnetic and has a susceptibility of $\chi = -11.0 \cdot 10^{-6}$ (SI units) at room temperature, Doty et al. (1998). For the internal compartment we used a ferritin solution taken from equine spleen from Sigma-Aldrich®. The ferritin solution comes with an iron concentration of $6.92\,\mathrm{mg/ml}$. We dissolved it in water in proportions $1_{\text{ferritin}} : 2.46_{\text{water}}$ and $1_{\text{ferritin}} : 5.92_{\text{water}}$ for the iron concentrations of $\rho_{\text{Fe}} = 2\,\mathrm{mg/ml}$ and $\rho_{\text{Fe}} = 1\,\mathrm{mg/ml}$, respectively. The values for the susceptibility difference $\Delta\chi$ can be estimated from the iron concentration using proportionality factor estimated experimentally by Zheng et al. (2013) for ferritin from the same supplier: $1.10\,{}^{\mathrm{ppb}}/_{\mu\mathrm{g/ml}}$, see Table 5.2.

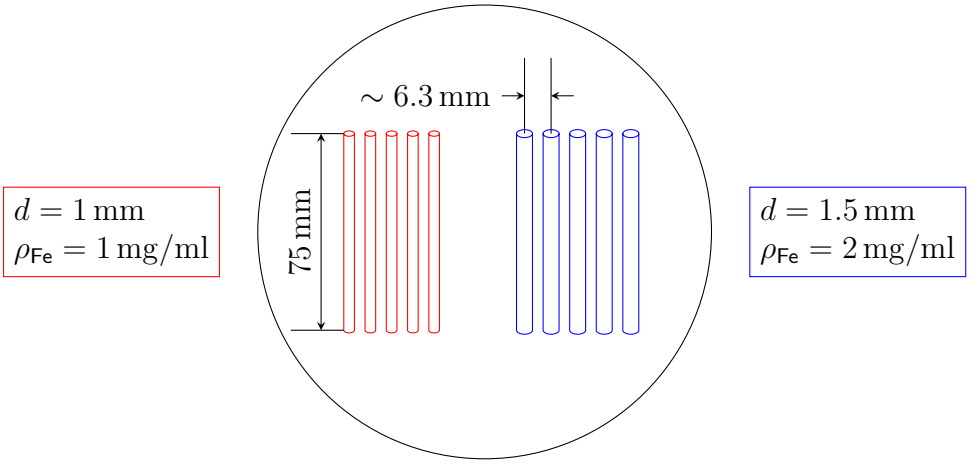
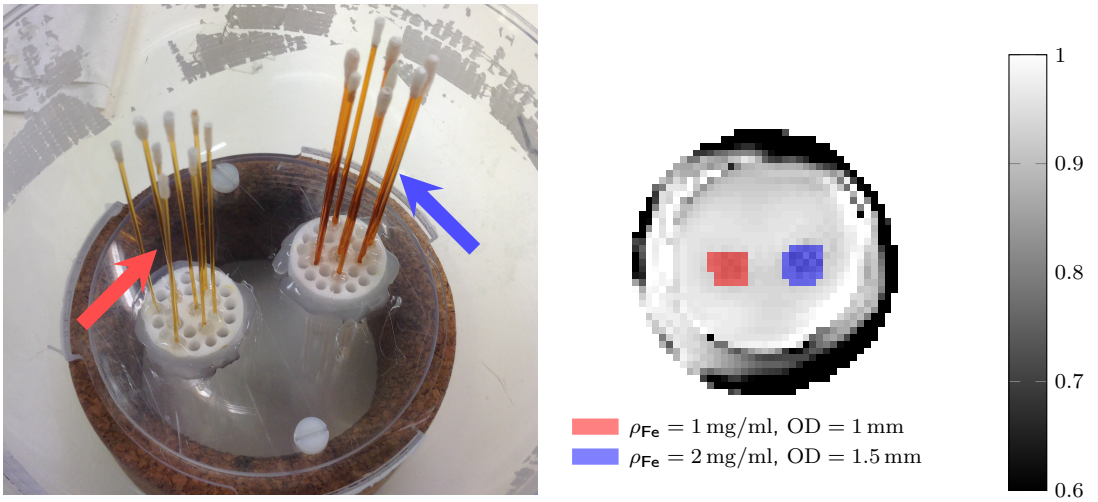


Figure 5.1.: Schematic composition of IronPhan. The average separation between the capillary tubes is similar for both groups and was estimated from the high-resolution ($0.75 \times 0.75 \times 0.75\,\mathrm{mm}^3$) gradient-echo images acquired when the capillaries oriented parallel to $\vec{B}_0$.

The capillary tubes with diameter of $d = 1\,\mathrm{mm}$ and wall thickness of $0.01\,\mathrm{mm}$ were filled with the ferritin solution with iron concentration of $\rho_{\mathrm{Fe}} = 1\,\mathrm{mg/ml}$. The capillary tubes with diameter of $d = 1.5\,\mathrm{mm}$ and wall thickness of $0.02\,\mathrm{mm}$ were filled with the ferritin solution with iron concentration of $\rho_{\mathrm{Fe}} = 2\,\mathrm{mg/ml}$. The capillary tubes were $75\,\mathrm{mm}$ long. Both capillary types were then sealed using Parafilm®, arranged into two groups consisting of 8 tubes each, and glued vertically onto a platform attached to a spherical shell, which was filled with water. The capillaries were placed at approximate distance of 6 to $8\,\mathrm{mm}$ from one another. The phantom is shown schematically in Figure 5.1. The capillaries with $d = 1\,\mathrm{mm}$ and iron concentration of $\rho_{\mathrm{Fe}} = 1\,\mathrm{mg}/\mu\mathrm{l}$ are indicated by the red arrow. The capillaries with $d = 1.5\,\mathrm{mm}$ and iron concentration of $\rho_{\mathrm{Fe}} = 2\,\mathrm{mg}/\mu\mathrm{l}$ are indicated by the blue arrow. Throughout this chapter, the red colour is used to identify smaller capillaries with lower iron concentration and the blue colour is used to identify larger capillaries with higher iron concentration. We will refer to this phantom as "IronPhan".



(a) (b)

Figure 5.2.: Glass capillaries with diameters of $1\,\mathrm{mm}$ and $1.5\,\mathrm{mm}$ are filled with ferritin solution yielding iron concentrations of $\rho_{Fe} = 1\,\mathrm{mg/ml}$ and $\rho_{Fe} = 2\,\mathrm{mg/ml}$, respectively, and positioned parallel to one another, as shown in (a). The corresponding ROIs are shown in (b) on a normalised magnitude image acquired at an echo time of $50\,\mathrm{ms}$.

Table 5.3.: Scanning parameters used to estimate the relaxation times of ferritin solution with two different iron concentrations of $\rho_{\mathsf{Fe}} = 1\,\mathrm{mg/ml}$ and $\rho_{\mathsf{Fe}} = 2\,\mathrm{mg/ml}$. A multi-echo gradient-echo sequence was used to measure the T_2^* values and an inversion recovery sequence was used to measure the T_1 values. Data for each iron concentration were collected in separate sessions.

	MEGE to estimate T_2^*				IR to estimate T_1	
	TE_1 [ms]	$\Delta\mathrm{TE}$ [ms]	TR [ms]	α [°]	TR [ms]	TI-range [ms]
(i) $\rho_{\mathsf{Fe}} = 1\,\mathrm{mg/ml}$	2	1.04	100	10	8000	140 . . . 5000
(ii) $\rho_{\mathsf{Fe}} = 2\,\mathrm{mg/ml}$	2.2	1.38	100	10	8000	140 . . . 5000

Table 5.4.: Relaxation times of pure water and ferritin solution with iron concentrations of $1\,\mathrm{mg/ml}$ and $2\,\mathrm{mg/ml}$ at magnetic field strength of $7\,\mathrm{T}$. Data for each iron concentration were collected in separate sessions (indicated by (i) and (ii) in Table 5.3) and relaxation times for water were estimated from each data set.

		c	T_1 [ms]	T_2^* [ms]
(i) $\rho_{\mathrm{Fe}} = 2\,\mathrm{mg/ml}$	ferritin	1.73	573 ± 88	16.4 ± 0.2
	water	1.94	2851 ± 203	1253 ± 120
(ii) $\rho_{\mathrm{Fe}} = 1\,\mathrm{mg/ml}$	ferritin	1.79	934 ± 30	23.5 ± 0.5
	water	1.89	2214 ± 50	1401 ± 142

Relaxation times at 7 T To characterise the chosen ferritin solutions, we filled two $2\,\mathrm{ml}$ sample tubes (approximate diameter of $10\,\mathrm{mm}$) with ferritin solution with iron concentrations of $\rho_{\mathsf{Fe}} = 1\,\mathrm{mg/ml}$ and $\rho_{\mathsf{Fe}} = 2\,\mathrm{mg/ml}$ and placed them in a water bath within a spherical container. We then performed MEGE and inversion recovery (IR) scans at room temperature at a magnetic field strength of $7\,\mathrm{T}$. The resolution for both scans was $1\,\mathrm{mm}$ isotropic. Further scanning parameters are displayed in Table 5.3. Data for each ferritin concentration were collected in separate sessions.

The collected data were then averaged over three ROIs containing: water, ferritin

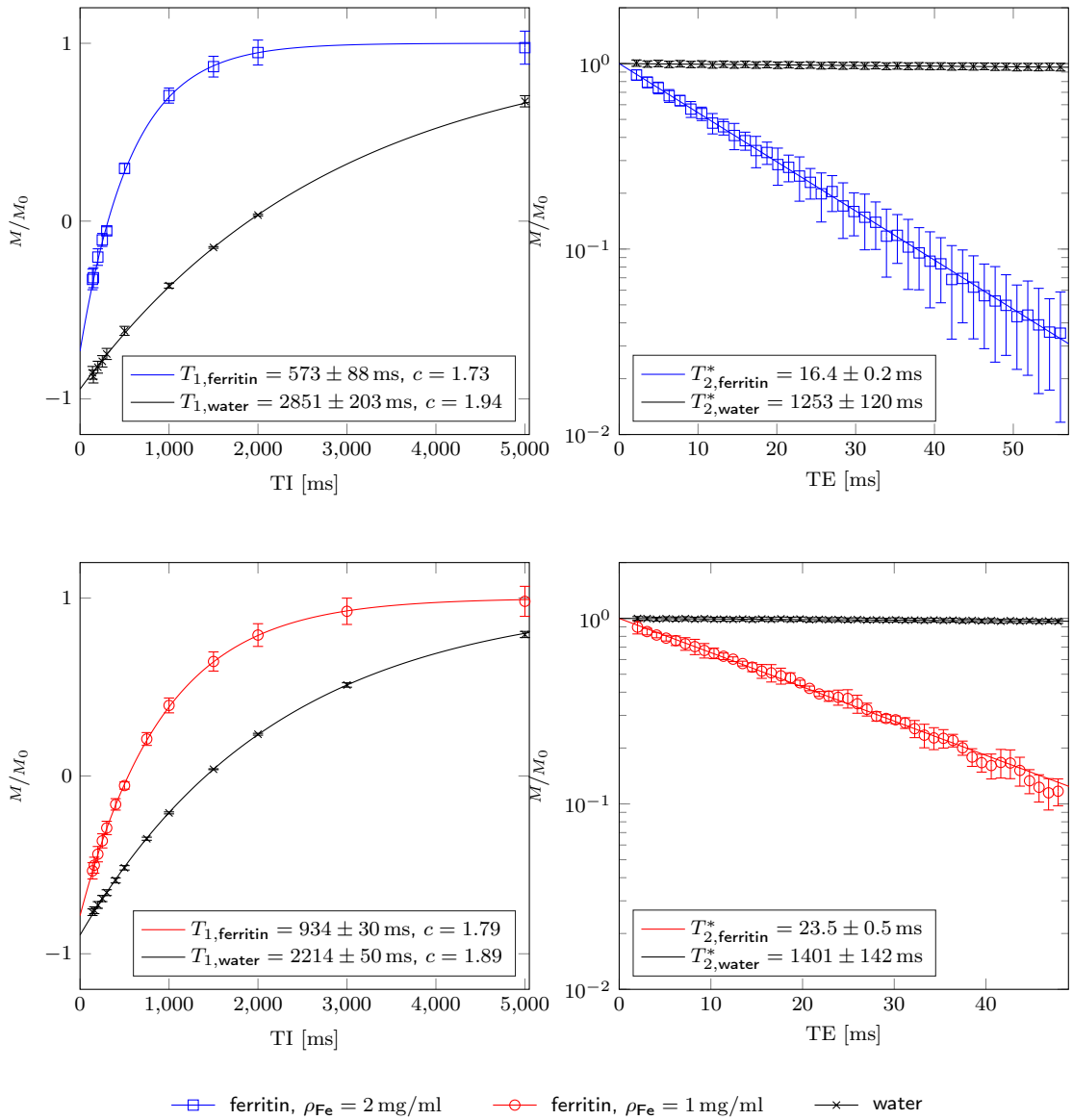


Figure 5.3.: Averaged MEGE (plots on the right) and IR (plots on the left) data from ROIs containing water (×), ferritin solution with iron concentration $\rho_{\text{Fe}} = 2\text{mg}/\mu\text{l}$ (□), and ferritin solution with iron concentration $\rho_{\text{Fe}} = 1\text{mg}/\mu\text{l}$ (○). Solid lines are the best fitting curves modelled as $M/M_0 = 1 - c \cdot e^{-\text{TI}/T_1}$ for IR data and $M/M_0 = e^{-\text{TE}/T_2^*}$ for MEGE data. The corresponding best-fitting parameters for the relaxation times T_1 and T_2^* are detailed in the legend. The data were normalised to M_0 estimated from the fit prior plotting. Longitudinal and transverse relaxation rates are higher for the solution with the higher iron concentration. The transverse relaxation rates for water cannot be estimated accurately at the selected echo times.

solution with iron concentration $\rho_{\mathsf{Fe}} = 1\,\mathrm{mg/ml}$, and ferritin solution with iron concentration $\rho_{\mathsf{Fe}} = 2\,\mathrm{mg/ml}$, for each echo time TE for MEGE scans and each inversion time TI for IR scans. To estimate T_2^* values, a single exponential function was fitted to the MEGE signal decay:

$$M = M_0 \cdot e^{-\mathrm{TE}/T_2^*} \ . \tag{5.1}$$

To estimate the T_1 values we fitted a three-parameter model to the IR signal evolution:

$$M = M_0 \cdot (1 - c \cdot e^{-\mathrm{TI}/T_1}) \ . \tag{5.2}$$

The MEGE and IR signal evolution for each of three ROIs, as well as the best-fitting curves, are displayed in Figure 5.3. The MEGE and IR data were normalised by M_0, which was estimated from the fit, prior to being plotted. The best fitting values for longitudinal and transverse relaxation times for each of three ROIs are given in Table 5.4. As expected, the ferritin solution with the higher iron concentration of $\rho_{\mathsf{Fe}} = 2\,\mathrm{mg/ml}$ showed faster relaxation rates than that of the ferritin solution with iron concentration of $\rho_{\mathsf{Fe}} = 1\,\mathrm{mg/ml}$. The selected echo times are too short for a precise estimation of the relaxation times of water. The values c from the three parameter IR model reflect the quality of the signal inversion. Water signal is not fully inverted since the water signal is not fully recovered at the repetition time of $\mathrm{TR} = 8\,\mathrm{s}$. The signal from the ferritin solution will fully recover at this repetition time, but its off-resonance frequency does not enable optimal inversion of the magnetisation.

While the solution with the lower iron concentration provides susceptibility values similar to those of venous blood, it has a lower rate of transverse relaxation than that of venous blood at $7\,\mathrm{T}$. The rate of transverse relaxation is higher for the higher iron concentration, but still lower than that of venous blood. The rate of transverse re-

laxation could be increased by using higher concentration of ferritin. This would also, however, increase the susceptibility and, therefore, increase the maximum relative frequency offset. Consequently, shorter echo spacings would be necessary for evaluation of the signal evolution. This point is discussed in further detail in Section 5.3.3.

5.3. Complex signal from the phantom

5.3.1. Materials and methods

Scanning protocol The IronPhan phantom was placed into the bore of the whole-body $7\,\mathrm{T}$ scanner with the capillaries lying in the xz plane, where the x, y, and z axes corresponding to the left-right, anterior-posterior, and head-foot directions. The static magnetic field $\vec{B}_0$ is along the z-axis. The capillaries were then scanned at 14 different orientations ($0°$ - $90°$) with respect to the static magnetic field $\vec{B}_0$, achieved by rotating the phantom around the x-axis, while keeping the capillaries in the xz plane. The set-up is shown schematically in Figure 5.4.

The scanning protocol for each orientation included the acquisition of two low-resolution ($4\,\mathrm{mm}$ isotropic) single-slice, MEGE scans and one high-resolution ($0.75\,\mathrm{mm}$ isotropic) multi-slice gradient-echo scan. For each MEGE sequence, 100 gradient echoes were acquired at low excitation angle of $\alpha = 10°$ using bipolar gradient echo readout with first echo time, echo spacing and repetition time values of $\mathrm{TE}_1/\Delta\mathrm{TE}/\mathrm{TR} = 1.1/0.6/100\,\mathrm{ms}$. The voxel size of $4 \times 4 \times 4\,\mathrm{mm}^3$ for the MEGE scans was chosen so that each voxel contains a mixture of ferritin filled capillaries and surrounding water. The difference between the two MEGE scans was a reversal of the polarity of the readout gradients. Each scan was repeated five times. The data were acquired from a slice positioned transverse to the capillaries' axis, cutting through the centre of the

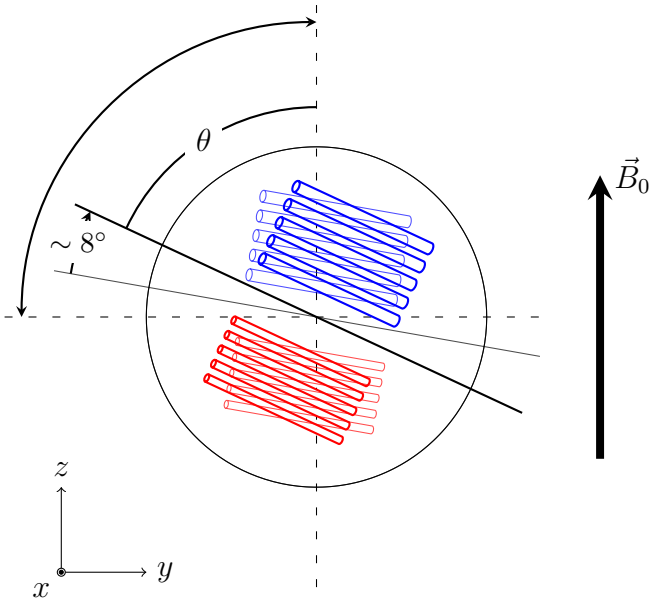


Figure 5.4.: Schematic illustration of the experimental setup. The capillary tubes lie in the yz plane and the phantom is rotated around the x-axis to achieve 14 different orientations of the tubes to $\vec{B}_0$

capillaries. The high-resolution gradient echo data were collected from 45 slices at the echo time $\mathrm{TE} = 30\,\mathrm{ms}$. The slice orientation and position for the high-resolution gradient echo was kept the same for all phantom orientations and used to evaluate the orientation of the capillaries with respect to $\vec{B}_0$.

Data processing The real and imaginary data from the two MEGE scans were averaged across repeats and combined to form the complex signal $S^{\pm}(\mathrm{TE}_n) = \overline{\Re(S^{\pm})} + i \cdot \overline{\Im(S^{\pm})}$ for each echo n. The $+$ and $-$ signs indicate the signals which were acquired with the opposite readout gradient polarities. The product of S^{+} and S^{-} was processed using the frequency difference mapping (FDM), the expression in Eq. (3.10). Two ROIs containing the two different types of capillaries were identified for each of 14 orientations from the normalised magnitude image at the echo time of $50\,\mathrm{ms}$, as

shown in Figure 5.2b. The angle θ between the magnetic field and the capillaries was estimated for each orientation from the high-resolution, single gradient echo $3\mathrm{D}$ scans. The FDM data and the magnitude data were averaged over each region of interest (ROI) for each orientation and each echo time; the magnitude data were then normalised by the first echo. The signal evolution was modelled using 2-compartment model of complex signal evolution:

$$\begin{aligned} S(t) &= F_{\mathsf{water}}(t) + F_{\mathsf{ferritin}}(t) \\ &\sim (1-A)\cdot e^{-R^*_{2,\mathsf{water}}t} + A\cdot e^{-R^*_{2,\mathsf{ferritin}}t}\cdot e^{i\omega t}\ . \end{aligned} \tag{5.3}$$

The 4 fitted parameters were the relaxation rates for water and ferritin, $R^*_{2,\mathsf{water}}$ and $R^*_{2,\mathsf{ferritin}}$, respectively, the frequency offset between both compartments ω, and the signal fraction of the ferritin compartment A. We performed non-linear least squares analysis on FDM and magnitude data both separately and simultaneously. The FDM is insensitive to the absolute values of the effective transverse relaxation times R^*_2 of water and ferritin: therefore, only the difference in the rate of relaxation $r^*_{2,\mathsf{ferritin}} = R^*_{2,\mathsf{ferritin}} - R^*_{2,\mathsf{water}}$ can be obtained from the FDM data. The signal fractions and the relaxation rates of water, $R^*_{2,\mathsf{water}}$ were restricted to non-negative values, the difference in the rate of relaxation, $r^*_{2,\mathsf{ferritin}}$, were restricted to values between 10 and $100\,\mathrm{s}^{-1}$, no limits were applied to the frequency offsets. In addition to characterising the ROI averaged data, the FDM data were also analysed voxelwise.

5.3.2. Results

ROI averaged data The best-fitting values for A, ω, $R^*_{2,\mathsf{ferritin}}$, and $R^*_{2,\mathsf{water}}$ obtained from fitting FDM, normalised magnitude, and both data types simultaneously are plotted against the angle θ in Figures 5.5, 5.6 and 5.7, respectively.

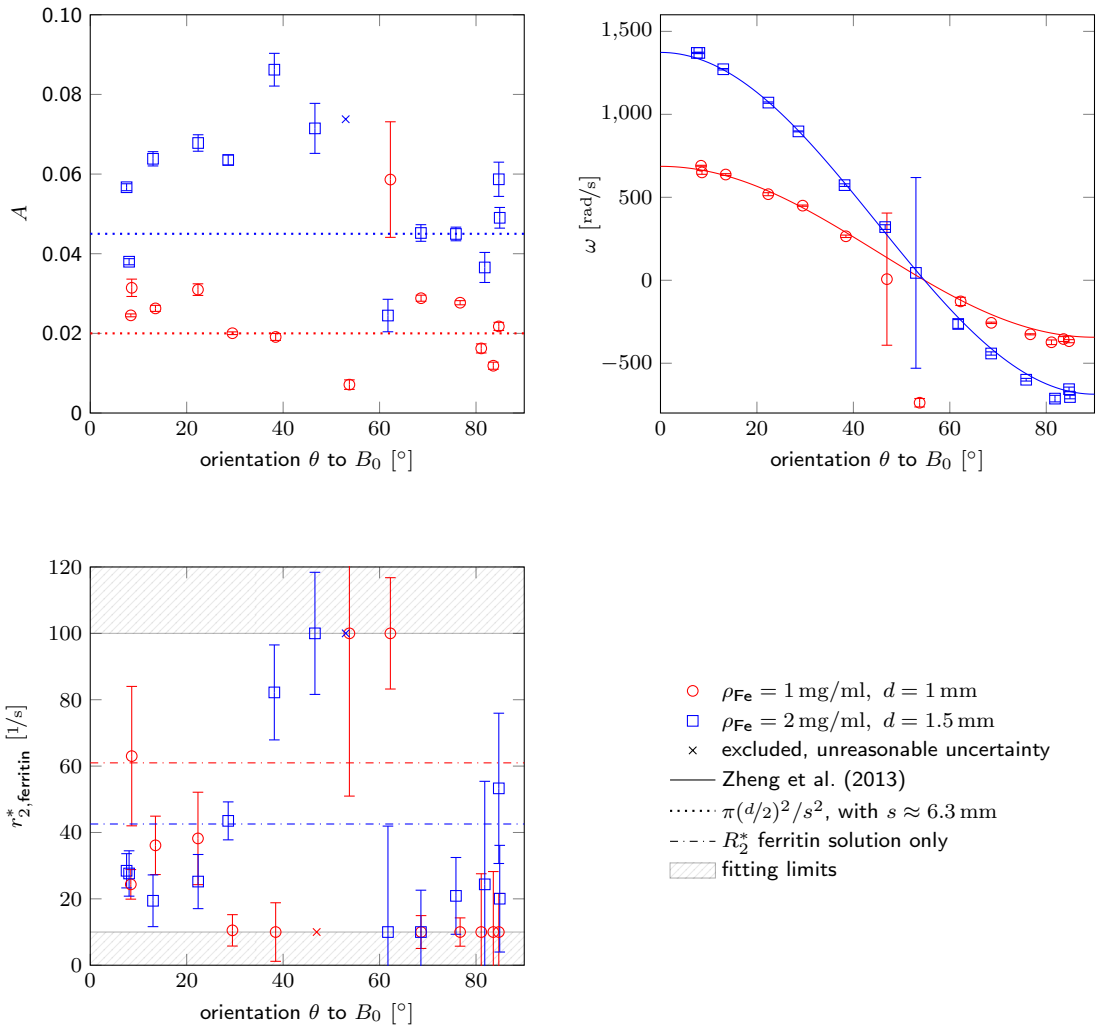


Figure 5.5.: Best fitting parameters resulting from fitting the 2-compartment model to the averaged FDM data, plotted against the capillary orientation: ferritin solution signal fraction A (top left plot), frequency offset ω between the compartments (top right plot), the difference between the relaxation rates of ferritin solution and water, $r^*_{2,\text{ferritin}}$ (bottom left plot). The dotted lines in the first plot are the volume fractions for either capillary type, f_d, calculated from the capillary diameter, d, and average capillary separation $s = 6.3\,\text{mm}$. The solid and dashed curves in the second plot show the predictions based on the orientation and susceptibility-dependent field perturbation due to an infinite cylinder. The susceptibility values were derived from the proportionality factor between the iron concentration and the susceptibility, based on experimental results from Zheng et al. (2013) (solid line).

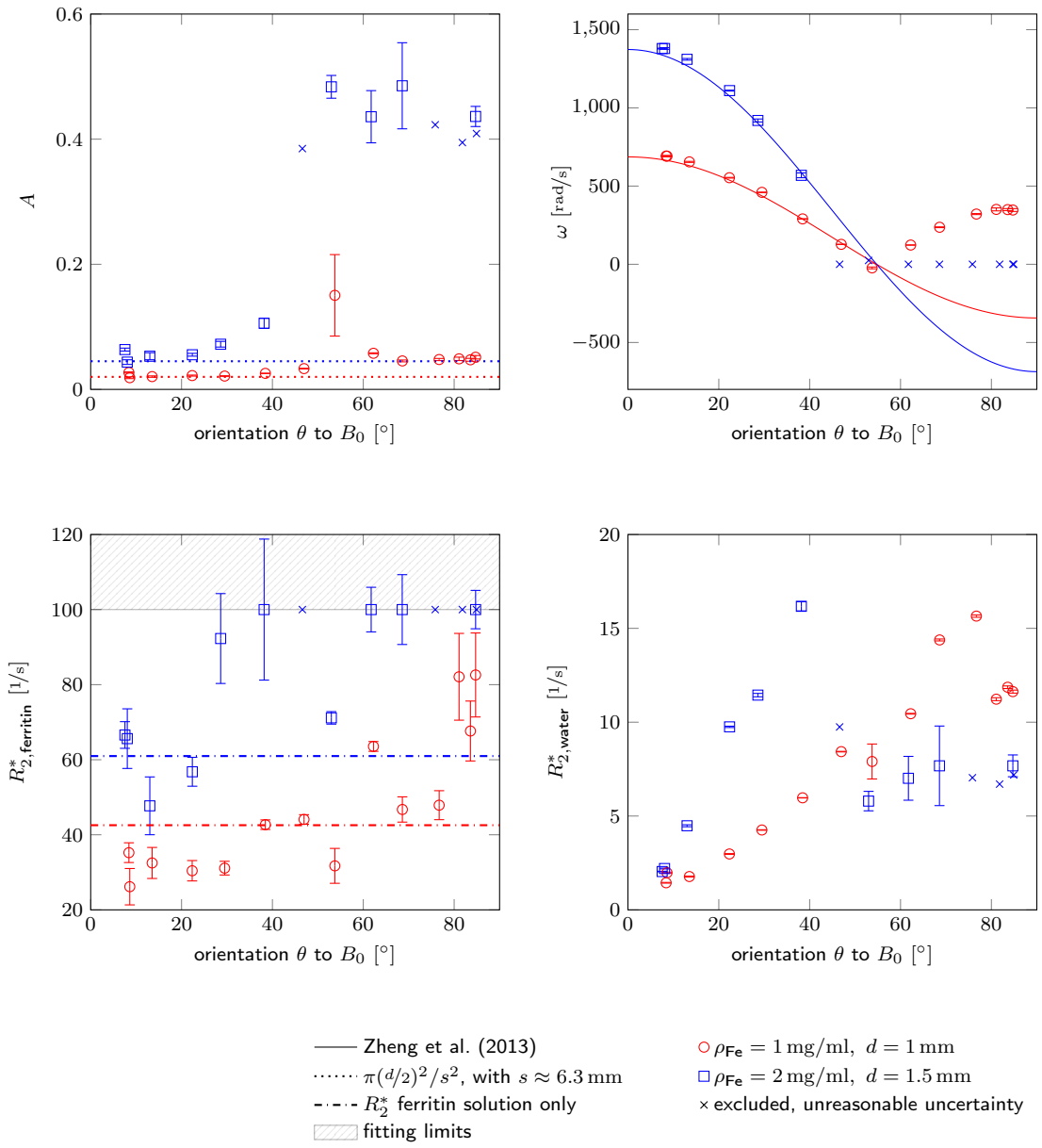


Figure 5.6.: Best fitting parameters resulting from fitting the 2-compartment model to the normalised averaged magnitude data and plotted against the capillary orientation: ferritin solution signal fraction A (top left plot), frequency offset ω between the compartments (top right plot), the relaxation rate of ferritin solution $R^*_{2,\text{ferritin}}$ (bottom left plot) and water $R^*_{2,\text{water}}$ (bottom right plot). It is evident from the frequency offsets for the lower concentration in top right, that the magnitude contains no information about their sign, i.e. negative and positive frequency offsets are indistinguishable. Moreover, the 2-compartment model fails for the solution with higher concentration of ferritin at $\theta > 40°$.

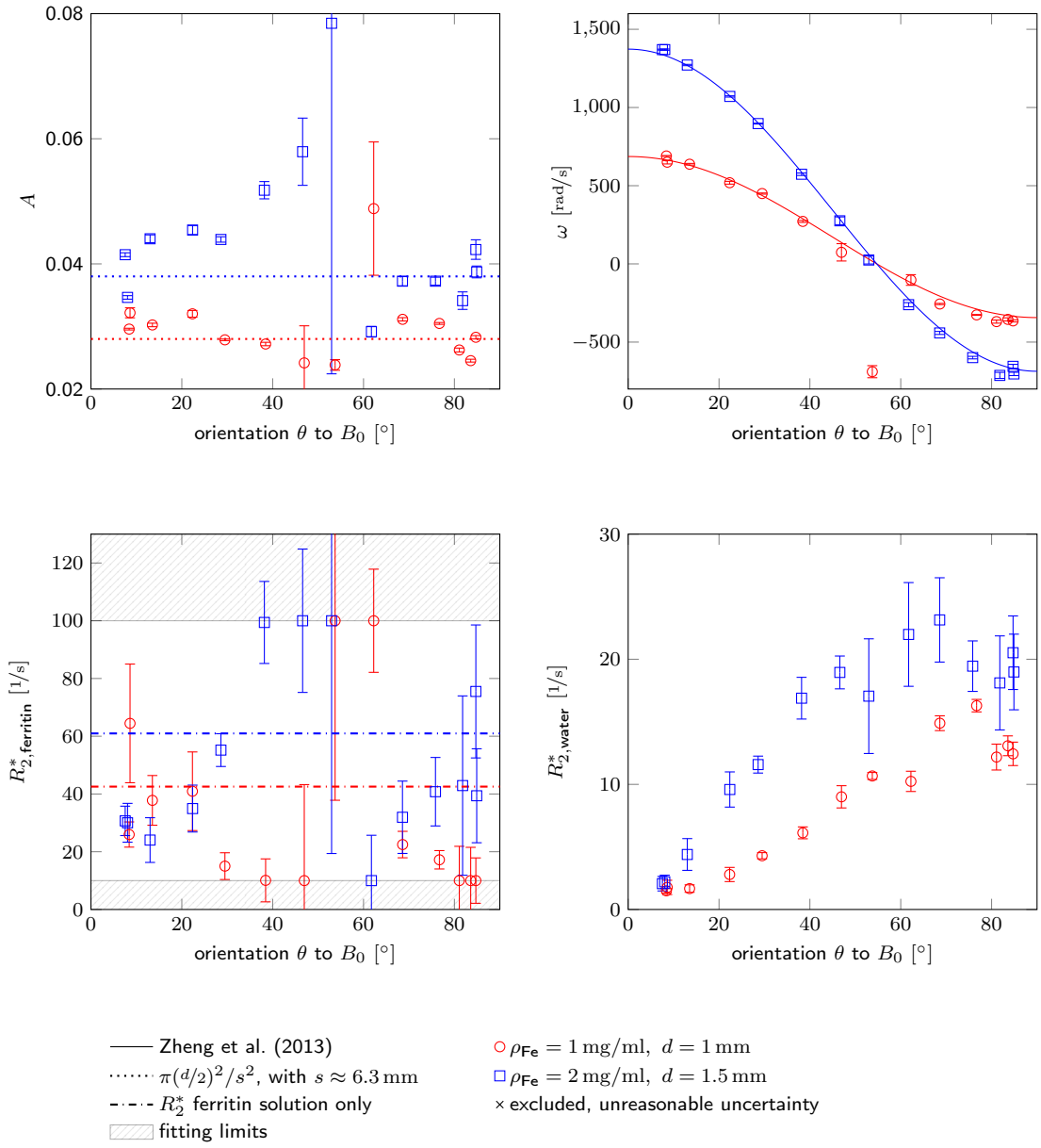


Figure 5.7.: Best fitting parameters resulting from fitting the 2-compartment model to the averaged FDM and normalised averaged magnitude data, simultaneously, and plotted against the capillary orientation: ferritin solution signal fraction A (top left plot), frequency offset ω between the compartments (top right plot), the relaxation rate of protons in ferritin solution $R^*_{2,\text{ferritin}}$ (bottom left plot) and in water $R^*_{2,\text{water}}$ (bottom right plot).

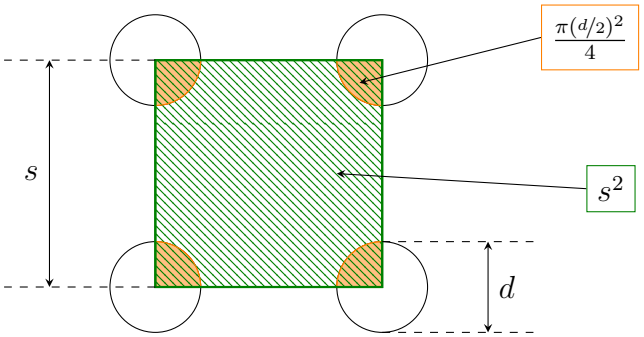


Figure 5.8.: For capillaries packed in squares capillary volume fraction can be calculated from the distance, s, between the adjacent capillaries' axes and the capillaries' diameters, d.

Ferritin signal fraction A The dotted lines in the plots with ferritin signal fractions A indicate the capillary volume fraction calculated using capillary diameter, d, and average separation between the tubes, $s = 6.3 \pm 1.5\,\mathrm{mm}$: $f_d = {}^{\pi(d/2)^2}/_{s^2}$, leading to the values $f_{d=1\,\mathrm{mm}} = 0.020 \pm 0.010$ and $f_{d=1.5\,\mathrm{mm}} = 0.045 \pm 0.021$ for diameters of $1\,\mathrm{mm}$ and $1.5\,\mathrm{mm}$. This calculation is based on the assumption that the capillary tubes are packed in squares as shown in Figure 5.8. The ferritin signal fraction obtained from the joint fit for the capillaries with diameter of $1.5\,\mathrm{mm}$ was of $\tilde{A}_{d=1.5\,\mathrm{mm}} = 0.055 \pm 0.015$ (median value), higher than that for the capillaries with diameter of $1\,\mathrm{mm}$ of $\tilde{A}_{d=1\,\mathrm{mm}} = 0.025 \pm 0.008$ (median value). Both values are higher than the estimated capillary volume fractions, f_d, of 0.045 ± 0.021 and 0.020 ± 0.010, respectively. This could be a result of some T_1-weighting due to the selected sequence parameters. Since T_1 values from the ferritin compartment are significantly shorter than T_1 values of water, the signal fraction from the ferritin solution may appear higher than its volume fraction. However, the ratio ${}^{\tilde{A}_{d=1\,\mathrm{mm}}}/_{\tilde{A}_{d=1.5\,\mathrm{mm}}} = 0.45 \pm 0.19$ is similar to the ratio of diameters' squared ${}^{(1\,\mathrm{mm})^2}/_{(1.5\,\mathrm{mm})^2} = 0.4444$. The signal fraction values reflect, therefore, the volume fraction, which depends on the diameters of the

capillaries for a similar capillary spacing, as used here. The variations in A of about 30% at different orientations probably result from the variation in the relative position between the re-aligned slice and capillaries. Larger variations occur for the θ values close to the magic angle of $54.7°$, since the frequency offset between two compartment approaches zero and the compartments can no longer be distinguished in the 2-pool model.

Relaxation rates R_2^* In the plots with relative (estimated from fitting FDM data), $r^*_{2,\text{ferritin}}$, or absolute (estimated from fitting magnitude data or joint fit), $R^*_{2,\text{ferritin}}$, relaxation rates of the ferritin solution, the dash-dotted lines indicate the actual relaxation rates as measured in Section 5.2. The shaded regions indicate the allowed fitted range of $R^*_{2,\text{ferritin}}$. Both FDM and magnitude data, show low sensitivity to the relaxation rates of ferritin. The fitted relaxation rates of water, $R^*_{2,\text{water}}$, obtained from the joint fitting of the FDM and magnitude data show a $\sin^2\theta$-like increase with the orientation, which is greater for the higher concentrated solution. This is expected due to the field inhomogeneity outside the capillary: $\Delta\omega \sim \Delta\chi \sin^2\theta$ (also see Figure 2.3).

Frequency offsets ω In the plots showing the frequency offsets, ω, the solid line is the predicted variation in ω with orientation θ and susceptibility $\Delta\chi$:

$$\omega(\theta) = \gamma B_0 \frac{\Delta\chi}{2}\left[\cos^2\theta - \frac{1}{3}\right] \ , \tag{5.4}$$

where the susceptibility values $\Delta\chi$ were estimated from the iron concentrations using the factor $p = 1.10\,{}^{\text{ppb}}/_{\mu\text{g/ml}}$ obtained experimentally by Zheng et al. (2013). The frequency offset values, ω, obtained from fitting FDM and from the joint FDM and magnitude fitting are in a very good agreement with the predicted curves, while the magnitude data are insensitive to the sign of the frequency offset.

In summary, the FDM data are highly sensitive to the susceptibility and the capillary

orientation, while the magnitude data are insensitive to the sign of ω. However, the magnitude data are more sensitive to the relaxation rates.

Voxelwise analysis In Figures 5.9, 5.10, 5.11, and 5.12 we show examples of the voxelwise FDM data fitting. In each figure we show examples of the fitted FDM data, the maps of the fitted parameters, ω, A, $r^*_{2,\text{ferritin}}$, and their uncertainties $\delta\omega$, δA, $\delta r^*_{2,\text{ferritin}}$ within each ROI. The capillary type and approximate orientation are indicated at the top right in each figure. The FDM data include two "good" (colours green and purple) and two "bad" (colours orange and teal) examples. The "good" examples usually show a good fit and fit for high partial volume fraction of the ferritin solution. The "bad" examples fit for lower ferritin volume fraction and/or show a poor fit. The colours of the plots are are equivalent to colours of the selected voxels indicated by arrows in the corresponding ROIs.

Finally, Figure 5.13 demonstrates the best-fitting values of frequency offsets mapped for each types of capillaries relative to the orientation θ.

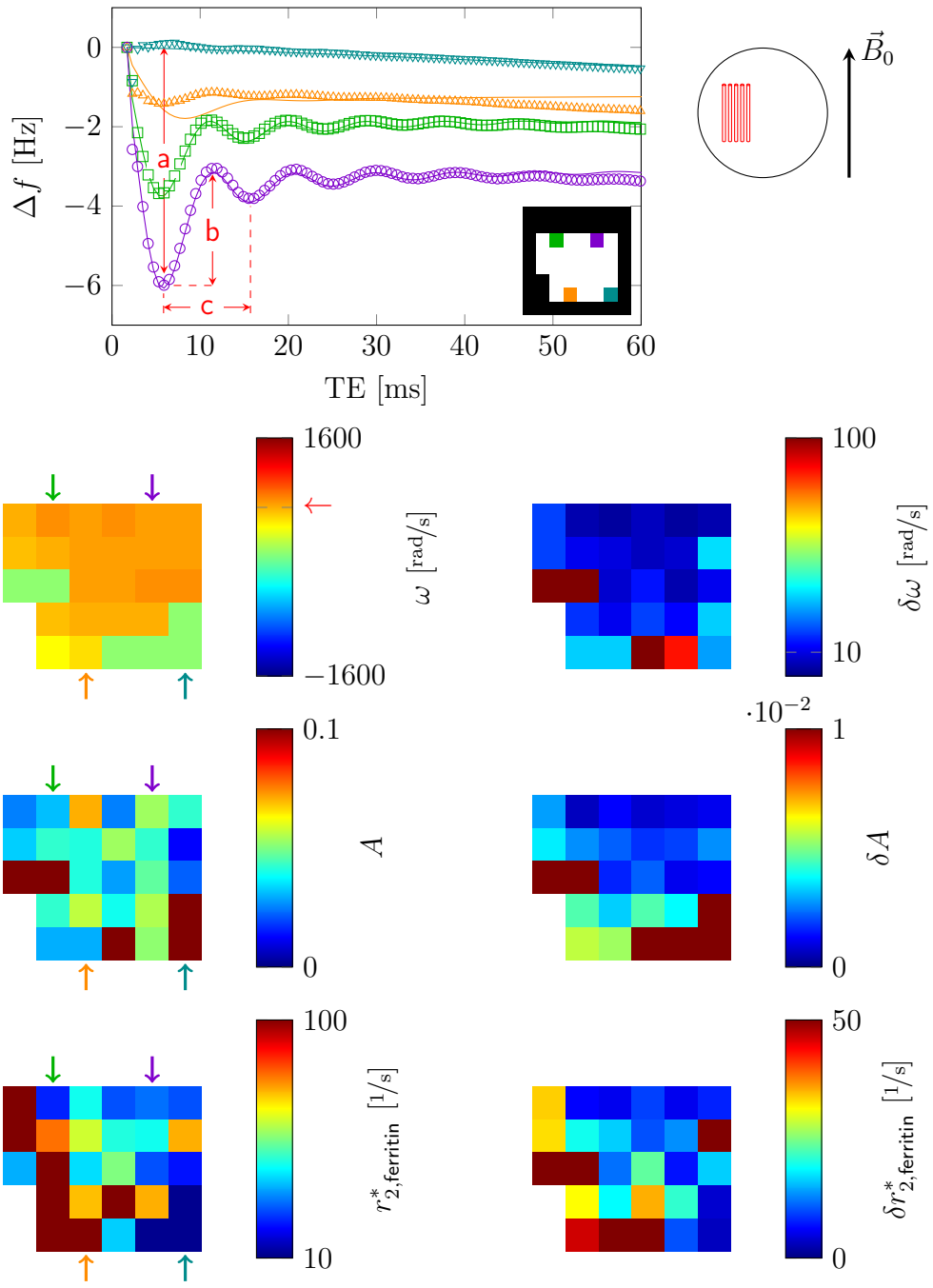


Figure 5.9.: Example of FDM data from an ROI containing the capillaries with $d = 1\,\mathrm{mm}$ and $\rho_{\mathrm{Fe}} = 1\,\mathrm{mg/ml}$, when the capillaries are approximately parallel to the magnetic field. The maps of ω, A, and $r_{2,\text{ferritin}^*}$, are given on the left), and the corresponding maps of uncertainties δ are given on the right. Red arrow in the colorbar for ω-map indicates the predicted frequency offset. The values a, b, and c indicate the maximum frequency difference, the reduction of the oscillation amplitude, and the inverse oscillation frequency, respectively.

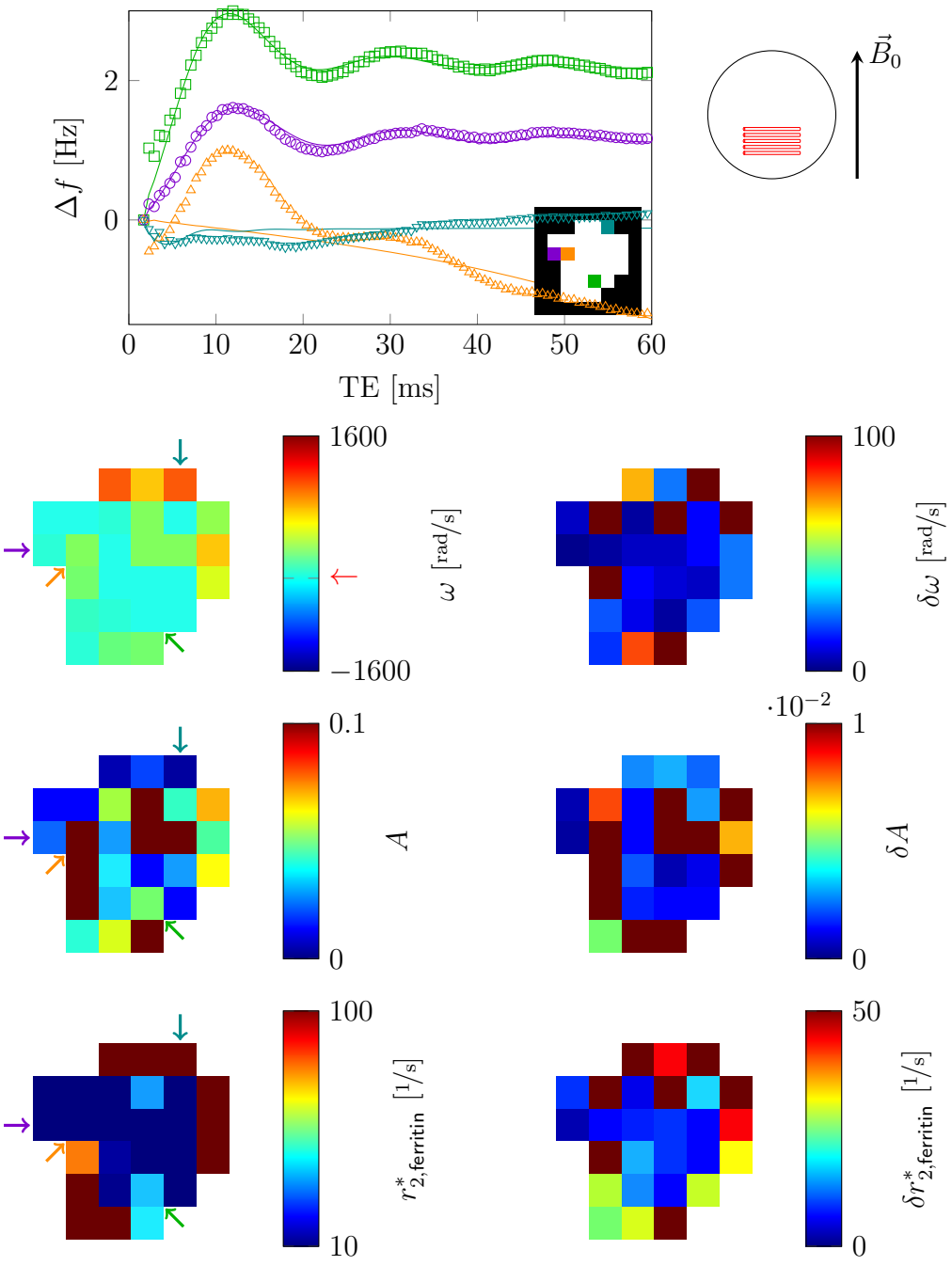


Figure 5.10.: Example of FDM data from an ROI containing the capillaries with $d = 1\,\text{mm}$ and $\rho_{\text{Fe}} = 1\,\text{mg/ml}$, when the capillaries are approximately perpendicular to the magnetic field.

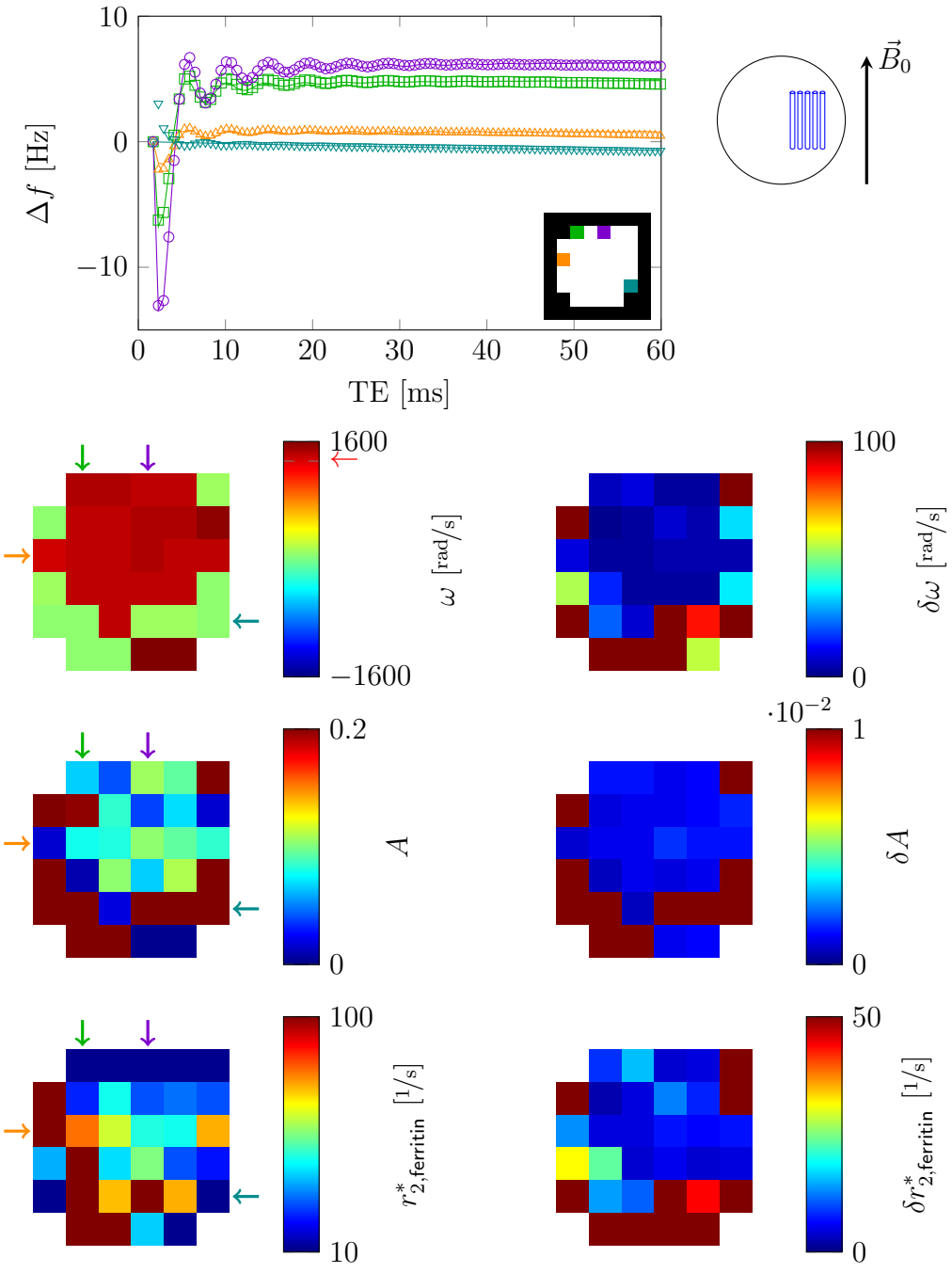


Figure 5.11.: Example of FDM data from an ROI containing the capillaries with $d = 1.5\,\text{mm}$ and $\rho_{\text{Fe}} = 2\,\text{mg/ml}$, when the capillaries are approximately parallel to the magnetic field.

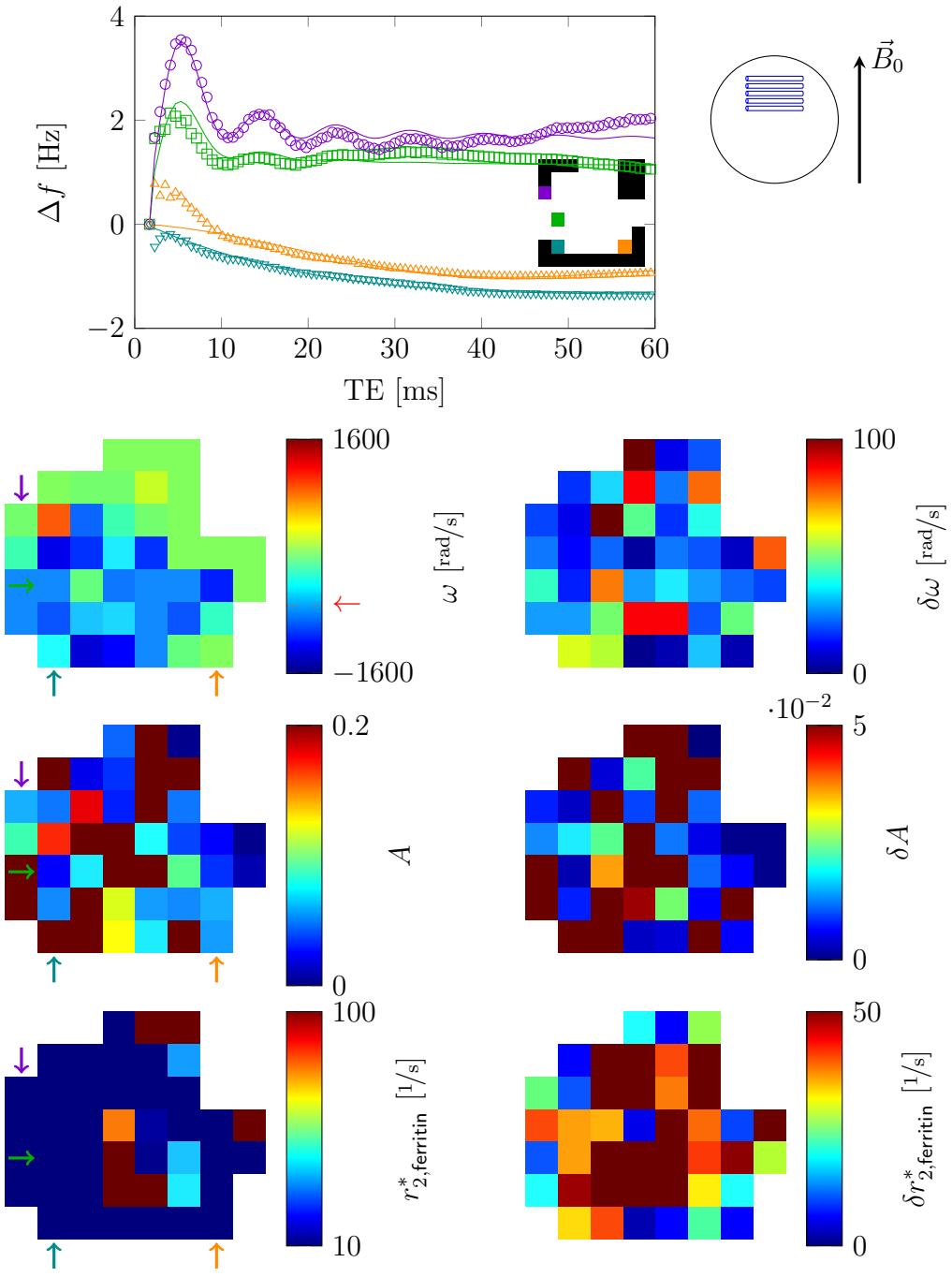


Figure 5.12.: Example of FDM data from an ROI containing the capillaries with $d = 1.5\,\text{mm}$ and $\rho_{\text{Fe}} = 2\,\text{mg/ml}$, when the capillaries are approximately perpendicular to the magnetic field.

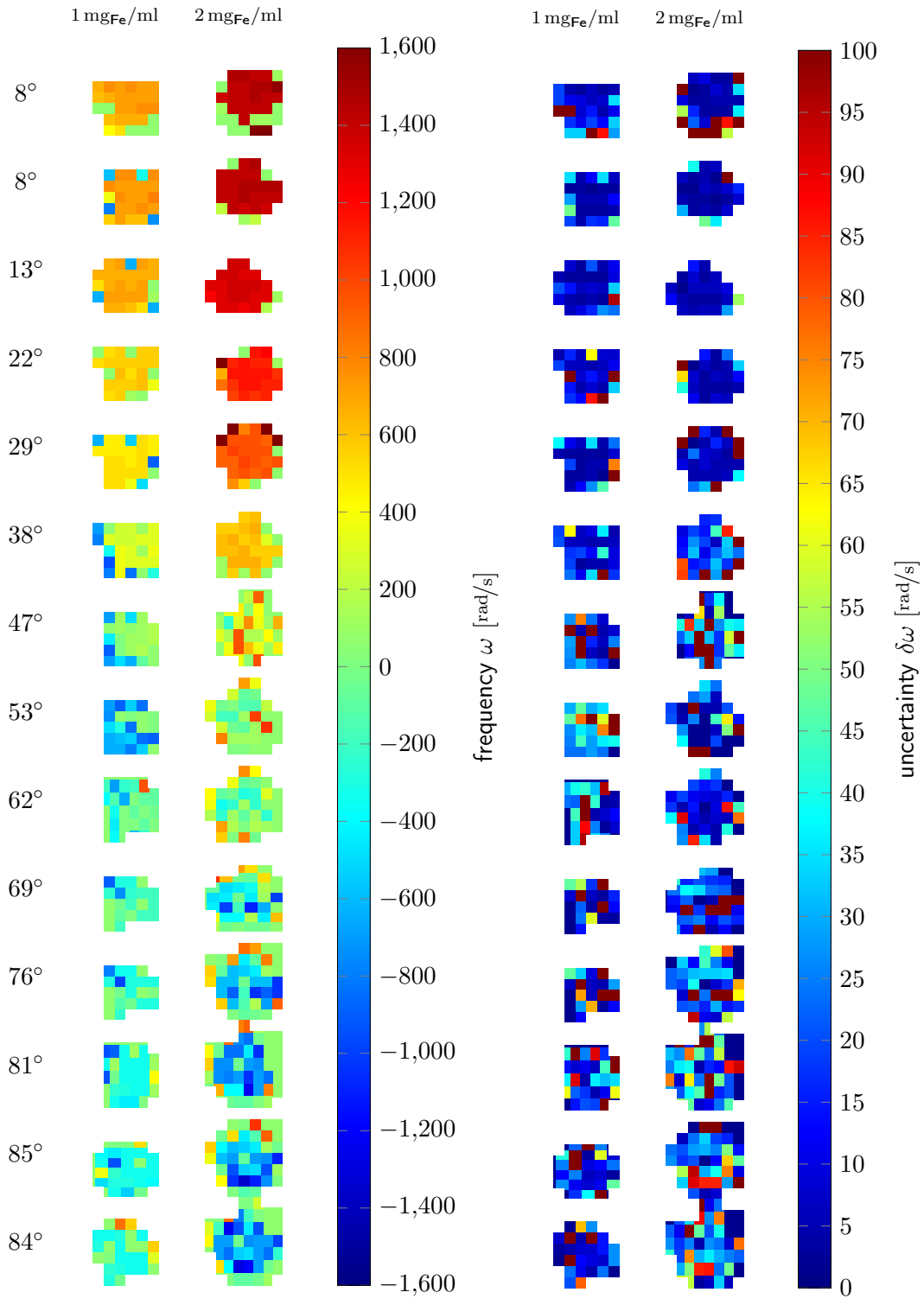


Figure 5.13.: Frequency offset, ω, varies with the capillaries' orientation with respect to the magnetic field B_0. This variation is larger with the higher iron concentration, as expected. The uncertainty, $\delta\omega$, increases when θ approaches the magic angle, $54.7°$.

5.3.3. Discussion

Values obtained from ROI averaged data There was agreement between the fitted and predicted frequency offsets for the FDM and FDM/magnitude data fits. However the magnitude data are insensitive to the sign of the frequency offset, and fails for the higher iron concentration sample at θ values above 40° with large uncertainty (blue crosses $\times$ in Figure 5.6).

In Chapter 2 we have shown that the field inhomogeneity outside the infinite cylinder varies with the angle θ and susceptibility difference $\Delta\chi$ as $\Delta\chi \sin^2\theta$ and is greatest near the cylinder walls. In our model we have assumed that the external signal decay can be approximated by a single exponential:

$$e^{-R_2 t} \cdot \int_V e^{i\delta\omega(\vec{r})t}\, \mathrm{d}\vec{r} \approx e^{-R_2 t} e^{-R_2' t} = e^{-R_2^* t} \,, \tag{5.5}$$

where $\delta\omega(\vec{r})$ is frequency deviation from the average frequency, ω_0, of the external compartment. The phantom data suggests that this approximation no longer holds when distribution of the external field inhomogeneity becomes broader, as is the case for higher susceptibility values and capillary orientations closer to perpendicular to $\vec{B}_0$, so that the 2-compartment model breaks down. The FDM data seem to be less sensitive to the relaxation rate in external compartment than the magnitude data, and hence provide better agreement with the model.

The increasing field inhomogeneity outside the cylinder is also reflected in the increasing effective transverse relaxation rate of water. The relaxation rate of the external water, $R^*_{2,\mathsf{water}}$, in the ROI containing the capillaries with lower iron concentration (red) is lower than that in the ROI containing the capillaries with higher iron concentration (blue). Moreover, we can see that $R^*_{2,\mathsf{water}}(\theta)$ follows a $\sin^2\theta$ variation in plots in

Figure 5.6 for θ below 40° when the iron concentration is $2\,\mathrm{mg/ml}$ and for θ up to 75° when the iron concentration is $1\,\mathrm{mg/ml}$. In Figure 5.7 we can see the behaviour $R^*_{2,\mathsf{water}}(\theta) \sim \sin^2\theta$ breaks down earlier for the higher iron concentration than for the lower iron concentration, at around 70° vs 75°. This correlates with the assumption that the single exponential approximation for the effective transverse relaxation holds at the lower field inhomogeneities.

The estimated values for ferritin signal fractions, A, are similar for all data types, except for when the data fitting failed in the magnitude data (as indicated by the symbol $\times$ in Figure 5.6). Small variations with θ are likely to be linked to the low number of the capillaries and the varying slice position relative to the capillaries, since the slice was realigned after each rotation. Signal fraction is proportional to the volume fraction of the capillaries. This is evident from the similarity of the ratio between the squared diameters to the ratio between the signal fractions of the corresponding capillaries, which we obtained from the joint data analysis.

Compared to other parameters, the estimation of the effective transverse rate of relaxation of the ferritin solutions, $R^*_{2,\mathsf{ferritin}}$, or their relaxation rate relative to that of water in the case of FDM, $r^*_{2,\mathsf{ferritin}}$, appears to be very inaccurate and approaches the fitting boundaries. It was assumed that the measured values for $R^*_{2,\mathsf{ferritin}}$ would be independent of the orientation of the capillaries, whereas the values for $r^*_{2,\mathsf{ferritin}}(\theta)$ decreased with $-\sin^2\theta$ because of the increasing relaxation rate of water $R^*_{2,\mathsf{water}}(\theta)$. Based on the obtained relaxation rates of each solution, we also expected that the signal of the ferritin solution in the tubes with higher iron concentration would show faster decay. One of the possible causes of the inaccurate estimation of this value lies in the higher influence of frequency offset, ω, and signal fraction, A, values on the data: the rate of relaxation from a small compartment has only small impact on the signal

amplitude or the frequency difference, compared to other parameters, therefore it has a smaller contribution to the residual norm. More accurate modelling may improve the estimation of the parameters. Since the frequency offset values were estimated very accurately, they can be fixed in the fit once they are known, and this may improve the estimation of R_2^*-values.

FDM time evolution We plotted the FDM data examples for both capillary types from the data acquired at two extreme orientations in Figures 5.9, 5.10, 5.11, and 5.12 The maximum frequency difference (a in Figure 5.9) reflects the signal fraction of the ferritin compartment and the frequency offset between the internal and external compartments. For example, the maximum frequency difference of the green FDM curve in Figure 5.9 is lower than that of the purple curve, correspond to the measured signal fractions of the ferritin solutions are 0.0303 ± 0.0005 and 0.0499 ± 0.0007, respectively. Thus the increase in signal fraction, A, is reflected in the higher frequency difference (a in Figure 5.9), as long as the frequency offsets, ω, between the compartments are similar.

The rate at which the amplitude (b in Figure 5.9) of the FDM oscillation reduces reflects the difference in the rate of relaxation in the two compartments. The frequency of the FDM oscillations (the inverse of c in Figure 5.9) is related to the frequency offset, ω, between the compartments. For example, comparing the purple curves in Figures 5.9 and 5.11; in the first case, there are approximately two oscillations in the first $20\,\mathrm{ms}$, while in the second case there are approximately four oscillations in the same period of time. Consequently, we can estimate the approximate values of frequency offsets from the plots as: $\sim 630\,^{\mathrm{rad}}/_{\mathrm{s}}$ and $\sim 1260\,^{\mathrm{rad}}/_{\mathrm{s}}$. The corresponding values for the frequency offsets obtained from the fit are: $\omega = 685 \pm 3\,^{\mathrm{rad}}/_{\mathrm{s}}$ and $\omega = 1377 \pm 2\,^{\mathrm{rad}}/_{\mathrm{s}}$, respectively.

The approximate values are less than $10\,\%$ less than the best-fitting values for ω.

The identification of the sign of the frequency offset from FDM is not always trivial, since it depends on the relationship between the echo spacing and the increase of the frequency offset between the compartments. For lower frequency offset and short echo spacing, the sign of the frequency offset is opposite to the sign of the FDM, as evident in the examples in Figure 5.9 and Figure 5.10 where the iron concentration is $\rho_{\mathsf{Fe}} = 1\,\mathrm{mg/ml}$. For example the purple FDM data in Figure 5.9 shows *negative* frequency difference and the best fitting value for the frequency offset is $\omega = 685 \pm 3\,{}^{\mathrm{rad}}/_{\mathrm{s}}$, i.e. *positive*. The purple FDM data in Figure 5.10 shows *positive* frequency difference, while the frequency offset is estimated to be $\omega = -343 \pm 2\,{}^{\mathrm{rad}}/_{\mathrm{s}}$, i.e. *negative*. However, when $\omega\Delta\mathrm{TE} \gtrsim 1$, interpreting the character of FDM becomes non-trivial, as, for example, in case of the FDM data shown in Figure 5.11. The frequency offset estimated from the purple curve is $\omega = 1377 \pm 2\,{}^{\mathrm{rad}}/_{\mathrm{s}}$, therefore ${}^{1}/_{\omega} = 0.7\,\mathrm{ms}$ which is similar to the echo spacing $\Delta\mathrm{TE} = 0.6\,\mathrm{ms}$. The relative relaxation rate between the compartments may additionally have an influence on the FDM behaviour in this case.

Translation into in-vivo Despite the greater complexity of in-vivo data, this phantom study gives us some pointers that are important for an *in vivo* set-up. First of all, we have seen that phase data processed using FDM analysis allows accurate estimation of the frequency offset, ω, between two compartments, which is evident from the corresponding plots in Figure 5.7 and ω maps in Figure 5.13. In contrast, the magnitude data are insensitive to the sign of ω and, therefore, to the orientation. This approach is very different to the majority of studies which investigate venous blood oxygenation using phase effects, since it does not require high spatial resolution. The susceptibility of venous blood is approximately $1\,\mathrm{ppm}$ (or less), which is comparable to the sus-

ceptibility value of the ferritin solution with an iron concentration of $\rho_{\mathsf{Fe}} = 1\,\mathrm{mg/ml}$. This means, that we can assume, that the decay of the signal from the external compartment can be approximated as a single exponential. The relaxation rate of the intra-vascular compartment *in vivo* is higher than that of our ferritin solutions. This and the similar susceptibility values indicate the need for a good temporal resolution at short echo times. Therefore the bipolar readout will be more appropriate in this situation than the unipolar, since it allows us to achieve shorter echo spacing.

Obviously, the in-vivo situation is far more complex than the phantom: (i) the external compartment may be far more complex due to local iron deposits and CSF contributions; (ii) multiple vessels with different orientations may be present in the same voxel; (iii) and last but not least, (physiological) motion may contribute to the phase information.

5.4. Conclusion

The IronPhan phantom helped us to better understand the complex signal evolution in presence of two compartments. We saw that the susceptibility values can be accurately obtained from the frequency offsets between two compartments for the known capillaries' orientation at the microscopic level. We have demonstrated the sensitivity to the capillary orientation of the FDM data, in contrast to the magnitude data.

Blood oxygenation level is an important bio-marker for understanding the brain physiology and disorders, which is reflected in the susceptibility value of venous blood. Our method can be therefore be applied at microscopic level to investigate the oxygen saturation of venous blood, but also to investigate the cerebral microvasculature.

6. Probing the myelin water compartment with a saturation recovery MEGE sequence

6.1. Introduction

We have demonstrated in Chapter 2 in Section 2.3 that the signal decay in myelinated white matter tissue acquired using multi-echo gradient-echo sequence is non-mono-exponential. Recent publications suggest there is a component of the magnetisation in white matter with short T_1 ($\ll 1\,\mathrm{s}$), which has been associated with the myelin water pool, Labadie et al. (2014); Kim et al. (2015); van Gelderen et al. (2016).

In this chapter we investigate the influence of the saturation recovery multi-echo gradient-echo sequence on the signal evolution from the human corpus callosum. We acquired MEGE scans with fixed short repetition time and variable excitation angles and evaluated the decay of the signal magnitude and evolution of the frequency difference with echo time. Our hypothesis is that the short T_2^* and short T_1 of myelin water (MW) will be reflected in lesser saturation of the MW pool relative to the axonal and external water pools in the saturation recovery, which will in turn be manifested as an

increased frequency difference and rate of magnitude signal decay with increasing flip angle.

6.2. Materials and methods

Data acquisition Mid-sagittal, single-slice, RF- and gradient-spoiled multi-echo gradient-echo data were acquired from five healthy subjects ($24.2 \pm 0.7\,\mathrm{y}$, 3 female). The in-plane resolution was $1 \times 1\,\mathrm{mm}^2$ and the slice thickness was $5\,\mathrm{mm}$. Each protocol involved acquisition of 60 MEGE scans: acquired for 6 different excitation angles, repeated with the polarity of the bipolar read gradients being reversed, and all repeated 5 times. To achieve different excitation angles, the B_1 amplitude of the RF pulses was varied while maintaining a fixed pulse length. The maximum B_1 amplitude and the pulse duration were defined by the shortest possible RF excitation pulse that could be used to achieve $80°$ flip angle on the scanner, and the RF pulse amplitudes were scaled by $[1.00\ 0.75\ 0.60\ 0.45\ 0.30\ 0.10]$ to produce nominal flip angles of $[80°\ 60°\ 48°\ 36°\ 24°\ 8°]$. B_1 amplitude modulation was adopted over varying the pulse duration because it allowed us to avoid variation of eddy current effects due to variable slice selective gradients in the latter case. Thirty echoes were acquired for each excitation and the values of the first echo time, echo spacing, and repetition time were set to $\mathrm{TE}_1/\Delta\mathrm{TE}/\mathrm{TR} = 1.52/1.4/100\,\mathrm{ms}$. Magnitude, phase, real and imaginary data were saved for images acquired at each echo time. The complex data were averaged over 5 repeats. Examples of phase variation as a function of the dynamic scan are shown in Figure 6.1 and Figure 6.2.

B_1 maps were acquired using dual-TR $3\mathrm{D}$ gradient-echo sequence to determine the true values for the excitation angles in the region of interest. The values for flip angle, echo time, and first and second repetition times were $\alpha/\mathrm{TE}/\mathrm{TR}_1/\mathrm{TR}_2 =$

$60°/5\,\mathrm{ms}/23\,\mathrm{ms}/80\,\mathrm{ms}$, and voxel size was $3 \times 3 \times 5\,\mathrm{mm}^3$.

In order to correct for residual eddy-current-related field variation, MEGE data from a spherical phantom (outer diameter of $16\,\mathrm{cm}$) containing aqueous copper sulphate solution were acquired for the same slice position and orientation as for the data acquired from each subject, using the same scanning parameters.

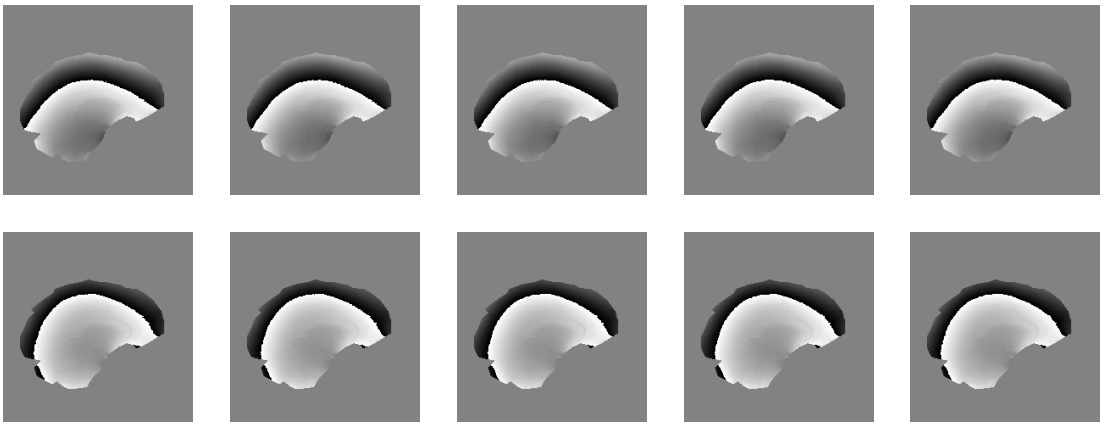
Signal processing Each real and imaginary data set of the *in vivo* and the phantom data were averaged across dynamic scans for each echo and combined to provide the complex signal evolution:

$$S_n^{\pm} = S^{\pm}(\mathrm{TE}_n) = \overline{\mathfrak{R}(S^{\pm}_{\mathsf{dynamic}}(\mathrm{TE}_n))} + i \cdot \overline{\mathfrak{I}(S^{\pm}_{\mathsf{dynamic}}(\mathrm{TE}_n))}\ . \tag{6.1}$$

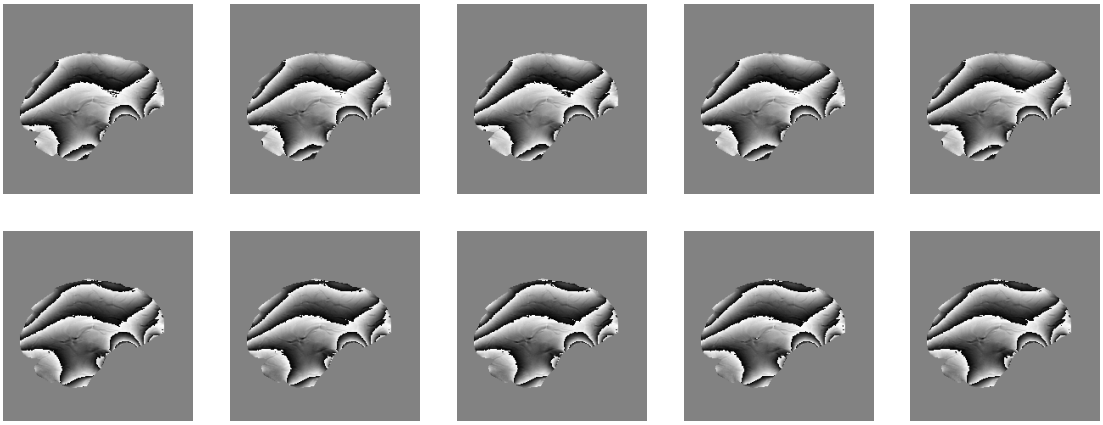
The superscript $\pm$ indicates the polarity of the first read gradient, subscript 'dynamic' indicates the signal from each dynamic scan, $\mathfrak{R}$ and $\mathfrak{I}$ are the real and the imaginary part of the signals, TE_n is the echo time of the nth gradient-echo, and the overlines indicate the arithmetic mean over the dynamic scans.

The product of the complex signals S_n^+ and S_n^- for each RF excitation amplitude was processed using FDM following equation (3.10). The 3rd order polynomial fits were estimated for each echo from the FDM phantom data and were subtracted from the corresponding in-vivo FDM data to correct for eddy current effects. Examples of magnitude, FDM and eddy-current-corrected FDM images from the lowest and the highest excitation pulses collected at the echo time of $14\,\mathrm{ms}$ are shown in Figure 6.3. Figure 6.4a shows the FDM data and Figure 6.4b shows the magnitude data as a function of the RF amplitude acquired at $\mathrm{TE} = 14\,\mathrm{ms}$. Figure 6.5a and Figure 6.5b show example of FDM and magnitude data at low and high flip angle, respectively.

Finally, for each subject a ROI in the splenium of the corpus callosum was selected. The

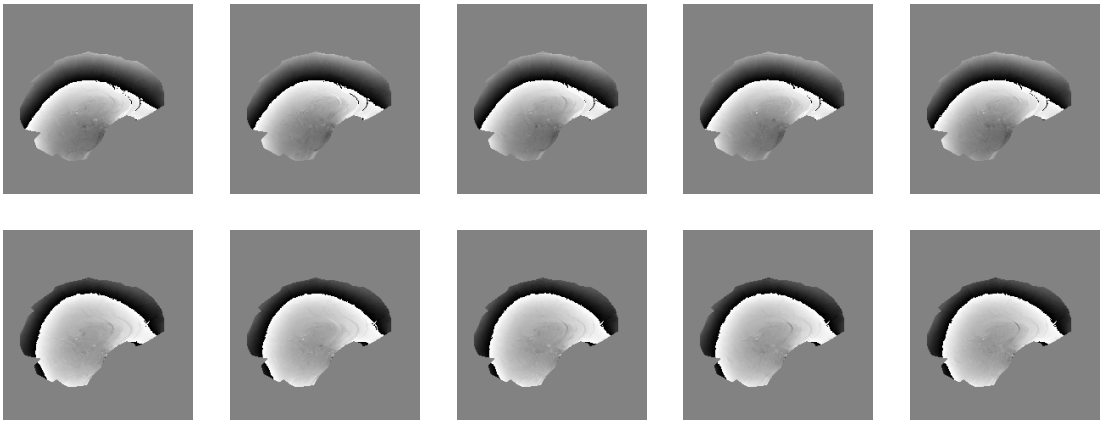


(a) Phase variation as a function of the dynamic scan (left to right) from the data acquired at $\mathrm{TE} = 1.5\,\mathrm{ms}$ (odd echo number) and lowest flip angle with fat shift direction foot (top row) and head (bottom row).

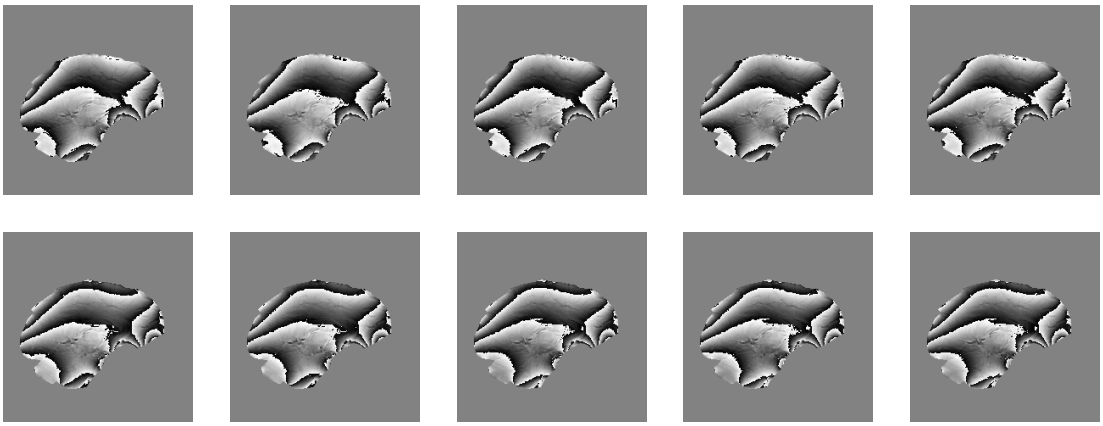


(b) Phase variation as a function of the dynamic scan (left to right) from the data acquired at $\mathrm{TE} = 14\,\mathrm{ms}$ (even echo number) and lowest flip angle with fat shift direction foot (top row) and head (bottom row).

Figure 6.1.: Example for the phase data as a function of dynamics (left to right) acquired using the lowest flip angle at (a) $\mathrm{TE} = 1.5\,\mathrm{ms}$ and (b) $\mathrm{TE} = 14\,\mathrm{ms}$. There is no evident phase variation between the dynamic scans.



(a) Phase variation as a function of the dynamic scan (left to right) from the data acquired at $\mathrm{TE} = 1.5\,\mathrm{ms}$ (odd echo number) and highest flip angle with fat shift direction foot (top row) and head (bottom row).



(b) Phase variation as a function of the dynamic scan (left to right) from the data acquired at $\mathrm{TE} = 14\,\mathrm{ms}$ (even echo number) and highest flip angle with fat shift direction foot (top row) and head (bottom row).

Figure 6.2.: Example for the phase data as a function of dynamics (left to right) acquired using the highest flip angle at (a) $\mathrm{TE} = 1.5\,\mathrm{ms}$ and (b) $\mathrm{TE} = 14\,\mathrm{ms}$. There is no evident phase variation between the dynamic scans.

corpus callosum is a bundle of white matter fibres, which connects two hemispheres of the brain and thus appears to be perpendicular to $\vec{B}_0$ of the scanner. As a result, the frequency offset between the external, intra-axonal and myelin water pools is maximal, see Section 2.3. The splenium of the corpus callosum is less susceptible to the in-flow artifacts from the anterior cerebral artery than the genu and body of the corpus callosum. The mean of the FDM and magnitude data were calculated for each echo in each data set within the selected ROI. The mean magnitude data were normalised by the mean magnitude of the first echo.

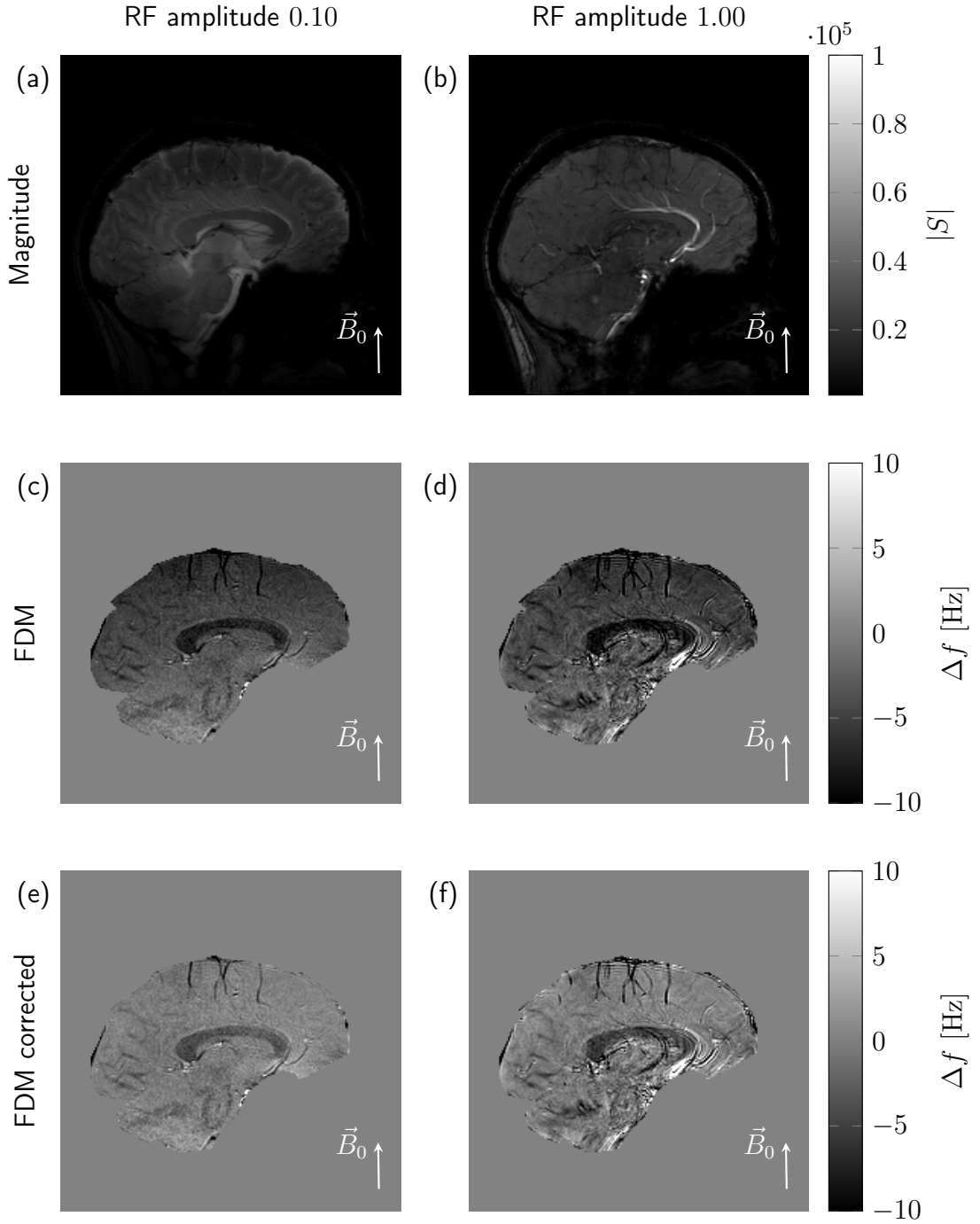


Figure 6.3.: Magnitude (a) and (b), FDM (c) and (d), and FDM corrected for eddy current (e) and (f) data examples acquired at echo time of $14\,\mathrm{ms}$. Data in (a), (c) and (e) were acquired at $10\,\%$ of the maximum B_1 amplitude, and data in (b), (d) and (f) were acquired at the maximum B_1 amplitude. Here, the maximum B_1 amplitude is associated with the amplitude of the shortest, $80°$ flip angle RF pulse.

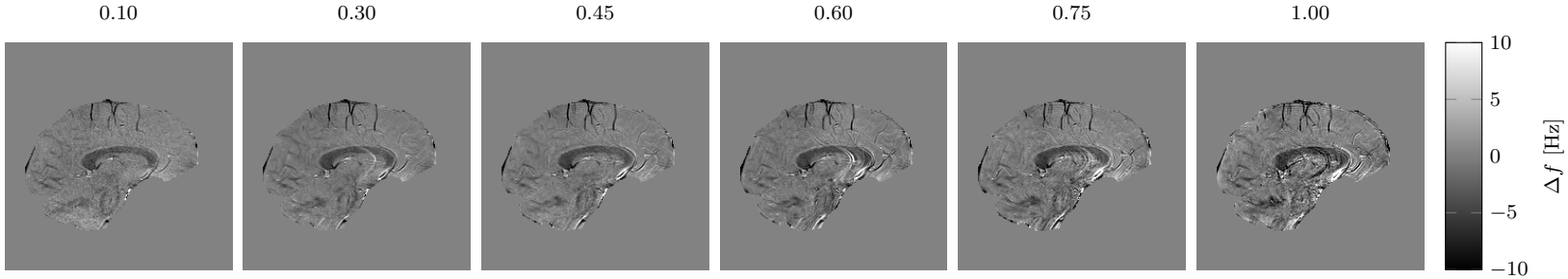


Figure 6.4a.: Example of the FDM data variation with the RF amplitude acquired at $\mathrm{TE} = 14\,\mathrm{ms}$.

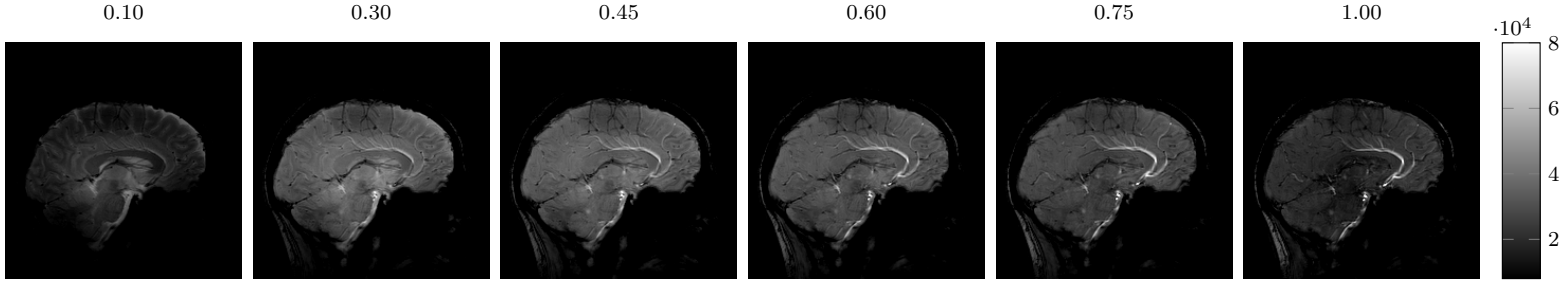


Figure 6.4b.: Example of the magnitude data variation with the RF amplitude acquired at $\mathrm{TE} = 14\,\mathrm{ms}$.

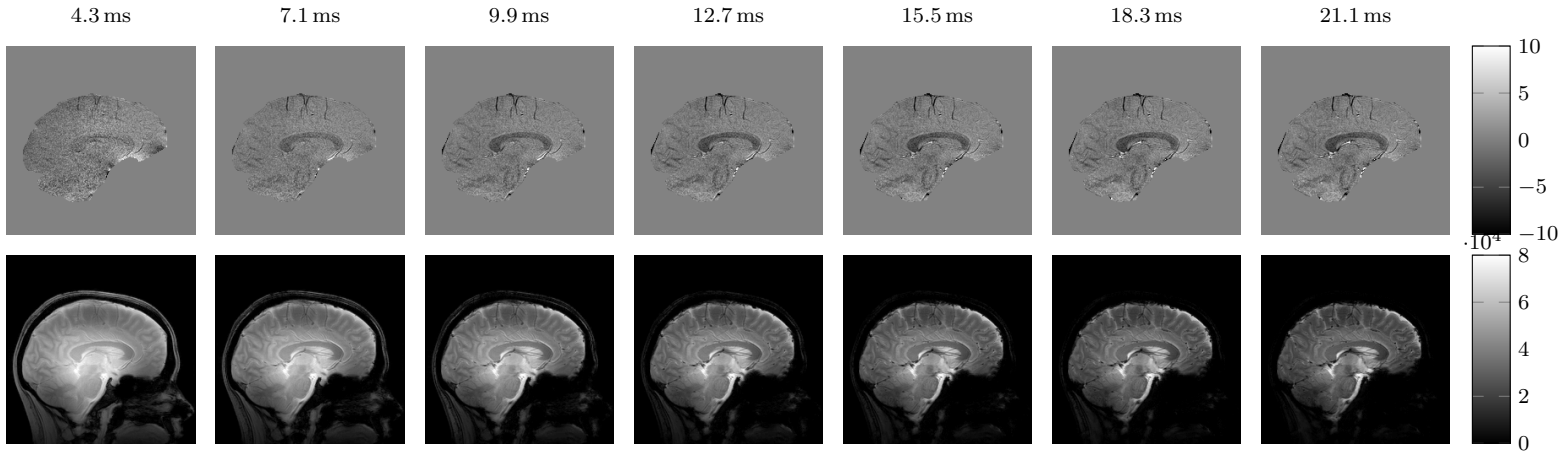


Figure 6.5a.: Example of the FDM and magnitude data evolution with TE acquired at RF amplitude scale of 0.10.

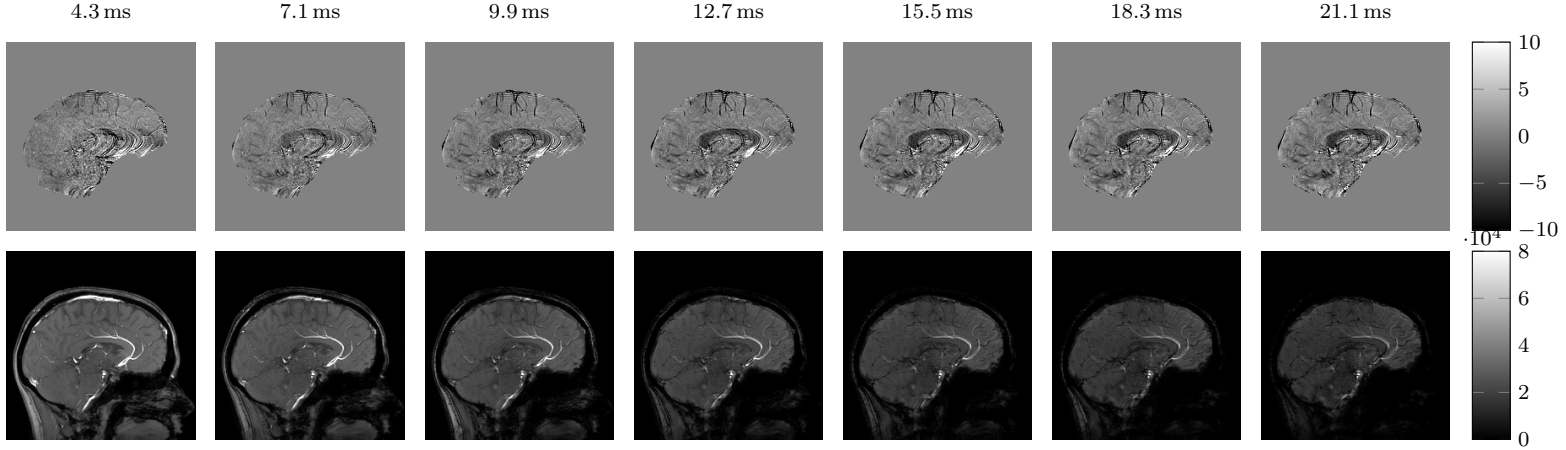


Figure 6.5b.: Example of the FDM and magnitude data evolution with TE acquired at RF amplitude scale of 1.00.

Signal evolution modelling As described in Chapter 2 in Section 2.3, white matter signal can be described by 3-pool model, where the signal evolution of each of the water pools is given by $F_{\mathrm{e/a/m}}(t) \sim A_{\mathrm{e/a/m}} \cdot e^{i\omega_{\mathrm{e/a/m}}t} \cdot e^{-R^*_{\mathrm{e/a/m}}t}$ (van Gelderen et al. (2012); Nam et al. (2015)). The subscript e/a/m indicates the external (e), axonal (a) or myelin (m) water pools, A is the signal fraction of each water pool, ω denotes frequency offset relative to a reference frequency, and R_2^* is the effective transverse relaxation rate. The signal fraction A carries the information on volume fraction V and proton density ρ, but will also depend on a longitudinal relaxation rate dependent factor L, linked to the saturation recovery. While the volume and proton density are independent of the scanning parameters, the factor L, at the fixed repetition time, will vary with the RF excitation amplitude, which defines the excitation angle α:

$$L_{\mathrm{e/a/m}}(\alpha) = \sin\alpha \cdot \frac{1 - e^{-\mathrm{TR}/T_{1,\mathrm{e/a/m}}}}{1 - \cos\alpha \cdot e^{-\mathrm{TR}/T_{1,\mathrm{e/a/m}}}} \ . \tag{6.2}$$

Moreover, when observing the complex signal of white matter, we can only distinguish the relative signal fractions, e.g. ${}^{A_\mathrm{e}}/_{A_\mathrm{a}}$ and ${}^{A_\mathrm{m}}/_{A_\mathrm{a}}$, not the absolute signal fraction values. Here, the initial assumption will be that the longitudinal relaxation times of axonal and external water pools are similar and much larger than the repetition time: $T_{1,\mathrm{e}} \approx T_{1,\mathrm{a}} \gg \mathrm{TR}$, so that the dependence of relative signal fraction ${}^{A_\mathrm{e}}/_{A_\mathrm{a}}$ on the RF excitation can be ignored. By setting the reference frequency equal to the Larmor frequency of the external water pool, we can set the frequency offset ω_e to zero. Based on the findings in previous studies, we also assume similar effective transverse relaxation rates of axonal and external pools, i.e. $R^*_{2,\mathrm{a}} \approx R^*_{2,\mathrm{e}} = R^*_2$. The 3-pool model is illustrated in Figure 6.6

In the following steps we describe modifications of the 3-pool model: (i) for fitting FDM data, and (ii), (iii), and (iv) for joint fitting of FDM and magnitude data. In (i),

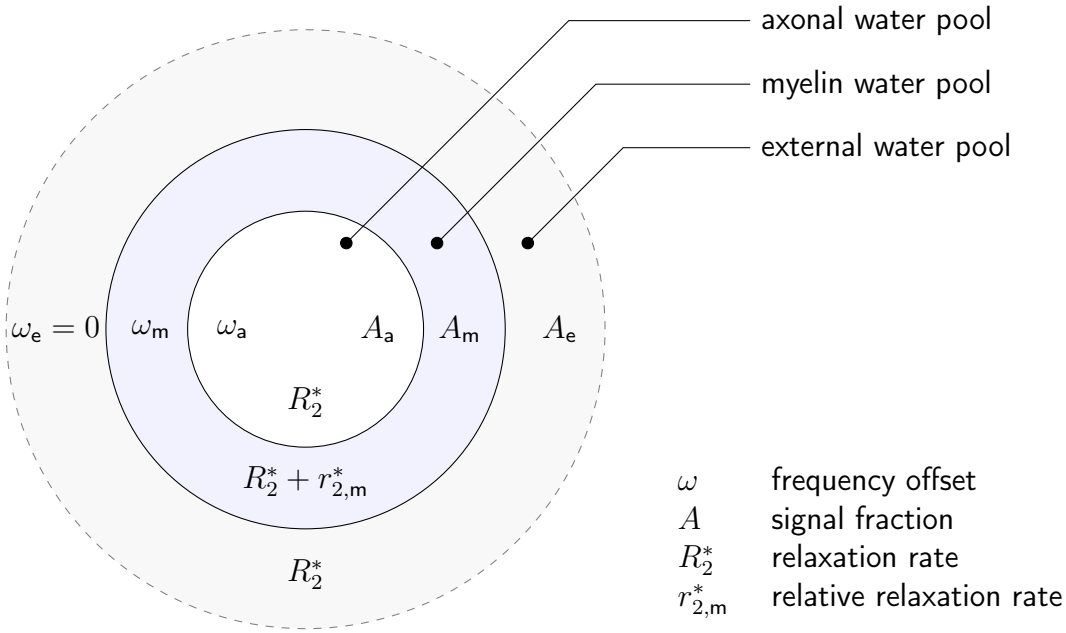


Figure 6.6.: Schematic description of the 3-pool model for describing the multi-exponential multi-echo gradient-echo signal evolution from the white matter oriented perpendicular to $\vec{B}_0$.

(ii), and (iii) we assume $T_{1,a} = T_{1,e}$ and in (iv) $T_{1,a} \neq T_{1,e}$.

(i) First, we modelled the signal evolution in the FDM data. This it is insensitive to the absolute value of the effective relaxation rate R_2^*, so that the FDM signal evolution can be reduced to 4 RF-excitation-independent parameters: ω_a, ω_m, $r_{2,m}^* = R_{2,m}^* - R_2^*$ (the difference in the transverse relaxation rate of myelin water), and ${}^{A_e}/_{A_a}$; and 6 RF-dependent parameters ${}^{A_m}/_{A_a}(\alpha)$, which vary with the excitation pulse amplitude – fitting 6×29 data points to 10 parameters:

$$S(t, \alpha) \sim \frac{A_e}{A_a} + e^{i\omega_a t} + \frac{A_m}{A_a}(\alpha) \cdot e^{i\omega_m t} \cdot e^{-r_{2,m} t} \ . \tag{6.3}$$

(ii) In the next step we introduce the joint modelling of FDM and magnitude evolution and therefore include the absolute value of the effective relaxation rate R_2^*, increasing

the number of parameters to 11 and number of data points to 6×59, where FDM and magnitude data contribute 6×29 and 6×30 data points, respectively:

$$S(t,\alpha) \sim \left(\frac{A_{\mathsf{e}}}{A_{\mathsf{a}}} + e^{i\omega_{\mathsf{a}} t} + \frac{A_{\mathsf{m}}}{A_{\mathsf{a}}}(\alpha) \cdot e^{i\omega_{\mathsf{m}} t} e^{-r^*_{2,\mathsf{m}} t} \right) \cdot e^{-R^*_2 t} \ . \tag{6.4}$$

(iii) The spatially linear macroscopic magnetic field inhomogeneity through the slice G_x effects the magnitude of the signal as echo-time-dependent factor $\mathrm{sinc}(a \cdot t)$, where a depends on the gradient amplitude and slice thickness, Yablonskiy (1998). Here we thus fit for 12 parameters and 6×59 data points:

$$S(t,\alpha) \sim \left(\frac{A_{\mathsf{e}}}{A_{\mathsf{a}}} + e^{i\omega_{\mathsf{a}} t} + \frac{A_{\mathsf{m}}}{A_{\mathsf{a}}}(\alpha) \cdot e^{i\omega_{\mathsf{m}} t} e^{-r^*_{2,\mathsf{m}} t} \right) \cdot e^{-R^*_2 t} \cdot \mathrm{sinc}(a \cdot t) \ . \tag{6.5}$$

(iv) Finally, we also allow for the relative signal fraction ${}^{A_{\mathsf{e}}}\!/_{A_{\mathsf{a}}}$ to vary with the excitation angle, replacing one fixed fitting parameter ${}^{A_{\mathsf{e}}}\!/_{A_{\mathsf{a}}}$ by six excitation-angle-dependent fitting parameters ${}^{A_{\mathsf{e}}}\!/_{A_{\mathsf{a}}}(\alpha)$ yielding a total of 17 parameters and 6×59 data points:

$$S(t,\alpha) \sim \left(\frac{A_{\mathsf{e}}}{A_{\mathsf{a}}}(\alpha) + e^{i\omega_{\mathsf{a}} t} + \frac{A_{\mathsf{m}}}{A_{\mathsf{a}}}(\alpha) \cdot e^{i\omega_{\mathsf{m}} t} e^{-r^*_{2,\mathsf{m}} t} \right) \cdot e^{-R^*_2 t} \cdot \mathrm{sinc}(a \cdot t) \ . \tag{6.6}$$

Fitting procedure The four different models described above were fitted to FDM and magnitude data using non-linear least squares analysis (Matlab, MathWorks function lsqnonlin). Signal fractions and relaxation rates were restricted to non-negative values, no limits were applied to the frequency offsets. Subsequently, the resulting values ${}^{A_{\mathsf{m}}}\!/_{A_{\mathsf{a}}}(\alpha)$ were compared to a model of relative signal fractions from Eq. (6.2):

$$\frac{A_{\mathsf{m}}}{A_{\mathsf{a}}}(\alpha) = c \cdot \frac{L_{\mathsf{m}}(\alpha)}{L_{\mathsf{a}}(\alpha)} \ , \tag{6.7}$$

where c is a volume-fraction- and proton-density-dependent value, and $L_{\mathsf{e/a/m}}(\alpha)$ is defined in equation (6.2). In practice the slice profile must be considered in this

Table 6.1.: B_1 values in % of the target flip angle calculated for the splenium of the corpus callosum for all subjects.

Subject number	1	2	3	4	5
B_1 [% of the target α]	103	112	109	97	104

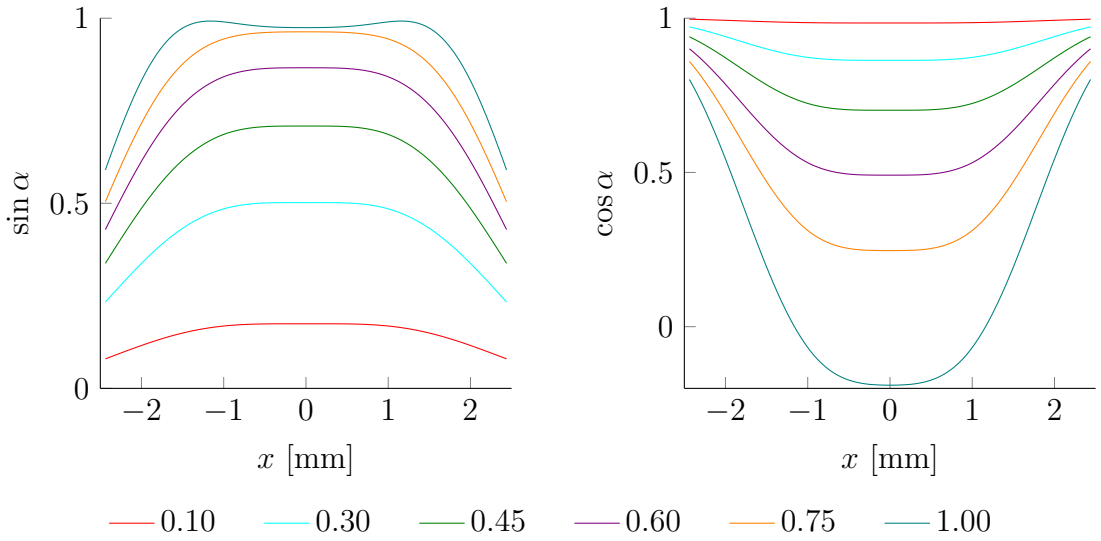


Figure 6.7.: An example of RF-amplitude-dependent slice profiles for subject 5.

analysis. The slice profiles were calculated using a Bloch equations simulator, based on the RF pulse shape, B_1-weighted RF pulse amplitude and bandwidth, as well as the slice-selective gradient amplitude, yielding the variation of $\sin\alpha$ and $\cos\alpha$ over the slice (Figure 6.7). This means, that $L_{\mathrm{e/a/m}}(\alpha)$ varies across the slice and therefore we have to estimate $L_{\mathrm{e/a/m}}(\alpha)$ as the arithmetic mean of $L_{\mathrm{e/a/m}}(\alpha(x))$. B_1 values as % of the target flip angle were calculated for the splenium of the corpus callosum for all subjects (Table 6.1).

6.3. Results

We observed that the FDM contrast increases with the excitation angle for all subjects.

The example frequency difference maps in Figure 6.3 show the effect of the excitation pulse amplitude on the magnitude and FDM data at the echo time of $14\,\mathrm{ms}$. They also indicate the difference between the FDM images before and after the spatial correction for eddy-current-related field variation. The corpus callosum and blood vessels are the regions which show strong local frequency variation and large difference in relaxation rates between the sub-voxel compartments, and therefore are prominent in the frequency difference map in Figure 6.3e. The contrast increases with increased RF amplitude, Figure 6.3f. In Figure 6.8 the mean frequency difference data from the splenium of the corpus callosum is plotted against the echo time for each of the subjects along with 3-pool model fits based on Eq. (6.3). The fast decay of the myelin water signal is reflected in the increasingly negative frequency difference in the first 10-$15\,\mathrm{ms}$ before a plateau is achieved when the white matter signal predominantly originates from the external and axonal compartments.

Figure 6.9a shows the fitted values of ${}^{A_\mathsf{m}}\!/_{A_\mathsf{a}}(\alpha)$, normalised by the scaling factor c estimated from Eq. (6.7), plotted against α, and the results from fitting the data to (6.7). The normalisation factor was set to the parameter c from equation (6.7). Figure 6.9b shows ${}^{L(T_{1,\mathsf{short}})}\!/_{L(T_{1,\mathsf{long}})}(\alpha)$ curves, which were simulated for three pairs of short, $T_{1,\mathsf{short}}$, and long, $T_{1,\mathsf{long}}$, longitudinal relaxation times as indicated in the legend. Despite the large rage of T_1-values, the simulated curves are very similar. Figure 6.10 shows values for ${}^{A_\mathsf{m}}\!/_{A_\mathsf{a}}$ and ${}^{A_\mathsf{e}}\!/_{A_\mathsf{a}}$ as a function of the RF pulse amplitude from version (iv) of the 3-pool model.

Figure 6.11 shows the spread of the fitted values for the frequency offsets of the axonal, f_a, and myelin, f_m, compartments, and the difference between these offsets, $f_\mathsf{m} - f_\mathsf{a}$, across the subjects, as estimated for each of the suggested models. Figure 6.12 compares the fitted values for the relaxation rates estimated for models in (ii), (iii) and

Table 6.2a.: Reference values from Sati et al. (2013) for the human splenium of the corpus callosum. The subscripts 1, 2, and 3 are associated with the myelin, external and axonal water pools. Flip angle and repetition time in this reference were $\alpha = 70°$ and $\mathrm{TR} = 1\,\mathrm{s}$, respectively.

A_1 [%]	$R^*_{2,1}$ [Hz]	Δf_1 [Hz]	A_2 [%]	$R^*_{2,2}$ [Hz]	Δf_2 [Hz	A_3 [%]	$R^*_{2,3}$ [Hz]	Δf_3 [Hz]
12.6(1.1)	164.2(20.1)	31.8(2.3)	50.1(2.4)	39.5(1.5)	2.0(0.2)	37.3(2.2)	24.1(2.9)	−4.1(0.7)

Table 6.2b.: Reference values from Wharton and Bowtell (2012). The subscripts I and A are associated with isotropic and anisotropic susceptibility, SP and LP are associated with small pool (equivalent to myelin water pool) and large pool (external and axonal water pools). Flip angle and repetition time in this reference were $\alpha = 14°$ and $\mathrm{TR} = 38\,\mathrm{ms}$, respectively.

$T^*_{2\text{-SP}}$ [ms]	$T^*_{2\text{-LP}}$ [ms]	χ_{I} [ppb]	χ_{A} [ppb]	$\chi_{\mathsf{I\text{-}LP}}$ [ppb]	g-ratio r/R
10 ± 2	38 ± 2	-60 ± 20	-120 ± 20	-20 ± 10	0.8

(iv). The boxplots in Figure 6.13 show the spread of the fitted values for the relative signal fraction ${}^{A_\mathsf{m}}/_{A_\mathsf{a}}(0.1 \cdot \alpha_{\mathsf{max}})$ and ${}^{A_\mathsf{e}}/_{A_\mathsf{a}}$.

We compared the fitted parameters to values estimated from the complex data acquired with MEGE scan at low flip angle by Wharton and Bowtell (2012) and Sati et al. (2013). The best fitting parameters were compared to the reference values for the splenium of the human corpus callosum published by Sati et al. (2013) listed in Table 6.2a as follows: in Figure 6.11 the frequency offset f_m was compared to the value $\Delta f_1 - \Delta f_2$, and f_a to the value $\Delta f_3 - \Delta f_2$; in Figure 6.12 the effective transverse relaxation rate R^*_2 was compared to $R^*_{2,2}$ and $R^*_{2,3}$; and the relative effective transverse relaxation rate of myelin water $r^*_{2,\mathsf{m}}$ to $R^*_{2,1} - R^*_{2,2}$ and $R^*_{2,1} - R^*_{2,3}$; in Figure 6.13 the relative signal fraction ${}^{A_\mathsf{m}}/_{A_\mathsf{a}}$ was compared to ${}^{A_1}/_{A_3}$, and ${}^{A_\mathsf{e}}/_{A_\mathsf{a}}$ to ${}^{A_2}/_{A_3}$. The values for the frequency offsets and relaxation rates were also compared to the values estimated from Wharton and Bowtell (2012) listed in Table 6.2b as follows: in Figure 6.11 the frequency offsets f_m and f_a were compared to the value $(\Delta\omega^\mathsf{A} + \Delta\omega^\mathsf{I} - \Delta\omega^{\mathsf{I\text{-}LP}})/2\pi$, estimated from

the anisotropic (A) and isotropic susceptibility values, and g-ratio in Table 6.2b using expressions in equations (2.64) and (2.65) for $r < \rho \leq R$ and $\rho \leq r$, respectively; in Figure 6.12 the effective transverse relaxation rate R_2^* was compared to ${}^1/_{T^*_{2\text{-LP}}}$; and the relative effective transverse relaxation rate of myelin water $r^*_{2,\text{m}}$ was compared to ${}^1/_{T^*_{2\text{-SP}}} - {}^1/_{T^*_{2\text{-LP}}}$.

Additionally, we compared the signal models described in (ii), (iii) and (iv) for the FDM and magnitude data evolution in Figure 6.14.

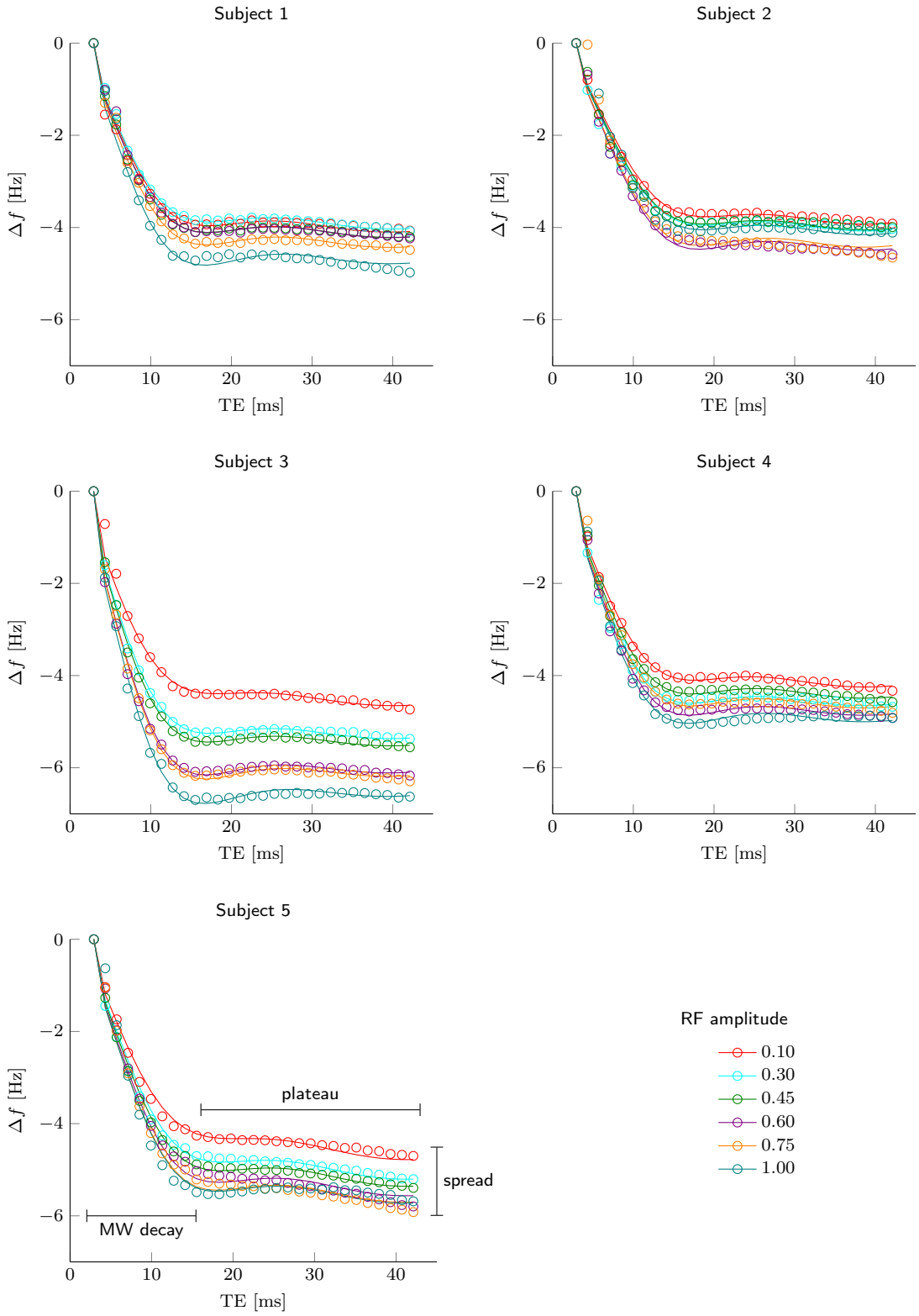


Figure 6.8.: FDM data from the splenium comparison across the subjects along with the best fitting curves for all RF excitation pulses.

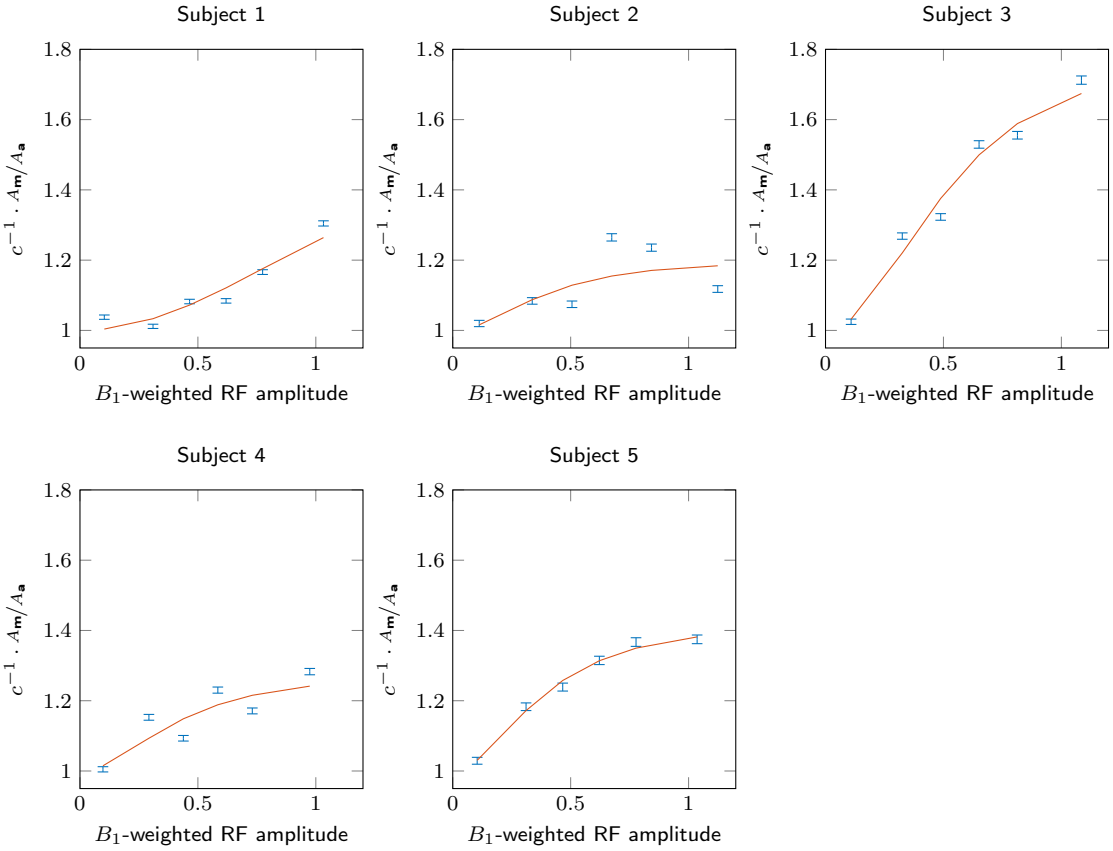


Figure 6.9a.: Relative signal fraction ${}^{A_m}/_{A_a}(\alpha)$ dependence on RF excitation pulse amplitude was modelled using $c \cdot {}^{L_m}/_{L_a}(\alpha)$ and normalised by c from Eq. (6.7).

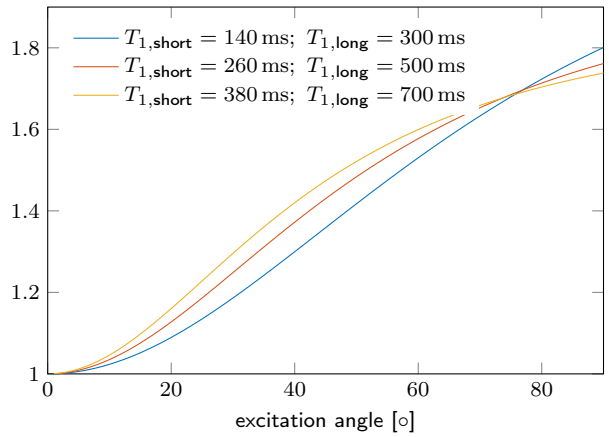


Figure 6.9b.: ${}^{L(T_{1,\text{short}})}/_{L(T_{1,\text{long}})}(\alpha)$ curves were modelled for three pairs of $T_{1,\text{short}}$ and $T_{1,\text{long}}$ show very similar behaviour despite the large range of the values.

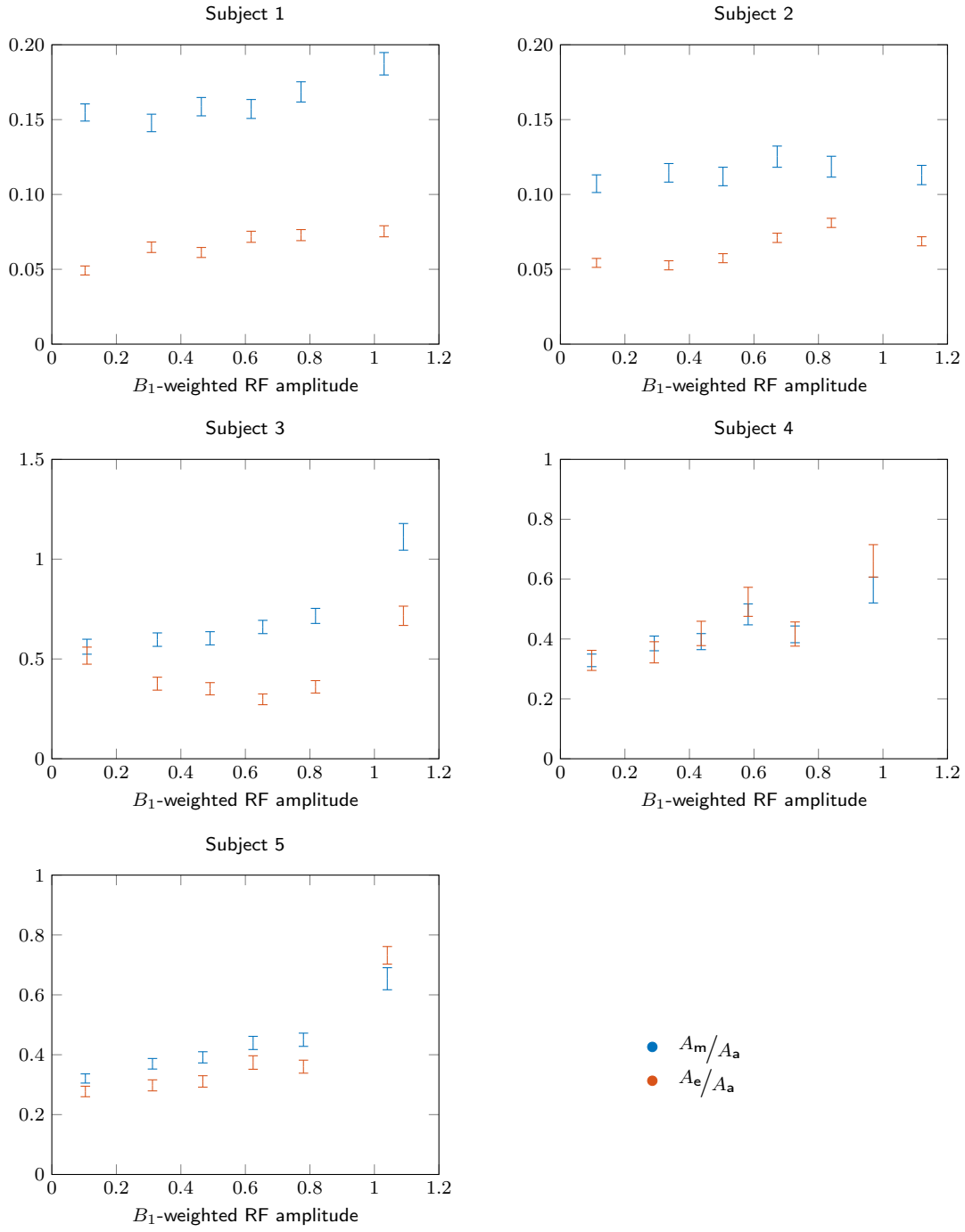


Figure 6.10.: Values A_m/A_a and A_e/A_a as a function of RF pulse amplitude were estimated from the joint fitting of the FDM and magnitude data by version (iv) of the 3-pool model.

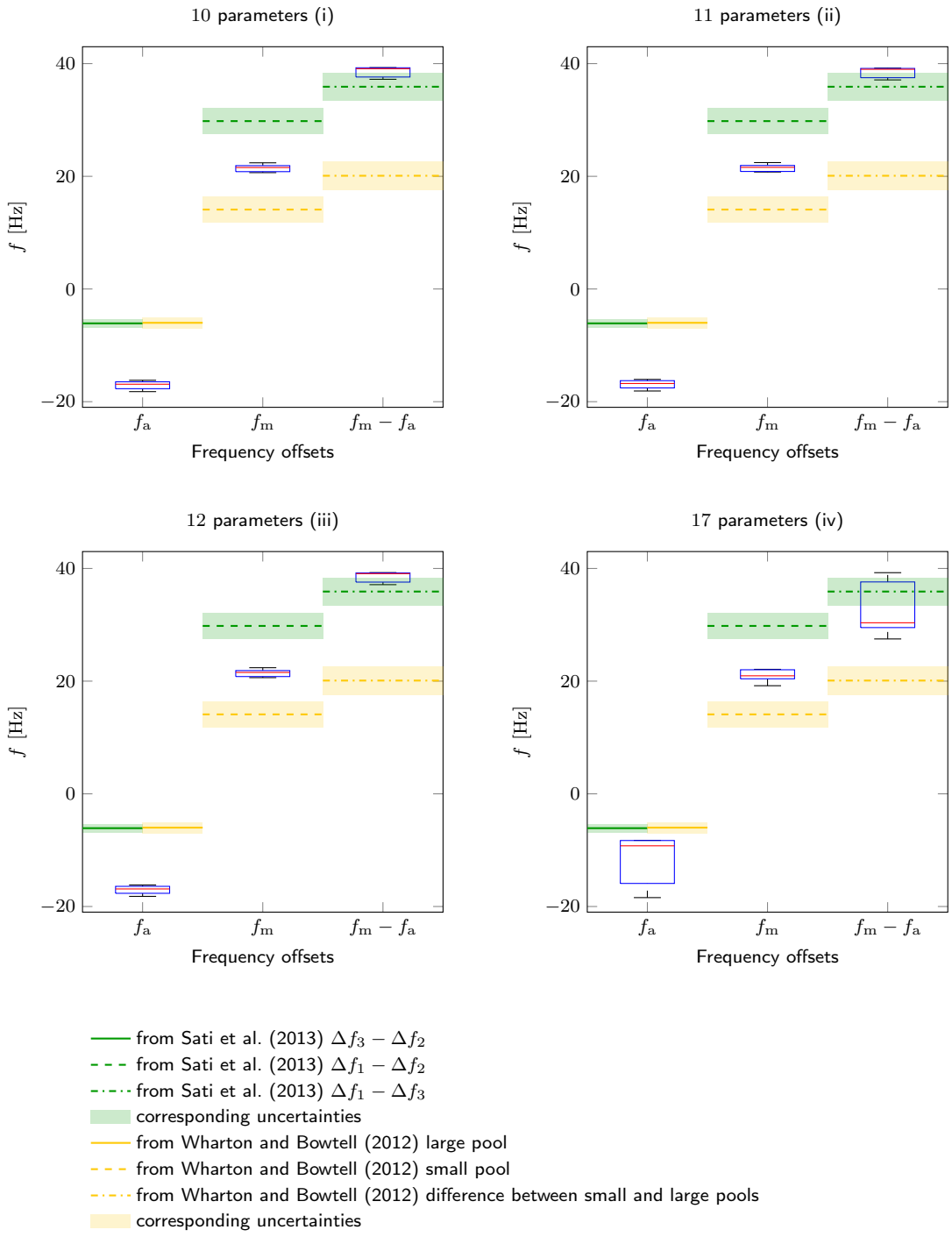


Figure 6.11.: Comparison of the frequency offsets in myelin water pool, f_m, and axonal water pool, f_a, estimated from all subjects by fitting 4 different modifications of the 3-pool model (i)-(iv) to the complex signal evolution. The boxplots show the variation of the values f_m, f_a, and $f_m - f_a$, across the subjects. The yellow and green values indicate the corresponding reference values from Wharton and Bowtell (2012); Sati et al. (2013).

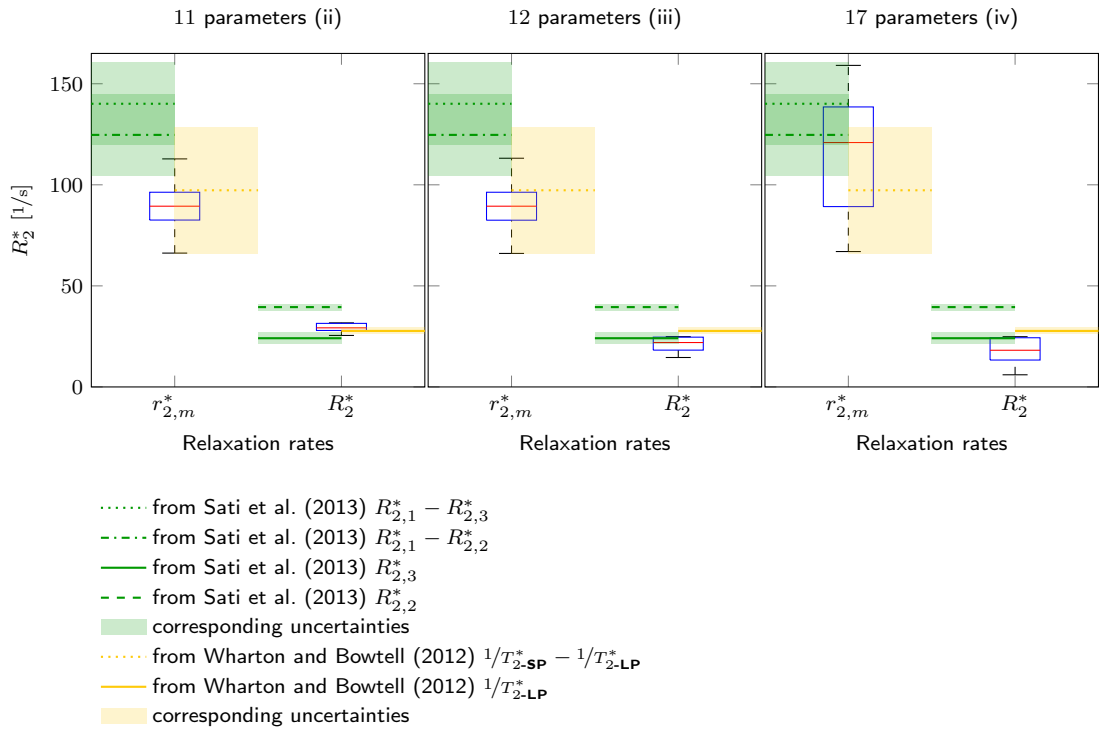


Figure 6.12.: Comparison of the relative relaxation rates of myelin water $r_{2,\mathrm{m}}^*$ and absolute relaxation rates R_2^* estimated from all subjects by joint fitting of FDM and magnitude data evolution to 3 modifications (i)-(iv) of the 3-pool model. The boxplots show the spread of the values $r_{2,\mathrm{m}}^*$, and R_2^*, across the subjects. The yellow and green values indicate the corresponding reference values from Wharton and Bowtell (2012); Sati et al. (2013).

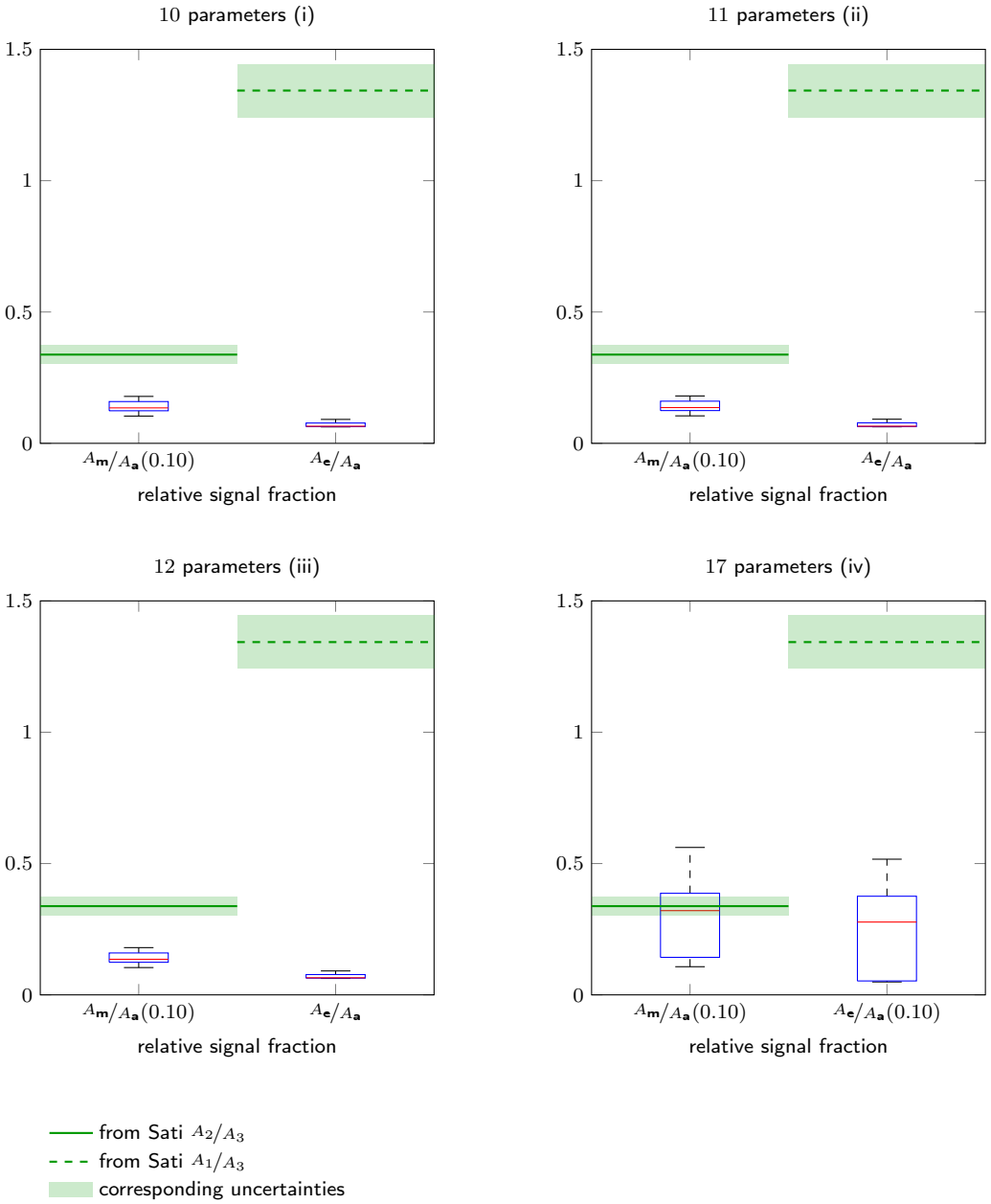
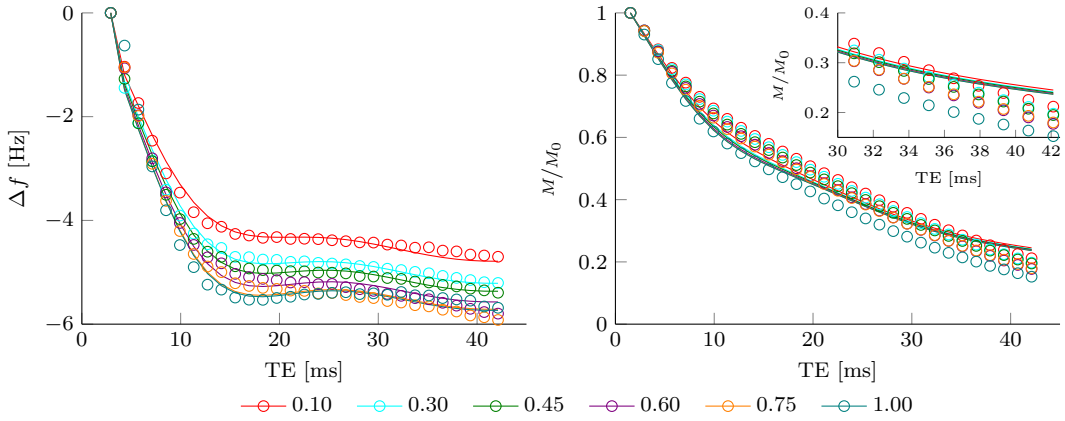
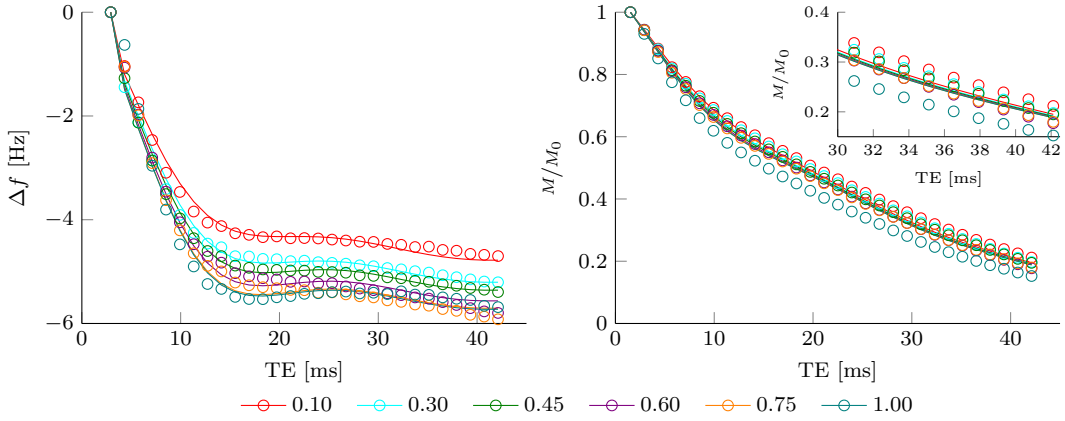


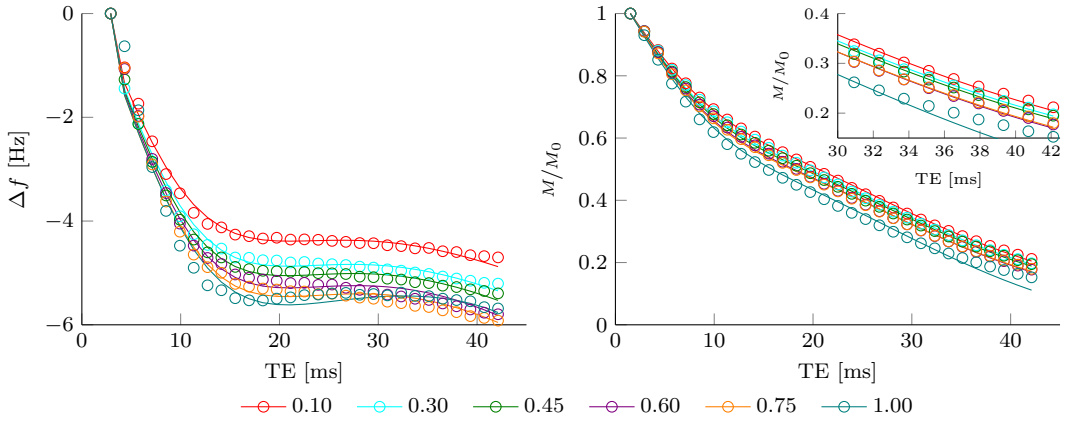
Figure 6.13.: Fitted values for relative signal fractions at the smallest RF pulse amplitude from all subjects are displayed in the boxplots. The green values indicate the corresponding reference values from Sati et al. (2013).



(a) Joint fit of FDM and magnitude data, signal modelled using 3-pool 11-parameter model, (ii).



(b) Improvement of the fit by including a factor $\mathrm{sinc}(a \cdot \mathrm{TE}_n)$ into the signal model from (a), (iii).



(c) The relative signal fractions A_e/A_a are allowed to vary with the flip angle, (iv).

Figure 6.14.: Joint FDM and magnitude data fitting for different number of parameters is show on example of one subject. The effect of the fitting the magnitude data is magnified for the echo times 30-42 ms.

6.4. Discussion

Figure 6.3e and 6.3f show that the FDM contrast in the corpus callosum changes with B_1. These images were created for $\mathrm{TE} = 14\,\mathrm{ms}$ selected as an echo time when signal from myelin water has significantly decayed. The frequency difference value at this echo time is thus linked to the signal fraction of the myelin water pool: the larger the signal fraction of the myelin water pool the higher the absolute value of the FDM. The data thus implies that the long-T_2^* water pool is more saturated than the short-T_2^* water pool at higher flip angle, which could be explained by correlation of transverse and longitudinal relaxation times, as suggested by Labadie et al. (2014); Kim et al. (2015).

Figure 6.8 shows that the evolution of the FDM signal from the splenium was similar across subjects: there was a rapid change in frequency difference in the first 15-$20\,\mathrm{ms}$ followed by a nearly constant frequency difference value at the echo times above $20\,\mathrm{ms}$. At low-amplitude RF excitation the frequency difference values were very similar for all subjects, and the FDM generally increased with flip angle. The variation of the frequency differences with RF pulse amplitudes at long TE is about 1-$1.5\,\mathrm{Hz}$ for all subjects apart from subject 3, where it exceeds $2\,\mathrm{Hz}$. This behaviour is reflected in the dependence of the fitted parameters for the relative signal fraction of myelin water ${}^{A_\mathsf{m}}\!/_{A_\mathsf{a}}$ on RF pulse amplitude: the larger the change of the frequency difference with RF amplitude (Figure 6.8), the larger is the variation of $c^{-1}{}^{A_\mathsf{m}}\!/_{A_\mathsf{a}}(\alpha)$ with RF amplitude (Figure 6.9a).

However, the absolute T_1 values cannot be estimated accurately from the relative signal fraction. The values are larger than the corresponding uncertainties only for subjects 3 and 5: $T_{1,\mathsf{m}} = 260 \pm 120\,\mathrm{ms}$, $T_{1,\mathsf{a}} = 505 \pm 215\,\mathrm{ms}$, and $T_{1,\mathsf{m}} = 570 \pm 146\,\mathrm{ms}$,

$T_{1,\mathsf{a}} = 830 \pm 210\,\mathrm{ms}$, respectively. To illustrate, why it is difficult to estimate T_1 values using this method, we calculated the variation of ${}^{L(T_{1,\mathsf{short}})}/_{L(T_{1,\mathsf{long}})}(\alpha)$ with flip angle based on three pairs of $T_{1,\mathsf{short}}$ and $T_{1,\mathsf{long}}$ values and plotted them against the flip angle ranging from 0° to 90° in Figure 6.9b. The three pairs of short and long longitudinal relaxation times were selected from $T_{1,\mathsf{m}}$ and $T_{1,\mathsf{a}}$ values estimated from the data for subject 3: lower confidence bound, actual value, and upper confidence bound. It is evident, that the curves only show small sensitivity to T_1, there is only a small difference between these curves. This means that based on our data we only can estimate some proportionality relation between both values and their range, but not the absolute values. The values for the proportionality constant c can be estimated more accurately from the fit since they are similar to the relative signal fraction value at the smallest excitation angle: $c = 0.174 \pm 0.007$ (subject 3), and $c = 0.148 \pm 0.002$ (subject 5).

Comparison between the modifications of the 3-pool model In this work we explored four variations of the 3-pool model described in items (i)-(iv) in Section 6.2: 3-pool model with 10 parameters was used for fitting the FDM data (i), and 3-pool model with 11, 12 and 17 parameters was used for the joint fitting of the FDM and magnitude data (ii)-(iv). We compared the values of the frequency offsets $f_{\mathsf{m}} = {}^{\omega_{\mathsf{m}}}/_{2\pi}$ and $f_{\mathsf{a}} = {}^{\omega_{\mathsf{a}}}/_{2\pi}$ and the difference $f_{\mathsf{m}} - f_{\mathsf{a}}$ across the subjects (predicted using these models) in Figure 6.11. The fitted values of the frequency offset of myelin water f_{m} are in very good agreement across all the subjects for all four models. The agreement across the subjects for the frequency offset of the axonal water f_{a} is very good when 3-pool model is fitted for 10, 11 or 12 parameters, but worsens when 17 parameters are used. Consequently, the same is true for the difference between the frequency

offsets. The frequency offset value for the myelin water f_{m} appears to be the most stable value in all fitting procedures. The value for f_{m} we estimated is higher than the reference value from Wharton and Bowtell (2012) but lower than the reference value from Sati et al. (2013). Our value for f_{a} is about $10\,\mathrm{Hz}$ lower that both reference values. The difference between the frequency offsets $f_{\mathsf{m}} - f_{\mathsf{a}}$ agrees well with the reference value from Sati et al. (2013), but is about $20\,\mathrm{Hz}$ higher than the reference value from Wharton and Bowtell (2012).

In Figure 6.12 we compared the relative relaxation rates of myelin water $r^*_{2,\mathsf{m}}$ and the absolute relaxation rates of external and axonal water pools R^*_2 obtained from the 3-pool model adaptation for joint FDM and magnitude data fitting (ii)-(iv). The values for the absolute relaxation rates, R^*_2, agree well across the subjects for all three models and agree with the reference values for the relaxation rates for the large pool $1/T^*_{2,\mathsf{LP}}$ in Wharton and Bowtell (2012) and for the axonal pool, $R^*_{2,3}$ in Sati et al. (2013). The relative relaxation rates for myelin water $r^*_{2,\mathsf{m}}$ appear to show a larger spread between the subjects. The values for $r^*_{2,\mathsf{m}}$ are similar to the value estimated by Wharton and Bowtell (2012) but they are significantly lower than the reference value from Sati et al. (2013).

In Figure 6.13 we compare the relative signal fractions $A_{\mathsf{m}}/A_{\mathsf{a}}$ and $A_{\mathsf{e}}/A_{\mathsf{a}}$ estimated at the smallest RF excitation pulse (nominal $\alpha = 8°$). Similarly to the frequency offset values, the relative signal fractions agree very well across the subjects for the 3-pool model variants, where $A_{\mathsf{e}}/A_{\mathsf{a}}$ was fixed for all the excitation pulses, and show a larger spread across the subjects, when we allowed these values to vary with flip angle. Also, the relative signal fraction $A_{\mathsf{m}}/A_{\mathsf{a}}$ was half the value of the reference value and $A_{\mathsf{e}}/A_{\mathsf{a}}$ only about $1/20$ of the reference values.

We have seen, that the fitted values agree very well across the subjects when $A_{\mathsf{e}}/A_{\mathsf{a}}$

was kept constant for all flip angles. If we compare the methods for joint magnitude and FDM data fitting in Figure 6.14, first we can see that including $\mathrm{sinc}(a \cdot t)$ into signal model provides a better description of the magnitude evolution at later echoes, Figure 6.14b. At the same time, neither Figure 6.14a nor Figure 6.14b can explain the spread of the data across the excitation pulses, while Figure 6.14c matches the data better. However, the improved fit to the magnitude data in Figure 6.14c could be a result of under-constrained fitting as indicated by increased spread of fitted parameters. This disagreement between the good fit of the FDM data and worse fit to the magnitude data needs further investigation and more advanced modelling.

Relative signal fraction of MW It is evident from Figure 6.9a that the relative signal fraction of myelin water ${}^{A_{\mathsf{m}}}/_{A_{\mathsf{a}}}$ consistently increases with increasing amplitude of the excitation angle across subjects for the variants (i)-(iii) of the 3-pool model. However based on the short and long T_1 values of myelin water estimated by Labadie et al. (2014), the expected difference between the ${}^{L(T_{1,\mathsf{short}},10^\circ)}/_{L(T_{1,\mathsf{long}},10^\circ)}$ and ${}^{L(T_{1,\mathsf{short}},90^\circ)}/_{L(T_{1,\mathsf{long}},90^\circ)}$ is at least 5 times higher, than the maximum difference we observe in our experiments. It has been observed that magnetisation transfer (MT) techniques are sensitive to the myelin water pool (Henkelman et al. (2001)). Additionally, the saturation of the MT pool increases with increasing RF amplitude and therefore possibly opposes the effect of the lesser saturation of the myelin water pool due to its shorter longitudinal relaxation time. Zhang et al. (2015) investigated the MT effect on a balanced steady-state approach by comparing the signal intensity from using short or long RF pulses producing the same flip angle. They observed that the signal intensity in white matter has significantly increased, when the short RF pulses were replaced by the long RF pulses, and interpreted this result as a reduction of the

MT effect due to the longer RF pulses.

Another hypothesis is that there is a greater exchange from the myelin water pool into the axonal water pool, than to the external water pool. This would explain the reduced values of ${}^{A_\mathrm{e}}/_{A_\mathrm{a}}$ and ${}^{A_\mathrm{m}}/_{A_\mathrm{a}}$, but not a much larger negative frequency offset f_a in the axonal compartment.

6.5. Conclusion

We have shown that the relative signal fraction of myelin water consistently increases with increasing amplitude of the excitation angle across subjects. This is consistent with lesser saturation of the myelin water compartment and hence this compartment having a shorter T_1 compared to that of the axonal and external compartments. We observed a much smaller difference between the saturation of the myelin and axonal/external water pools, than expected based on the previously reported values (Labadie et al. (2014)). This could be explained by a stronger MT effect in the myelin water pool and by increased MT-weighting with the increasing RF amplitude, but also by a possible greater exchange from the myelin water pool into the axonal water pool, than into the external water pool.

The MT effect on this MEGE setup could be investigated by adding MT saturation pulses prior to the sequence, and observing its effect on the FDM data. We would expect a stronger saturation of the myelin water pool due to the additional MT pulse and therefore a lower frequency difference.

7. Diffusion-Weighted Asymmetric Spin-Echo imaging to probe white matter microstructure

7.1. Introduction

We have seen that intra-axonal and external compartments' contributions to the complex MEGE signal evolution are barely distinguishable due to their similar effective transverse relaxation times. The application of diffusion-weighted spin echo imaging allows us to separate the signals from the external and axonal water pools. Moreover, by applying diffusion weighting perpendicular to white matter fibres, we can reduce the contribution from the external water pool to the total signal while the attenuation of the axonal water signal is negligible at long diffusion times as illustrated in Figure 7.1. The diffusion in the external compartment is referred to as *hindered diffusion* and in the intra-axonal compartment as *restricted diffusion* (Assaf et al. (2004)).

In this chapter we propose to access microstructural information about white matter

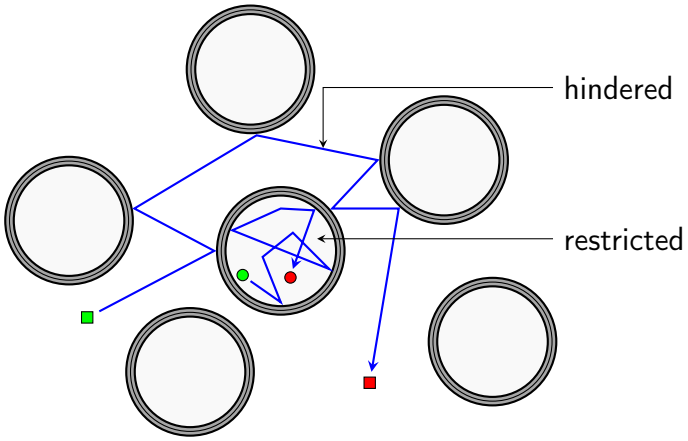


Figure 7.1.: Illustration of hindered and restricted Brownian motion of water molecules perpendicular to fibres in white matter. For the same path length between the start and end points of the motion, a water molecule in the hindered compartment, □, will travel further than that in the restricted compartment, ○. Thus, the signal attenuation in the restricted compartment can no longer be approximated as Gaussian, and the signal attenuation is greatly reduced.

by separating the signals from the intra-axonal and external compartments by performing a diffusion-weighted, asymmetric spin echo (DW-ASE) experiment with diffusion weighting applied perpendicular to the white matter fibres and with the fibre-orientation perpendicular to the magnetic field $\vec{B}_0$.

7.2. Complex signal of DW-ASE

In this section we introduce the DW-ASE complex signal modelling based on the differences in the diffusivity, relaxivity, and magnetic properties of the intra-axonal and external water pools.

With its transverse relaxation rate of $T_2 < 20\,\mathrm{ms}$, Bouhrara and Spencer (2017), the myelin water transverse magnetisation is assumed to be negligibly small at the spin echo times of $50\,\mathrm{ms}$ and above used in the DW-ASE sequence. We also assume, that at long diffusion times and low b-values the signal attenuation due to diffusion of the

axonal water pool is negligible when the diffusion weighting is applied perpendicular to the fibres. Therefore, the diffusion-weighted, asymmetric spin echo signal evolution, $S(b, \Delta t)$, as a function of b-value and acquisition delay, Δt, can be modelled as a superposition of the axonal and external water signals:

$$S(b, \Delta t) \sim S_{\mathsf{a}}(\Delta t) + S_{\mathsf{e}}(b, \Delta t) \tag{7.1}$$

$$= A_{\mathsf{a}} \cdot e^{-R^*_{2,\mathsf{a}}\Delta t} \cdot e^{i\omega\Delta t} + A_{\mathsf{e}} \cdot e^{-bD} \cdot e^{-R^*_{2,\mathsf{e}}\Delta t} \tag{7.2}$$

$$= \Bigg(\underbrace{\frac{A_{\mathsf{a}}}{A_{\mathsf{e}}}}_{=f} \cdot e^{i\omega\Delta t} + \underbrace{e^{-bD}}_{=E_D} \cdot \underbrace{e^{-r^*_2\Delta t}}_{=E_2} \Bigg) \cdot A_{\mathsf{e}} \cdot e^{-R^*_{2,\mathsf{a}}\Delta t} \ . \tag{7.3}$$

The subscripts a and e stand for the intra-axonal and external water pools. The parameters A and R^*_2 represent the signal fraction and transverse relaxation rate, ω denotes the frequency offset between the intra-axonal and external water pools, D stands for the apparent diffusion constant of the external water pool, and $r^*_2 = R^*_{2,\mathsf{e}} - R^*_{2,\mathsf{a}}$. Throughout this chapter we assume that $A_{\mathsf{a}} + A_{\mathsf{e}} = 1$. The initial value for the external signal attenuation function E_D is $E_D(b = 0) = 1$. For the relative transverse signal attenuation function E_2 the initial value is $E_2(\Delta t = 0) = 1$. The proportionality parameter f and the frequency offset ω reflect the geometry for fibres perpendicular to the magnetic field $\vec{B}_0$ as follows:

$$f = \frac{A_{\mathsf{a}}}{A_{\mathsf{e}}} = \frac{V_{\mathsf{a}}}{V_{\mathsf{e}}} = \frac{\pi r^2/V}{1 - \pi R^2/V}$$
$$= \left[\frac{r}{R}\right]^2 \cdot \frac{\pi R^2/V}{1 - \pi R^2/V} \ , \tag{7.4}$$

and

$$\omega = \frac{3}{4}\chi^{\mathsf{A}}\gamma B_0 \ln\frac{R}{r} \ . \tag{7.5}$$

The radii r and R are the average inner and outer radii of the fibres, V_{a}, V_{e} and V are intra-axonal, extra-axonal and total volumes, respectively, ${}^{\pi R^2}/_{V}$ is the fibre volume fraction, and χ^{A} is the anisotropic susceptibility of the the myelin sheath. The ratio ${}^{r}/_{R}$ is known as the g-ratio.

Signal attenuation due to Brownian molecular motion is generally defined as the ratio of the signals at $b > 0$ and $b = 0$, which for the two-pool model is given by:

$$\frac{S(b,t)}{S(0,t)} = \frac{f \cdot e^{i\omega\Delta t} + E_D \cdot E_2}{f \cdot e^{i\omega\Delta t} + E_2} \tag{7.6}$$

$$= \frac{f \cdot [\cos(\omega\Delta t) + i \cdot \sin(\omega\Delta t)] + E_D \cdot E_2}{f \cdot [\cos(\omega t) + i \cdot \sin(\omega\Delta t)] + E_2} \ . \tag{7.7}$$

We can calculate the magnitude of the signal attenuation as:

$$\left|\frac{S(b,\Delta t)}{S(0,\Delta t)}\right| = \left[\frac{[E_D \cdot E_2 + f \cdot \cos(\omega\Delta t)]^2 + [f \cdot \sin(\omega\Delta t)]^2}{[E_2 + f \cdot \cos(\omega\Delta t)]^2 + [f \cdot \sin(\omega\Delta t)]^2}\right]^{1/2} \ . \tag{7.8}$$

For $\Delta t = 0$ the magnitude of signal attenuation due to diffusion weighting is:

$$\left|\frac{S(b,0)}{S(0,0)}\right| = \frac{E_D + f}{1 + f} \ . \tag{7.9}$$

When the diffusion attenuation of the external compartment is large enough that $E_D \to 0$ the magnitude of signal attenuation due to T_2^*-weighting is:

$$\left|\frac{S(b,\Delta t)}{S(0,\Delta t)}\right| = \left[({}^{E_2}/_{f})^2 + 2 \cdot \cos(\omega\Delta t) \cdot {}^{E_2}/_{f} + 1\right]^{-1/2} \ . \tag{7.10}$$

The above expression is reduced to:

$$\left|\frac{S(b,\Delta t)}{S(0,\Delta t)}\right| \overset{\omega \equiv 0}{=} [{}^{E_2}/_{f} + 1]^{-1} \tag{7.11}$$

$$\overset{r_2^*\Delta t \to 0}{\approx} A_{\mathsf{a}} + A_{\mathsf{a}}(1 - A_{\mathsf{a}}) \cdot r_2^* \cdot \Delta t \ , \tag{7.12}$$

when the susceptibility of myelin sheath is purely isotropic, so there is no frequency

offset between the external and intra-axonal compartments, Eq. (7.11). The scaled signal magnitude is linear with Δt at short acquisition delays, Eq. (7.12).

The phase of the signal attenuation is:

$$\begin{aligned}\arg\left[\frac{S(b,\Delta t)}{S(0,\Delta t)}\right] &= \arg[S(b,t)] - \arg[S(0,t)] \\ &= \tan^{-1}\frac{\Im[S(b,t)]}{\Re[S(b,t)]} - \tan^{-1}\frac{\Im[S(0,t)]}{\Re[S(0,t)]} \\ &= \tan^{-1}\frac{f\cdot\sin(\omega\Delta t)}{f\cdot\cos(\omega\Delta t)+E_D\cdot E_2} - \tan^{-1}\frac{f\cdot\sin(\omega\Delta t)}{f\cdot\cos(\omega\Delta t)+E_2}\ .\end{aligned} \tag{7.13}$$

For $E_D \to 0$ the relative phase of the signal is:

$$\arg\left[\frac{S(b,\Delta t)}{S(0,\Delta t)}\right] = \omega\Delta t - \tan^{-1}\frac{f\cdot\sin(\omega\Delta t)}{f\cdot\cos(\omega\Delta t)+E_2}\ . \tag{7.14}$$

The magnitude and the phase, scaled by $2\pi\Delta t$, of the attenuated signal were calculated as a function of Δt for $E_D = 0$ using Eqs. (7.13) and (7.14), and are shown in Figure 7.2. The calculations for the red curves were performed based on the following reference values: $\Delta\omega = -2\pi\cdot 6\,\mathrm{Hz}$, $R^*_{2,\mathsf{a}} = 25\,\mathrm{s}^{-1}$, $R^*_{2,\mathsf{e}} = 40\,\mathrm{s}^{-1}$ (Wharton and Bowtell (2012); Sati et al. (2013)). The value for $\Delta\omega/2\pi$ is indicated by the black line in plot (b). The blue curves were calculated by setting the value for the frequency offset to zero: $\omega = 0\,\mathrm{Hz}$. Zero frequency offset between the external and the intra-axonal compartments would indicate that the susceptibility of the myelin sheath is purely isotropic, while the non-zero value indicates the presence of the additional anisotropic susceptibility component of the myelin sheath (Wharton and Bowtell (2012)). The dashed and solid lines were calculated using intra-axonal signal fractions of $A_\mathsf{a} = 0.3$ and $A_\mathsf{a} = 0.5$, respectively. These values are indicated by black lines in the plot (a).

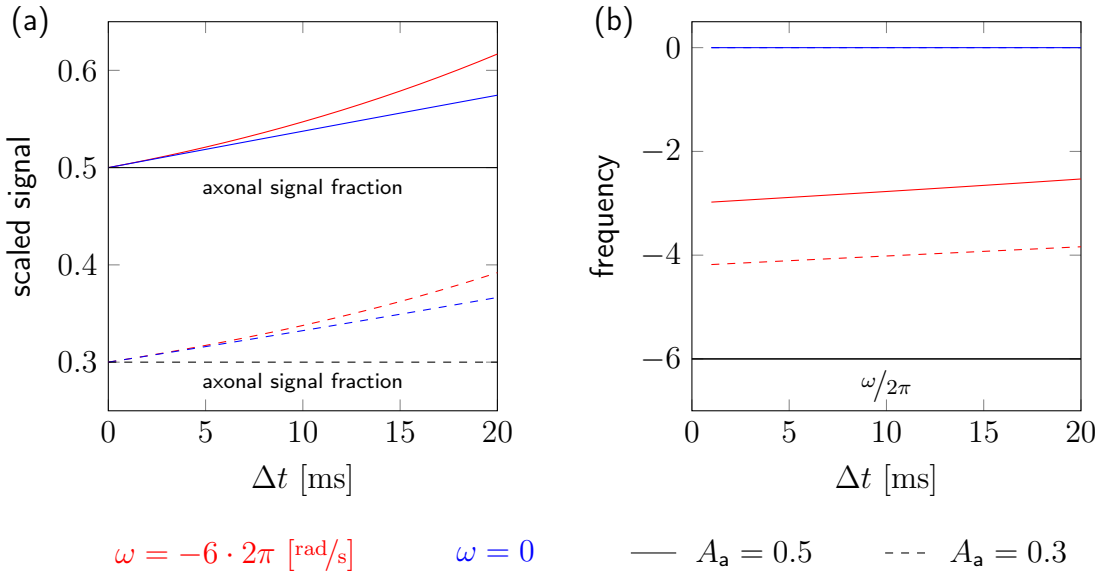


Figure 7.2.: (a) Magnitude and (b) phase scaled by $2\pi\Delta t$ of the scaled complex signal from the DW-ASE sequence as a function of the acquisition delay Δt, calculated using Eqs. (7.13) and (7.14).

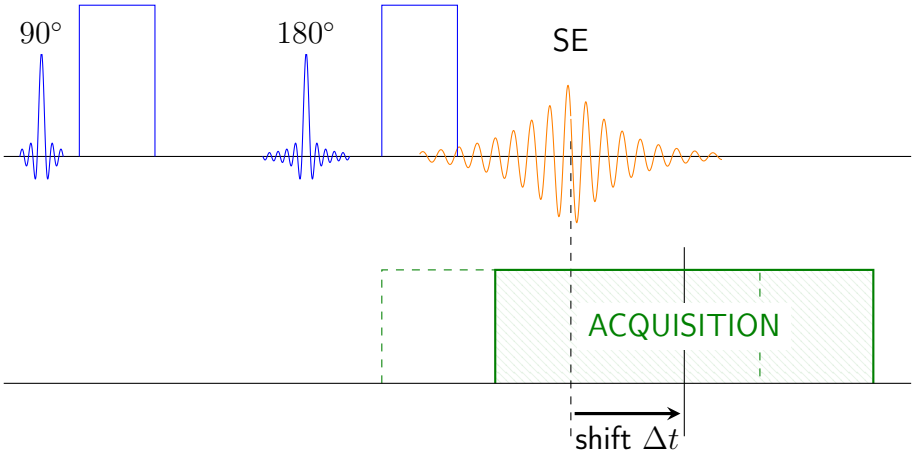


Figure 7.3.: The schematic diagram shows the spin-echo pulse sequence modification. If we shift the acquisition relative to the spin-echo, we can access phase.

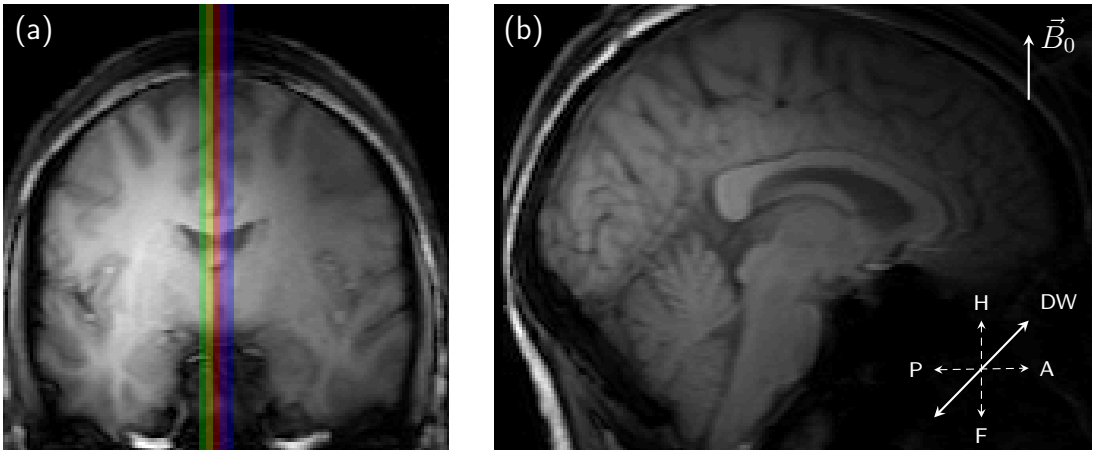


Figure 7.4.: The DW-ASE slice positioning is indicated in the coronal slice from the survey scan (a). In the sagittal slice of the survey scan (b) the magnetic field $\vec{B}_0$ and diffusion weighting (DW) orientations are indicated.

7.3. Materials and Methods

Pulse sequence programming A DW-ASE sequence was developed by modifying the standard diffusion-weighted spin echo using the pulse programming environment for the Philips $7\,\mathrm{T}$ scanner. First, we introduced a flexible delay, Δt, of the EPI readout relative to the RF spin echo, which could be varied between $0\,\mathrm{ms}$ and $50\,\mathrm{ms}$ in the exam card. In the second step, we enabled the saving of complex images, which is not a default possibility for single-shot diffusion-weighted spin echo data on the Philips scanner. The schematic diagram of the DW-ASE sequence is shown in Figure 7.3.

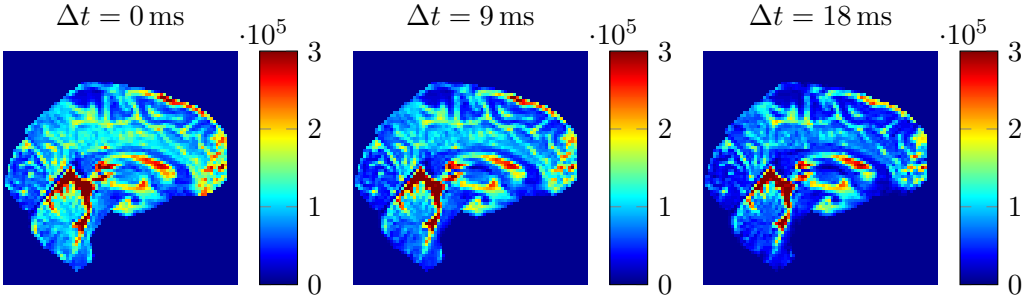
Data acquisition in-vivo DW-ASE scans were carried out on three healthy subjects ($25.0 \pm 0.2\,\mathrm{y}$, 2 female) using the whole-body $7\,\mathrm{T}$ scanner. The diffusion weighting was applied in a single direction perpendicular to the fibre orientation in the corpus callosum by jointly applying diffusion gradients along the anterior-posterior (AP) and foot-head (FH) directions. Thus, we could reduce the minimum required spin echo time, $\mathrm{TE}_{\mathrm{SE}}$,

necessary to achieve b-values up to $1200\,{}^{\mathrm{s}}/_{\mathrm{mm}^2}$, from $80\,\mathrm{ms}$ for diffusion gradients along the AP or FH axis, to $71\,\mathrm{ms}$ for diffusion gradients applied along the intermediate (AP and FH) axis. We acquired images at 4 equally spaced b-values ranging between 0 and $1200\,{}^{\mathrm{s}}/_{\mathrm{mm}^2}$ at $\mathrm{TE}_{\mathsf{SE}} = 71\,\mathrm{ms}$.The echo was delayed by $\Delta t = 0,\ 9,$ and $18\,\mathrm{ms}$ to enable T_2^*-weighting of the spin echo signal. For Subjects 2 and 3 the echo was also delayed by $\Delta t = 3,\ 6,\ 12,$ and $15\,\mathrm{ms}$. Five mid-sagittal slices were acquired with $2\,\mathrm{mm}$ isotropic voxel size and FOV of $256 \times 256 \times 10\,\mathrm{mm}^3$. For each b-value and echo delay, Δt, 10 dynamic scans were acquired and phase, magnitude, real and imaginary data were saved. The repetition time was set to $\mathrm{TR} = 5\,\mathrm{s}$ and the SENSE factor in the phase encoding direction was $R_{\mathsf{P}} = 2$. The slice positioning, $\vec{B}_0$ orientation and diffusion weighting direction are indicated in the images from the survey scan in Figure 7.4.

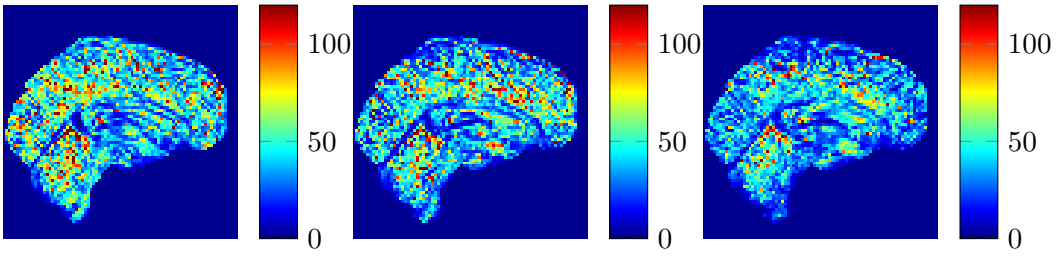
All volunteer scanning was done with full ethical permission and informed consent.

Data processing The magnitude data collected from each subject were averaged over 10 dynamic scans for all b-values and acquisition delays Δt. Signal-to-noise ratio (SNR) of the magnitude data was calculated as the ratio between the average magnitude and its standard deviation over dynamics. The averaged magnitude data, M_b, acquired with b-values above zero were scaled by the magnitude image data, M_0, acquired with $b = 0\,{}^{\mathrm{s}}/_{\mathrm{mm}^2}$ at the same value of Δt. The uncertainty of $\left[{}^{M_b}/_{M_0}\right]_{\Delta t}$ was calculated from the standard deviations δM_0 and δM_b over dynamics.

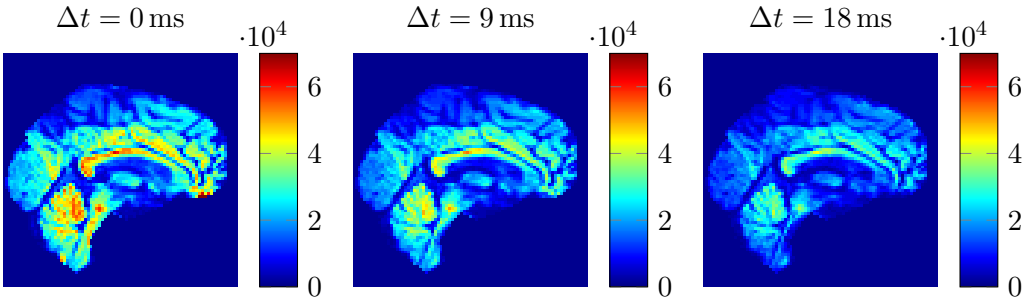
A binary mask was calculated from the regions of significant increase of $\left[{}^{M_b}/_{M_0}\right]_{\Delta t}$-values with acquisition delays. This mask was applied onto scaled magnitude images $\left[{}^{M_b}/_{M_0}\right]_{\Delta t}$ to highlight these regions.



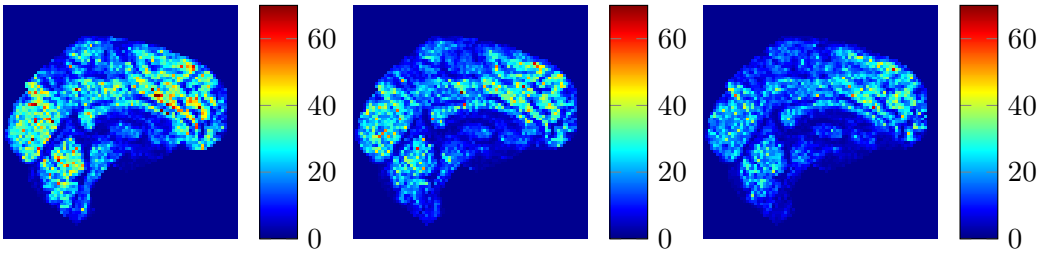
(a) The magnitude data acquired at $b = 0\,\mathrm{s/mm^2}$ were averaged over 10 dynamic scans.



(b) The magnitude data acquired at $b = 0\,\mathrm{s/mm^2}$ were averaged over 10 dynamic scans and divided by its standard deviation over the dynamics to calculate the SNR.



(c) The magnitude data acquired at $b = 1200\,\mathrm{s/mm^2}$ were averaged over 10 dynamic scans.



(d) The magnitude data acquired at $b = 1200\,\mathrm{s/mm^2}$ were averaged over 10 dynamic scans and divided by its standard deviation over dynamics to calculate the SNR.

Figure 7.5.: Magnitude data from Subject 1 were acquired at $b = 0\,\mathrm{s/mm^2}$ (a) and $b = 1200\,\mathrm{s/mm^2}$, $\mathrm{TE_{SE}} = 71\,\mathrm{ms}$ (c), using acquisition delays, Δt of 0, 9, and $18\,\mathrm{ms}$. The corresponding SNR maps calculated using standard deviation over dynamics are shown in (b) and (d), respectively.

7.4. Results

The data demonstrated in Figures 7.5 – 7.7 and 7.10 were collected from Subject 1. Data in Figures 7.8 and 7.9 were collected from Subjects 2 and 3, respectively.

Figure 7.5 shows data acquired with different values of the acquisition delay Δt, and with $b = 0\,\mathrm{s/mm^2}$ and $b = 1200\,\mathrm{s/mm^2}$, respectively. The magnitude data averaged over dynamic scans is shown in (a) and (c), and the corresponding SNR maps are shown in (b) and (d), respectively. Reduction of signal intensity and SNR with Δt in the data acquired at both b-values is evident. The data acquired at $b = 1200\,\mathrm{s/mm^2}$ shows higher relative signal in the corpus callosum and other white matter regions than the data acquired at $b = 0\,\mathrm{s/mm^2}$, compared to CSF signal. This is consistent with there being a component of slow (in this case non-Gaussian) diffusion in the selected diffusion direction perpendicular to the fibres in the corpus callosum.

Figure 7.6 shows example of magnitude data acquired with non-zero b-values, and scaled by the magnitude data acquired with $b = 0\,\mathrm{s/mm^2}$ for the same Δt-value. The images show the scaled magnitude data for different values of Δt (left to right) and of b-values (top to bottom). Figure 7.7 shows the same data zoomed onto the region of the splenium of the corpus callosum with the range of the displayed ratio values restricted to $[0.5, 1.0]$.

Figure 7.8 shows the scaled magnitude data and SNR maps (of the scaled magnitude) for different values of the acquisition delay Δt collected from Subject 2, from the whole slice (Figure 7.8 (a) and (b), respectively), and zoomed onto the region of the splenium (Figure 7.8 (c) and (d), respectively).

Figure 7.9 shows the scaled magnitude data and SNR maps as function of the acquisition delay Δt collected from Subject 3, from the whole slice (Figure 7.9 (a) and (b),

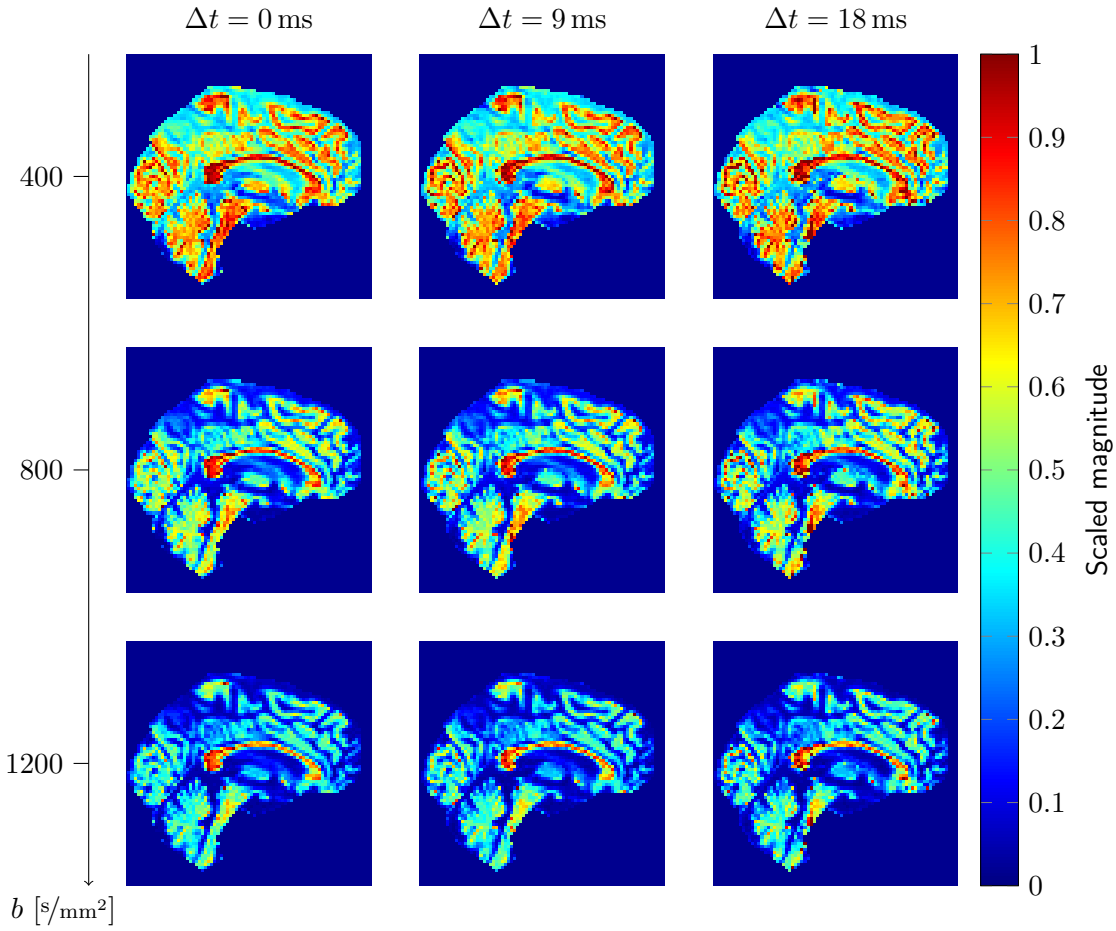


Figure 7.6.: The magnitude data (Subject 1) acquired at $\mathrm{TE}_{\mathrm{SE}} = 71\,\mathrm{ms}$ with b-values above zero, were scaled by the magnitude data acquired with $b = 0\,\mathrm{s/mm^2}$ at same Δt-value. Images show the scaled magnitude as a function of Δt (left to right) and of b-values (top to bottom).

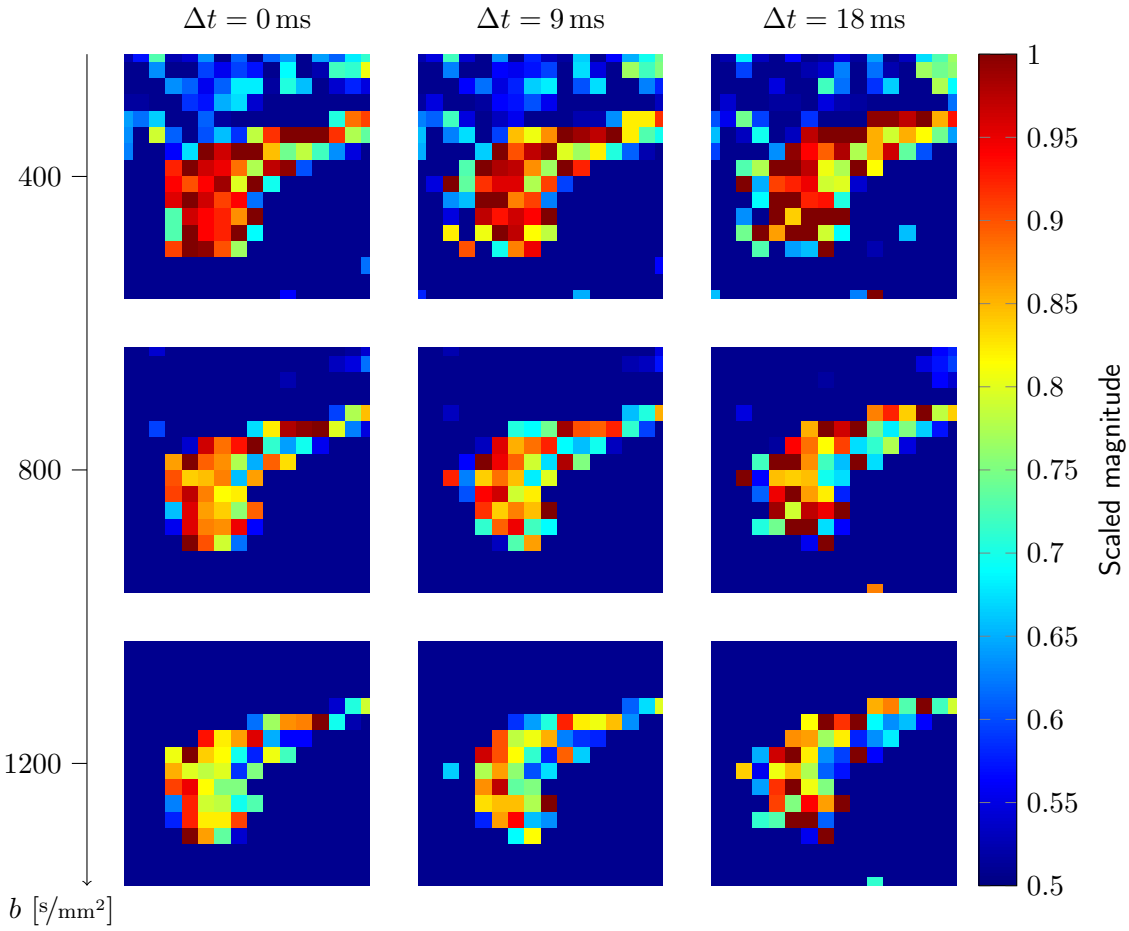


Figure 7.7.: The data shown in Figure 7.6 is zoomed onto the region of the splenium of the corpus callosum, and the scale $[0.5, 1.0]$. Images show the scaled magnitude as a function of Δt (left to right) and of b-values (top to bottom).

respectively), and zoomed region of the splenium (Figure 7.9 (c) and (d), respectively). Figure 7.10 demonstrates diffusion-weighted data, $^{M_b}/_{M_0}$, acquired at $b = 1200\,{}^{\mathrm{s}}/_{\mathrm{mm}^2}$, and $\Delta t = 0\,\mathrm{ms}$ and $\Delta t = 18\,\mathrm{ms}$, respectively, and masked in the regions of significant increase of $^{M_b}/_{M_0}$ with Δt. The increase of $^{M_b}/_{M_0}$ with Δt is significant when

$$\frac{M_b}{M_0}(18\,\mathrm{ms}) - \frac{M_b}{M_0}(0\,\mathrm{ms}) - \delta\left[\frac{M_b}{M_0}(18\,\mathrm{ms}) - \frac{M_b}{M_0}(0\,\mathrm{ms})\right] > 0\ , \tag{7.15}$$

where the uncertainty of $^{M_b}/_{M_0}$ increase with Δt is:

$$\delta\left[\frac{M_b}{M_0}(18\,\mathrm{ms}) - \frac{M_b}{M_0}(0\,\mathrm{ms})\right] = \sqrt{\delta\left[\frac{M_b}{M_0}(18\,\mathrm{ms})\right]^2 + \delta\left[\frac{M_b}{M_0}(0\,\mathrm{ms})\right]^2}\ . \tag{7.16}$$

In Figure 7.11 the scaled magnitude data from the splenium of the corpus callosum acquired at $\Delta t = 18\,\mathrm{ms}$ is plotted against the data acquired at $\Delta t = 0\,\mathrm{ms}$. The errorbars were calculated from the standard deviations of the magnitude data over dynamics acquired at $b = 0\,{}^{\mathrm{s}}/_{\mathrm{mm}^2}$ and $b = 1200\,{}^{\mathrm{s}}/_{\mathrm{mm}^2}$ using error propagation. We observed a significant increase of the scaled magnitude with Δt in some regions (data points above the red lines) in all subjects.

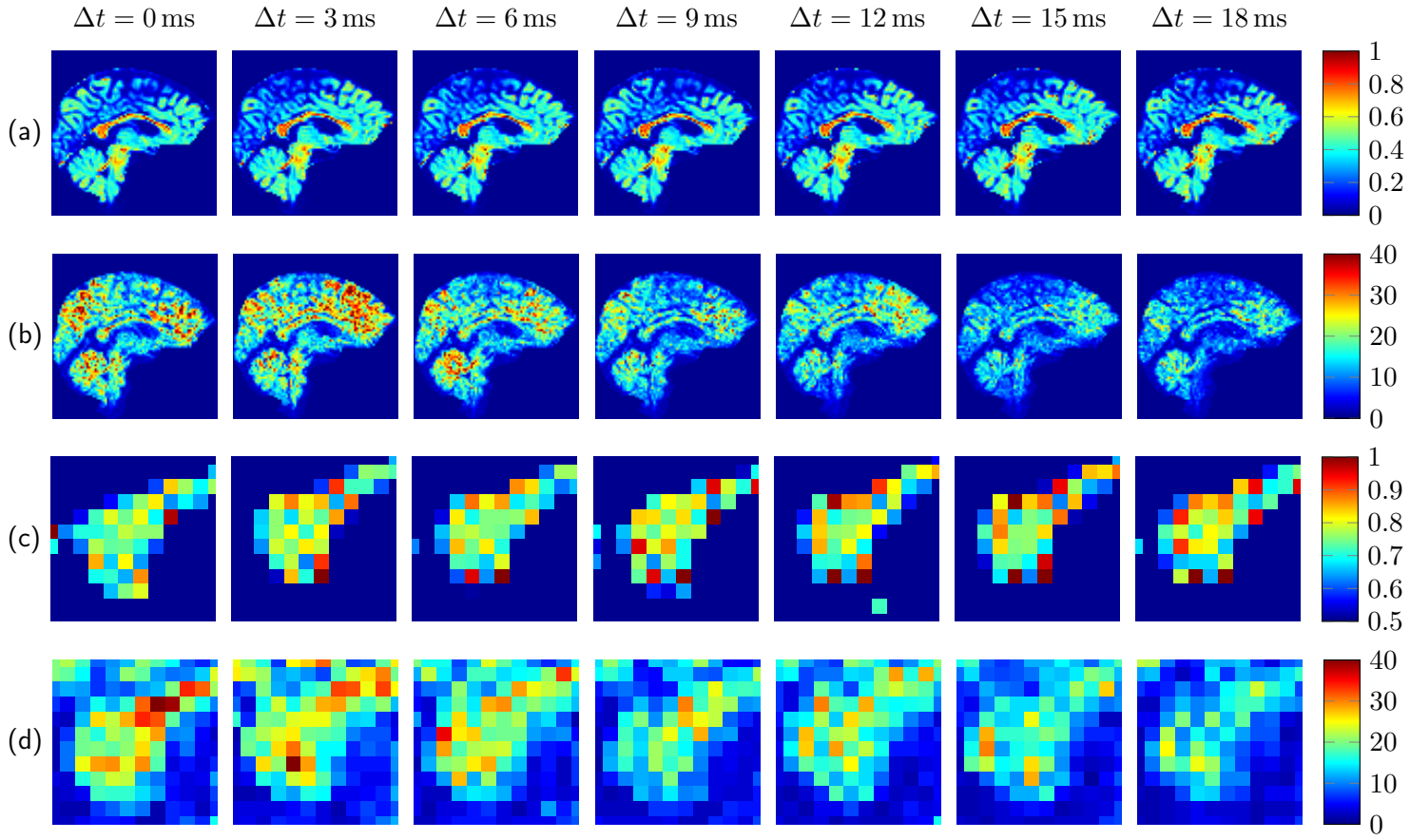


Figure 7.8.: The magnitude data (Subject 2) acquired at $\mathrm{TE}_{\mathsf{SE}} = 71\,\mathrm{ms}$ and $b = 1200\,{}^{\mathrm{s}}/_{\mathrm{mm}^2}$, were scaled by the magnitude data acquired with $b = 0\,{}^{\mathrm{s}}/_{\mathrm{mm}^2}$ at same Δt-value. The scaled magnitude and SNR maps of scaled images are shown as a function of Δt for the whole slice ((a) and (b), respectively), and zoomed onto a region of the splenium ((c) and (d), respectively).

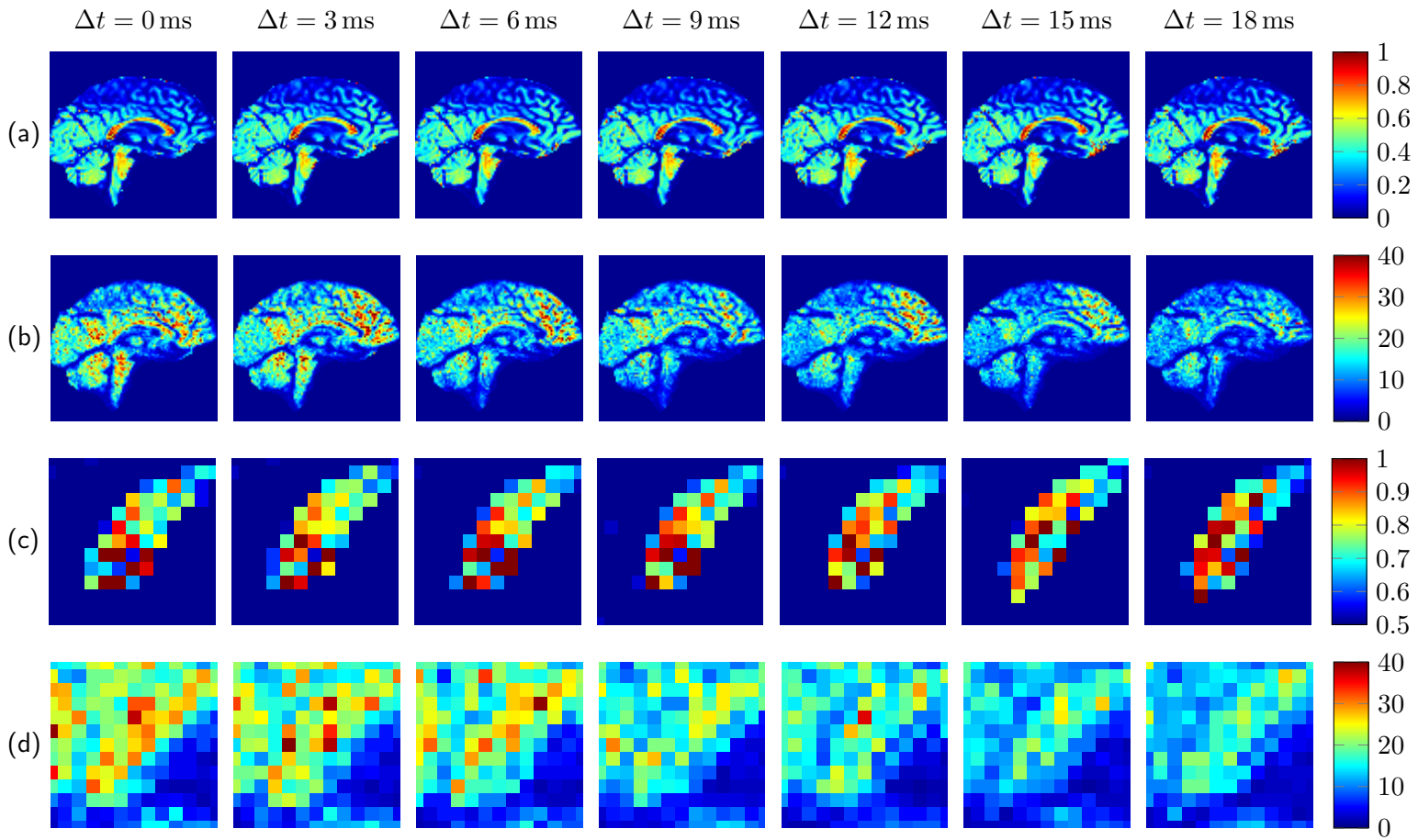


Figure 7.9.: The magnitude data (Subject 3) acquired at $\mathrm{TE}_{\mathsf{SE}} = 71\,\mathrm{ms}$ and $b = 1200\,{}^{\mathrm{s}}/_{\mathrm{mm}^2}$, were scaled by the magnitude data acquired with $b = 0\,{}^{\mathrm{s}}/_{\mathrm{mm}^2}$ at same Δt-value. The scaled magnitude and SNR maps of scaled images are shown as a function of Δt for the whole slice ((a) and (b), respectively), and zoomed onto a region of the splenium ((c) and (d), respectively).

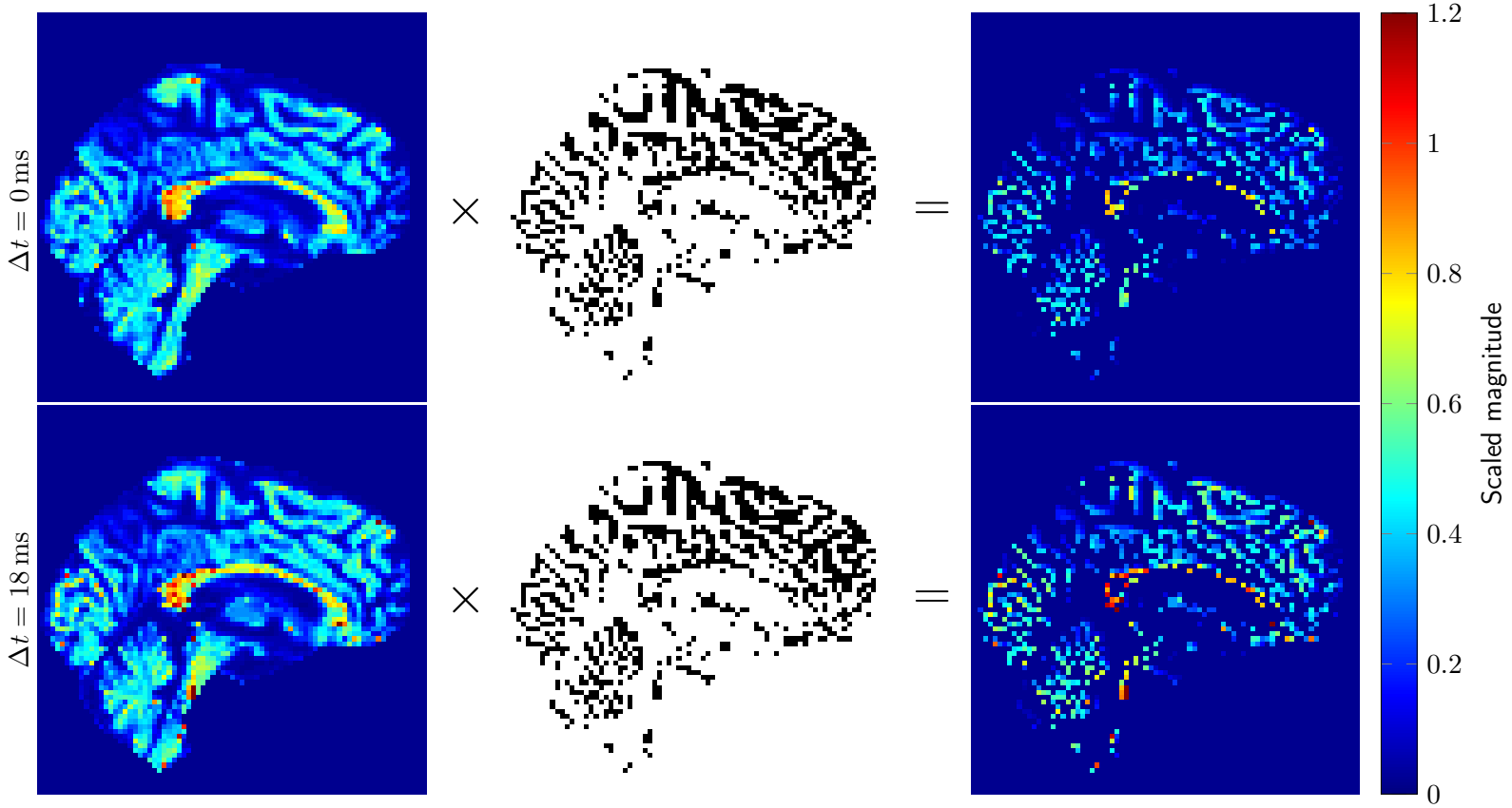


Figure 7.10.: Diffusion-weighted images (Subject 1) acquired at $\Delta t = 18$ (bottom left) and $\Delta t = 0$ (top left), using $b = 1200\,{}^{\mathrm{s}}/_{\mathrm{mm}^2}$ were subtracted from each other and the significant increase of ${}^{M_b}/_{M_0}$ values with Δt were used to calculate a binary mask (images in the middle are equivalent). The product between the diffusion-weighted images and the mask is shown for each Δt on the right.

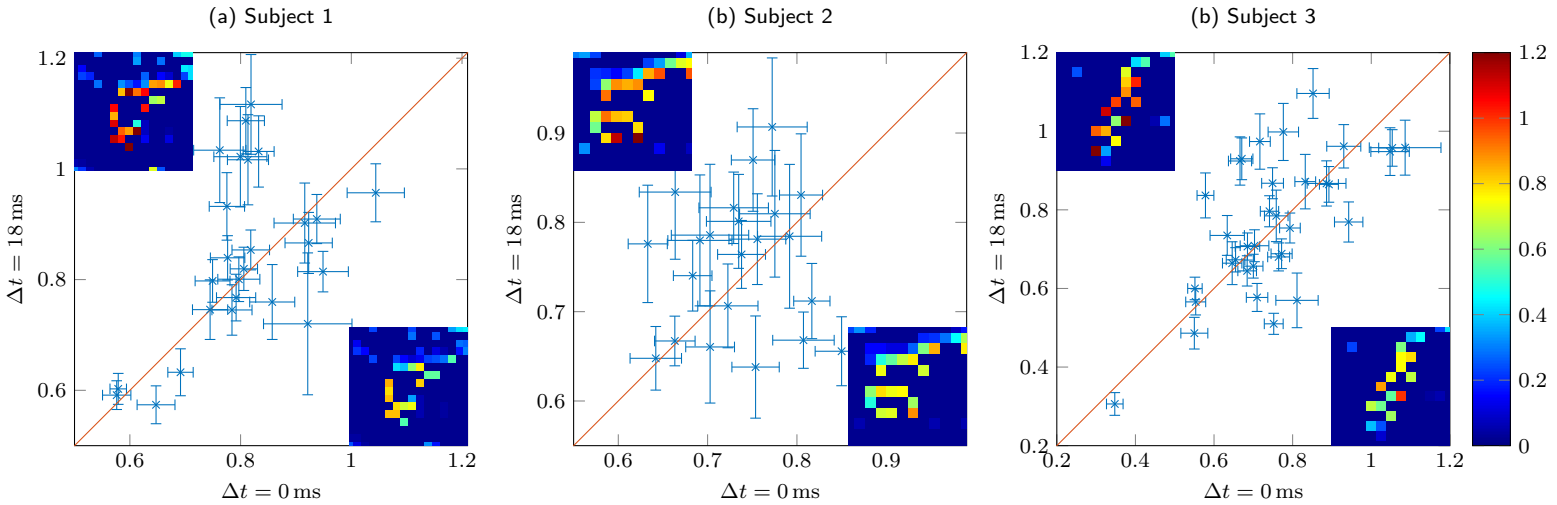


Figure 7.11.: Scaled magnitude data $^{M_b}/_{M_0}$ (for $b = 1200\,^{\mathrm{s}}/_{\mathrm{mm}^2}$) from the splenium in the corpus callosum from all subjects acquired at $\Delta t = 18\,\mathrm{ms}$ was plotted against the data acquired at $\Delta t = 0\,\mathrm{ms}$. The errorbars were calculated using error propagation from the standard deviations of the magnitude data acquired at $b = 0\,^{\mathrm{s}}/_{\mathrm{mm}^2}$ and $b = 1200\,^{\mathrm{s}}/_{\mathrm{mm}^2}$. The diffusion-weighted images acquired at $\Delta t = 0\,\mathrm{ms}$ and $\Delta t = 18\,\mathrm{ms}$ are zoomed onto a region of the splenium and masked for the areas of the significantly positive increase of $^{M_b}/_{M_0}$ with Δt, similarly to Figure 7.10.

7.5. Discussion

Signal attenuation due to Random walk In the corpus callosum data acquired at $\Delta t = 0\,\mathrm{ms}$ (images in the first column in Figure 7.6 and Figure 7.7) we observed an increase of the signal attenuation with b-value. The scaled magnitude $\left[{}^{M_b}/_{M_0}\right]_{\Delta t}$ in the corpus callosum ranges between 0.7–0.9 at $b = 1200\,{}^{\mathrm{s}}/_{\mathrm{mm}^2}$, whereas the CSF signal has fully decayed. This correlates with restricted/hindered diffusion in the corpus callosum perpendicular to the fibres and free diffusion in CSF.

Similar behaviour was observed in Subject 2 (Figure 7.8 images at $\Delta t = 0$ in (a) and (c)), and in Subject 3 (Figure 7.9 images at $\Delta t = 0$ in (a) and (c)).

Additional contrast due to magnetic properties of white matter The corpus callosum is the largest white matter fibre bundle in the human brain and its fibres are oriented perpendicular to the magnetic field, for the conventional position of the subject in the scanner. For this fibre orientation we expect the largest frequency offset (Wharton and Bowtell (2012)), and the largest R_2^* contrast (Lee et al. (2017)) between the external and the intra-axonal compartments. With constant b-values we observed a reduction of the signal attenuation in some regions and increase of the (global) spatial contrast with increasing acquisition delay Δt in the corpus callosum (Figures 7.6, 7.7, and 7.10 for Subject 1, Figure 7.8 for Subject 2, and Figure 7.9 for Subject 3). This behaviour is also evident from the splenium data in the plots shown in Figure 7.11.

Based on theoretical predictions derived in Figure 7.2, the increase of the scaled signal with Δt can be interpreted as the reduction of the external compartment contribution to the signal. In the scaled magnitude images and in plots in Figure 7.11 we observed significant increase of the scaled signal with Δt in some regions in the corpus callosum.

This could mean that the contribution from the external compartment in these regions is significantly lower than in the regions where the scaled signal remained constant. The initial hypothesis is that in the regions in the corpus callosum with the increased scaled signal at $\Delta t = 18\,\mathrm{ms}$ the apparent diffusion coefficient of the external compartment is larger than in the other regions. Since the apparent diffusion coefficient of external compartment at long diffusion times may reflect the geometry of the regions, and is possibly increased in the regions of larger axons or of sparse axonal distribution (due to lower tortuosity in the external compartment), the regions of the increased scaled signal at $\Delta t = 18\,\mathrm{ms}$ could be interpreted as regions with larger axons or of sparse axonal distribution.

These preliminary results and considerations require further investigation. We need to investigate the effects of the average radius and density of the axonal compartment on the apparent diffusion coefficient of external compartment. We also could increase the contrast by increasing Δt-values and/or by increasing the diffusion weighting. More information on fibre orientation could also be benificial.

7.6. Conclusion

We have proposed a method which allows us jointly to investigate the diffusive and magnetic properties of white matter tissue. The initial results show consistency with theory in some regions in the corpus callosum and are repeatable across the subjects. To increase the contrast, we can increase the b-values or the acquisition delay Δt. In either case we need to consider SNR, which reduces with increasing b- or Δt-values. We could identify optimal Δt by taking into account SNR in out theoretical considerations. Since both the magnetic and diffusive properties of white matter tissue reflect the orientation and compartmentalisation dependence in a different manner, this method

could be applied to better separate the effects of fibre dispersion and axonal volume fraction by combining diffusion tensor imaging with asymmetric spin-echo sequence. The difference in electromagnetic properties between the external and the intra-axonal compartments depends on the fibre orientation (θ) to $\vec{B}_0$ and varies with $\sin^2\theta$. Hence, it is negligible for θ approaching 0°. We expect that the radial element of diffusion tensor will decrease with increasing Δt for fibres perpendicular to $\vec{B}_0$, but remain unchanged for fibres parallel to $\vec{B}_0$.

Additionally, by applying a more robust method to process the phase data, we can gain additional information on the frequency offset between the external and the intra-axonal water pools.

Conclusion

This work demonstrated a method which allowed frequency difference mapping to be applied to complex data acquired using a multi-echo gradient-echo (MEGE) sequence with bipolar read gradients. Using bipolar read gradients allowed us to reduce the echo spacing and thus improve the temporal resolution with which the signal is sampled. This is important when probing short-T_2^* ($< 10\,\mathrm{ms}$) compartments, such as myelin water or venous blood. This method was used to investigate microstructural information from local complex signal evolution in a complex phantom and in *in vivo* measurements at $7\,\mathrm{T}$.

Models that describe electromagnetic properties of venous and white matter microstructure (the infinite cylinder model [ICM] and the hollow cylinder model [HCM]) were used to determine the complex signal evolution in a MEGE sequence. These were specifically: a 2-compartment model of local venous signal evolution, and a 3-pool model of white matter signal evolution.

The 2-compartment model was used to investigate local venous signal evolution *in vivo*. We acquired normoxic, single-slice, mid-sagittal MEGE data from 4 subjects. Measurements were also acquired from one subject during hyperoxia. The results showed that the frequency offset between the venous and tissue compartments estimated from the local complex signal evolution can be modelled as a function of susceptibility differ-

ence and venous orientation to $\vec{B}_0$ using the 2-compartment model. This allowed the venous blood oxygenation levels to be estimated *in vivo*. This new approach needs further validation against existing methods for measuring blood oxygenation, but we propose that it can be used to investigate cerebral microvasculature in grey matter.

Additionally, the 2-compartment model was validated on a phantom which contained aligned capillary tubes filled with ferritin solution and placed in water bath. MEGE data were acquired from the phantom for different capillary orientations with respect to the magnetic field. Resonant frequency differences between the water and the ferritin compartments were calculated from analysis of the complex data evolution and found to agree well with theory. We thus demonstrated that FDM data is sensitive to capillary orientation and to the susceptibility values of the ferritin solution, while the magnitude data is insensitive to the sign of the frequency offset between the compartments. This data supports our initial *in vivo* results and provides a better understanding of limitations and opportunities for future work.

A saturation-recovery MEGE sequence was used to investigate white matter microstructure *in vivo*. Data were acquired from 5 healthy subjects using a short TR and 6 nominal flip angles which varied between 8° and 80°. The observed increase of the FDM contrast with flip angle implies lesser relative saturation of the myelin water signal and agrees with the expectation that there is a short-T_1 component of longitudinal magnetisation associated with myelin water pool. However the difference in FDM contrast between the extreme flip angles was found to be significantly lower than expected from previously reported T_1 values. This could be explained by varying rates of exchange between the different compartments, but this hypothesis needs to be further tested.

Finally, a diffusion-weighted, asymmetric spin echo (DW-ASE) sequence was performed on 3 subjects and used to investigate simultaneously the diffusivity and electromag-

netic properties of the external and intra-axonal compartments in the white matter of the corpus callosum. Both the frequency offsets and diffusive attenuation reflect fibre orientation and could provide complementary information about white matter microstructure. Diffusion-weighting gradients were applied perpendicular to white matter fibres in the corpus callosum. Since the fibres are perpendicular to the magnetic field, we expect the highest difference between the resonant frequencies and transverse relaxation rates in the external and the intra-axonal compartments. The observed increase of the signal acquired with non-zero b-values, scaled by the $b = 0\,{}^{\mathrm{s}}/_{\mathrm{mm}^2}$ signal (acquired with the same acquisition delay Δt), with increasing Δt in some white matter regions correlates with theoretical predictions. However, the interpretation of these results requires further investigation. The contrast could be enhanced by increasing Δt and/or by applying stronger diffusion weighting. Additionally, we could benefit from applying diffusion weighting in multiple directions.

Future work In summary, the local complex MRI signal evolution is non-mono-exponential due to differences in electromagnetic properties between compartments in the presence of white matter microstructure and the venous vasculature. This can allow us to distinguish between the compartments and access important microstructural and metabolic information.

As such, these results suggest a number of interesting applications. For instance, we propose to use MEGE complex signal evolution processed with FDM to investigate microvasculature in the grey matter of the brain. Additionally, we could investigate exchange effects in different water pools in white matter on the MEGE complex signal evolution by applying magntisation transfer saturation prior to the sequence. Finally, we could further investigate the effects of diffusion weighting in an asymmetric spin

echo sequence in white matter regions by applying diffusion-weighting along multiple directions and varying the strength of diffusion- and T_2^*-weightings.

Bibliography

Andersen, M., Hanson, L. G., Madsen, K. H., Wezel, J., Boer, V., van der Velden, T., van Osch, M. J. P., Klomp, D., Webb, A. G., and Versluis, M. J. (2016). Measuring motion-induced B_0-fluctuations in the brain using field probes. *Magnetic Resonance in Medicine*, 75(5):2020–2030.

Arfken, G. B., Weber, H. J., and Spector, D. (1999). Mathematical Methods for Physicists, 4th ed. *American Journal of Physics*, 67(2):165–169.

Arrighini, G. P. (1968). Magnetic Properties of Polyatomic Molecules. I. Magnetic Susceptibility of $\mathrm{H_2O}$, $\mathrm{NH_3}$, $\mathrm{CH_4}$, $\mathrm{H_2O_2}$. *The Journal of Chemical Physics*, 49(2):882.

Assaf, Y., Freidlin, R. Z., Rohde, G. K., and Basser, P. J. (2004). New modelling and experimental framework to characterize hindered and restricted water diffusion in brain white matter. *Magnetic Resonance in Medicine*, 52(5):965–978.

Bernstein, M. A., King, K. F., and Zhou, X. J. (2004). *Handbook of MRI Pulse Sequences*. Academic Press.

Blockley, N. P., Jiang, L., Gardener, A. G., Ludman, C. N., Francis, S. T., and Gowland, P. A. (2008). Field strength dependence of R_1 and R_2^* relaxivities of human

whole blood to ProHance, vasovist, and deoxyhemoglobin. *Magnetic Resonance in Medicine*, 60(6):1313–1320.

Bouhrara, M. and Spencer, R. G. (2017). Rapid simultaneous high-resolution mapping of myelin water fraction and relaxation times in human brain using BMC-mcDESPOT. *NeuroImage*, 147(Supplement C):800–811.

Carr, H. Y. and Purcell, E. M. (1954). Effects of Diffusion on Free Precession in Nuclear Magnetic Resonance Experiments. *Phys. Rev.*, 94(3):630–638.

Dagher, J. and Du, Y. P. (2012). Efficient and robust estimation of blood oxygenation levels in single cerebral veins. *Medical & Biological Engineering & Computing*, 50(5):473–482.

Deistung, A., Rauscher, A., Sedlacik, J., Stadler, J., Witoszynskyj, S., and Reichenbach, J. R. (2008). Susceptibility weighted imaging at ultra high magnetic field strengths: Theoretical considerations and experimental results. *Magnetic Resonance in Medicine*, 60(5):1155–1168.

Deville, G., Bernier, M., and Delrieux, J. M. (1979). NMR multiple echoes observed in solid $^3\mathrm{He}$. *Physical Review B*, 19(11):5666–5688.

Doty, F. D., Entzminger, G., and Yang, Y. A. (1998). Magnetism in High-Resolution NMR Probe Design. I: General Methods. *Concepts Magn Reson*, 10:133–156.

Driver, I. D., Wharton, S. J., Croal, P. L., Bowtell, R., Francis, S. T., and Gowland, P. A. (2014). Global intravascular and local hyperoxia contrast phase-based blood oxygenation measurements. *NeuroImage*, 101(Supplement C):458–465.

Durrant, C. J., Hertzberg, M. P., and Kuchel, P. W. (2003). Magnetic susceptibility: Further insights into macroscopic and microscopic fields and the sphere of Lorentz. *Concepts in Magnetic Resonance Part A: Bridging Education and Research*, 18(1):72–95.

Duyn, J. H. (2012). The future of ultra-high field MRI and fMRI for study of the human brain.

Fan, A. P., Bilgic, B., Gagnon, L., Witzel, T., Bhat, H., Rosen, B. R., and Adalsteinsson, E. (2014). Quantitative oxygenation venography from MRI phase. *Magnetic Resonance in Medicine*, 72(1):149–159.

Haacke, E. M., Brown, R. W., Thompson, M. R., and Venkatesan, R. (1999). *Magnetic Resonance Imaging: Physical Principles and Sequence Design*. Wiley.

Haacke, E. M., Mittal, S., Wu, Z., Neelavalli, J., and Cheng, Y.-C. (2009). Susceptibility-Weighted Imaging: Technical Aspects and Clinical Applications, Part 1. *American Journal of Neuroradiology*, 30(1):19–30.

Hahn, E. L. (1950). Spin Echoes. *Phys. Rev.*, 80(4):580–594.

Hargreaves, B. and Lu, W. (2010). Magnetic Resonance Imaging with bipolar multi-echo sequences.

He, X. and Yablonskiy, D. A. (2007). Quantitative BOLD: Mapping of human cerebral deoxygenated blood volume and oxygen extraction fraction: Default state. *Magnetic Resonance in Medicine*, 57(1):115–126.

Henkelman, R. M., Stanisz, G. J., and Graham, S. J. (2001). Magnetization transfer in MRI: A review.

Jackson, J. D. (1975). *Classical electrodynamics*. John Wiley & Sons, 2nd edition.

Jain, V., Abdulmalik, O., Propert, K. J., and Wehrli, F. W. (2012). Investigating the magnetic susceptibility properties of fresh human blood for noninvasive oxygen saturation quantification. *Magnetic Resonance in Medicine*, 68(3):863–867.

Jehenson, P., Westphal, M., and Schuff, N. (1990). Analytical method for the compensation of eddy-current effects induced by pulsed magnetic field gradients in NMR systems. *Journal of Magnetic Resonance (1969)*, 90(2):264–278.

Jenkinson, M., Wilson, J. L., and Jezzard, P. (2004). Perturbation method for magnetic field calculations of nonconductive objects. *Magnetic Resonance in Medicine*, 52(3):471–477.

Kim, D., Lee, H. M., Oh, S.-H., and Lee, J. (2015). Probing signal phase in direct visualization of short transverse relaxation time component (ViSTa). *Magnetic Resonance in Medicine*, 74(2):499–505.

Labadie, C., Lee, J.-H., Rooney, W. D., Jarchow, S., Aubert-Frécon, M., Springer, C. S., and Möller, H. E. (2014). Myelin water mapping by spatially regularized longitudinal relaxographic imaging at high magnetic fields. *Magnetic Resonance in Medicine*, 71(1):375–387.

Lee, J., Nam, Y., Choi, J. Y., Kim, E. Y., Oh, S.-H., and Kim, D.-H. (2017). Mechanisms of T_2^* anisotropy and gradient echo myelin water imaging. *NMR in Biomedicine*, 30(4):e3513–n/a.

Lee, J., Shmueli, K., Fukunaga, M., van Gelderen, P., Merkle, H., Silva, A. C., and Duyn, J. H. (2010). Sensitivity of MRI resonance frequency to the orientation

of brain tissue microstructure. *Proceedings of the National Academy of Sciences*, 107(11):5130–5135.

Li, C., Langham, M. C., Epstein, C. L., Magland, J. F., Wu, J., Gee, J., and Wehrli, F. W. (2012). Accuracy of the cylinder approximation for susceptometric measurement of intravascular oxygen saturation. *Magnetic Resonance in Medicine*, 67(3):808–813.

Liu, C. (2010). Susceptibility tensor imaging. *Magnetic Resonance in Medicine*, 63(6):1471–1477.

Lu, H. and Ge, Y. (2008). Quantitative evaluation of oxygenation in venous vessels using T_2-Relaxation-Under-Spin-Tagging MRI. *Magnetic Resonance in Medicine*, 60(2):357–363.

Lu, W., Yu, H., Shimakawa, A., Alley, M., Reeder, S. B., and Hargreaves, B. A. (2008). Water-fat separation with bipolar multiecho sequences. *Magnetic Resonance in Medicine*, 60(1):198–209.

Marques, J. P. and Bowtell, R. (2005). Application of a Fourier-based method for rapid calculation of field inhomogeneity due to spatial variation of magnetic susceptibility. *Concepts in Magnetic Resonance Part B: Magnetic Resonance Engineering*, 25B(1):65–78.

Nam, Y., Lee, J., Hwang, D., and Kim, D.-H. (2015). Improved estimation of myelin water fraction using complex model fitting. *NeuroImage*, 116:214 – 221.

Oh, S. H., Bilello, M., Schindler, M., Markowitz, C. E., Detre, J. A., and Lee, J.

(2013). Direct visualization of short transverse relaxation time component (ViSTa). *NeuroImage*, 83:485–492.

Peters, A. M., Brookes, M. J., Hoogenraad, F. G., Gowland, P. A., Francis, S. T., Morris, P. G., and Bowtell, R. (2007). T_2^* measurements in human brain at 1.5, 3 and $7\,\mathrm{T}$. *Magnetic Resonance Imaging*, 25(6):748–753.

Peterson, P. and Månsson, S. (2014). Fat Quantification Using Multiecho Sequences with Bipolar Gradients: Investigation of Accuracy and Noise Performance. *Magnetic Resonance in Medicine*, 71:219–229.

Rane, S. D. and Gore, J. C. (2013). Measurement of T_1 of human arterial and venous blood at $7\,\mathrm{T}$. *Magnetic Resonance Imaging*, 31(3):477–479.

Salomir, R., de Senneville, B. D., and Moonen, C. T. (2003). A fast calculation method for magnetic field inhomogeneity due to an arbitrary distribution of bulk susceptibility. *Concepts in Magnetic Resonance Part B: Magnetic Resonance Engineering*, 19B(1):26–34.

Sati, P., van Gelderen, P., Silva, A. C., Reich, D. S., Merkle, H., de Zwart, J. A., and Duyn, J. H. (2013). Micro-compartment specific T_2^* relaxation in the brain. *NeuroImage*, 77:268–278.

Schäfer, A., Wharton, S., Gowland, P., and Bowtell, R. (2009). Using magnetic field simulation to study susceptibility-related phase contrast in gradient echo MRI. *NeuroImage*, 48(1):126–137.

Schweser, F., Deistung, A., Lehr, B. W., and Reichenbach, J. R. (2011). Quantitative

imaging of intrinsic magnetic tissue properties using MRI signal phase: An approach to in vivo brain iron metabolism? *NeuroImage*, 54(4):2789–2807.

Sedlacik, J., Rauscher, A., and Reichenbach, J. R. (2009). Quantification of modulated blood oxygenation levels in single cerebral veins by investigating their MR signal decay. *Zeitschrift für Medizinische Physikr Medizinische Physik*, 19(1):48–57.

Stejskal, E. O. and Tanner, J. E. (1965). Spin Diffusion Measurements: Spin Echoes in the Presence of a Time-Dependent Field Gradient. *The Journal of Chemical Physics*, 42(1):288–292.

Tendler, B. C. and Bowtell, R. (2018). Frequency difference mapping applied to the corpus callosum at $7\,\mathrm{T}$. Manuscript submitted for publication.

van de Moortele, P.-F., Pfeuffer, J., Glover, G. H., Ugurbil, K., and Hu, X. (2002). Respiration-induced B_0 fluctuations and their spatial distribution in the human brain at 7 Tesla. *Magnetic Resonance in Medicine*, 47(5):888–895.

van Gelderen, P., de Zwart, J., Starewicz, P., Hinks, R., and Duyn, J. (2007). Real-time shimming to compensate for respiration-induced B_0 fluctuations. *Magnetic Resonance in Medicine*, 57(2):362–368.

van Gelderen, P., de Zwart, J. A., Lee, J., Sati, P., Reich, D. S., and Duyn, J. H. (2012). Nonexponential T_2^* decay in white matter. *Magnetic Resonance in Medicine*, 67(1):110–117.

van Gelderen, P., Jiang, X., and Duyn, J. H. (2016). Effects of magnetization transfer on T_1 contrast in human brain white matter. *NeuroImage*, 128:85–95.

van Vaals, J. J. and Bergman, A. H. (1990). Optimization of eddy-current compensation. *Journal of Magnetic Resonance (1969)*, 90(1):52–70.

Vannesjo, S. J., Wilm, B. J., Duerst, Y., Gross, S., Brunner, D. O., Dietrich, B. E., Schmid, T., Barmet, C., and Pruessmann, K. P. (2015). Retrospective correction of physiological field fluctuations in high-field brain MRI using concurrent field monitoring. *Magnetic Resonance in Medicine*, 73(5):1833–1843.

Weisskoff, R. M. and Kiihne, S. (1992). MRI susceptometry: Image-based measurement of absolute susceptibility of MR contrast agents and human blood. *Magnetic Resonance in Medicine*, 24(2):375–383.

Wharton, S. and Bowtell, R. (2012). Fiber orientation-dependent white matter contrast in gradient echo MRI. *Proceedings of the National Academy of Sciences*, 109(45):18559–18564.

Wright, P., Mougin, O., Totman, J., Peters, A., and Brookes, M. (2008). Water proton T_1 measurements in brain tissue at 7, 3, and $1.5\,\mathrm{T}$ using IR-EPI, IR-TSE, and MPRAGE: results and optimization. *Magn Reson Mater Phy*, 21:121–130.

Yablonskiy, D. A. (1998). Quantitation of intrinsic magnetic susceptibility-related effects in a tissue matrix. Phantom study. *Magnetic Resonance in Medicine*, 39(3):417–428.

Yacoub, E., Shmuel, A., Pfeuffer, J., van De Moortele, P.-F., Adriany, G., Andersen, P., Vaughan, J. T., Merkle, H., Ugurbil, K., and Hu, X. (2001). Imaging brain function in humans at 7 Tesla. *Magnetic Resonance in Medicine*, 45(4):588–594.

Yu, H., Shimakawa, A., McKenzie, C. A., Lu, W., Reeder, S. B., Hinks, R. S., and

Brittain, J. H. (2010). Phase and Amplitude Correction for Multi-Echo Water-Fat Separation With Bipolar Acquisitions. *Journal of Magnetic Resonance Imaging*, 31:1264–1271.

Zhang, J., Kolind, S. H., Laule, C., and MacKay, A. L. (2015). How does magnetization transfer influence mcDESPOT results? *Magnetic Resonance in Medicine*, 74(5):1327–1335.

Zheng, W., Nichol, H., Liu, S., Cheng, Y.-C. N., and Haacke, E. M. (2013). Measuring iron in the brain using quantitative susceptibility mapping and X-ray fluorescence imaging. *NeuroImage*, 78:68–74.

Ziener, C. H., Bauer, W. R., and Jakob, P. M. (2005). Frequency distribution and signal formation around a vessel. *Magnetic Resonance Materials in Physics, Biology and Medicine*, 18(4):225–230.